Development of a Lightning Strike Simulator with In-Situ Loading

Nimit Berry

A thesis

submitted in partial fulfillment of the

requirements for the degree of

Master of Science

University of Washington

2025

Committee:

Marco Salviato

Francesco Deleo

Program Authorized to Offer Degree:

Aeronautics & Astronautics

University of Washington

Abstract

Development of a Lightning Strike Simulator with In-Situ Loading

Nimit Berry

Chair of the Supervisory Committee:

Marco Salviato
Aeronautics and Astronautics

In recent decades, the use of composite materials in the aerospace industry has significantly increased, mainly due to their excellent strength-to-weight ratio. However, these materials have inherently low electrical conductivity, necessitating the inclusion of lightning strike protection systems (LSPs) that compromise their weight-saving benefits. A commercial aircraft is likely to experience 1-2 lightning strikes annually. Without adequate protection systems, this can lead to significant damage, including delamination, matrix cracking, and fiber breakage, potentially resulting in strength degradation and even catastrophic structural failure.

In accordance with current standards, the tests are conducted without applying mechanical loads to the specimen; therefore, they do not account for the influence of in-flight stress. This creates a

significant knowledge gap, as the damage characteristics of a specimen under load may differ considerably from those of an unloaded specimen.

To address this gap, this project aims to design and develop an artificial lightning strike simulator with in-situ loading, allowing for a more realistic assessment of damage mechanisms. The insights gained may also prompt an urgent reassessment of existing certification and regulatory standards, ultimately contributing to safer and more efficient operations.

TABLE OF CONTENTS

LIST OF FIGURES

LIST OF TABLES

ACKNOWLEDGEMENTS

I want to begin by expressing my gratitude to Professor Marco Salviato for the opportunity to work on this amazing project. His constant support has been crucial in guiding my academic journey at the University of Washington.

I also want to acknowledge the JCATI Project team: Kameron Harmon, for the countless hours spent on design, manufacturing, assembly, and coordination behind the scenes; Conner Murphy, for his dedication, consistency, and patience during our manufacturing sessions; Dejan Nikic, for his invaluable technical support and expertise, that made this project possible; and Sam Pedigo, for managing the technical details and administrative processes efficiently. I am genuinely grateful to each of you.

My advisors and mentors in the Aero-Astro department also deserve special thanks: Dr. Ed Habtour, Dr. Francesco Deleo, and Dr. Muzamil Arshad. Their unwavering support and encouragement have helped me grow and become a better student. I'd like to extend my appreciation to Paul Neubert and Betsy Winter for always being there to assist me, answering my questions, and making my journey as smooth as possible. I'm also thankful to everyone at MAMS for their assistance and feedback over the past year, which contributed significantly to the development of this final product.

Lastly, I'd like to express my heartfelt thanks to my family, friends, and colleagues at the University of Washington for their unwavering support and encouragement.

DEDICATION

To my grandfather, Col. (Dr.) L.K. Berry

Chapter 1: Introduction

1.1 Composite Materials in Aerospace: A Primer

In recent decades, the utilization of composite materials within the aerospace industry has increased significantly. "A Composite Material, as in the name, is a formation of two or more constituent materials, each having significantly different physical or chemical properties, when combined, produces a material which possesses unique characteristics different from the constituent elements" [1]. This trend is primarily driven by the superior structural characteristics of composite materials compared to their metallic counterparts, alongside their exceptional strength-to-weight ratio, which often facilitates a reduction in structural weight by 20% to 50% [2]. Consequently, this leads to enhanced fuel efficiency, resulting in decreased emissions and increased payload carrying capacity. The global aerospace market was valued at USD 38 billion in 2022 and is forecasted to expand at a compound annual growth rate (CAGR) of 9%, ultimately reaching a valuation of USD 98.1 billion by 2033 [3]. Since World War II, composite materials have been used in the production of military aircraft; however, they now constitute an essential component in the manufacturing of modern commercial aircraft [4]. For example, during the 1950s, composites, particularly fiberglass, accounted for only 2% of the structural weight in the long-range narrowbody Boeing 707. In stark contrast, contemporary widebody aircraft such as the Boeing 787 and Airbus A350, as well as the double-decker Airbus A380, utilize composite materials for approximately 50% and 25% of their structural weight, respectively. Notably, in the case of the Boeing 787, the incorporation of composite materials in the primary structure of the aircraft, as depicted in Figure 1.1, has resulted in a weight reduction of approximately 10,000 lbs.,

thus decreasing fuel consumption by over 20% [2]. Similarly, for the Airbus A380, the application of composites within the wings led to a 17% reduction in fuel consumption per passenger [5].

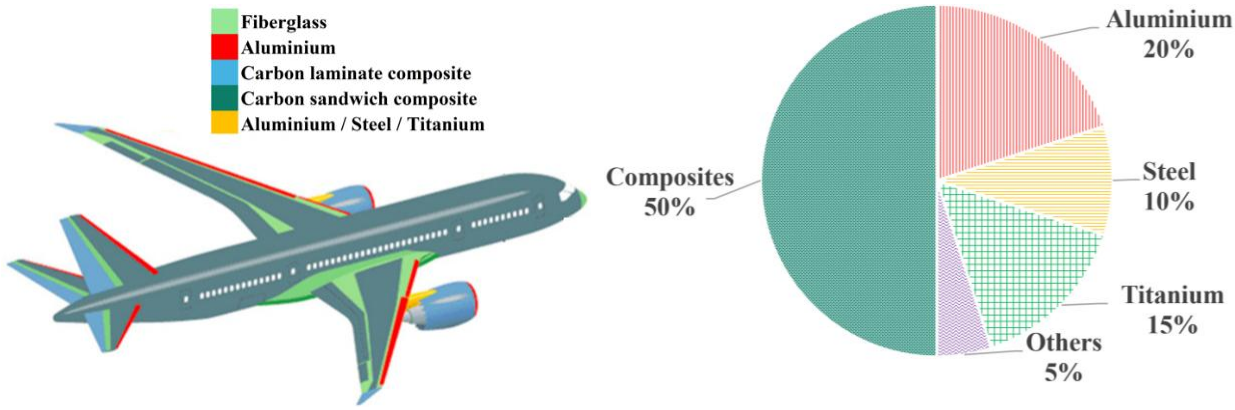

Figure 1.1. Material Composition of the Boeing 787 by Weight (Readapted from [6])

To provide a brief historical perspective, before the 1960s, composites were used in the fabrication of tertiary structures, including interior walls, bag racks, and galleys. Following this, these materials were deemed successful in secondary structural applications, particularly in the fabrication of wing and tail control surfaces [7]. The 1970s marked the transition from fiberglass to carbon in components such as helicopter rotor blades. In the 1980s, the horizontal stabilizer of the Boeing 737 and the vertical stabilizer of the Airbus A310 utilized high-performance composite materials, marking the first time composites were incorporated into the primary structure of large-scale commercial airplanes [8]. The Boeing 747 and 767 used composites to manufacture structures such as rudders, doors, elevators, flaps, ailerons, and aerodynamic fairings [9]. This led to the foundation for using composite materials in the horizontal and vertical stabilizers of the Boeing 777, a much larger wide-body aircraft [7]. The development, production, and delivery of the Boeing 787 marked a manufacturing revolution, as it became the first commercial aircraft to

utilize an all-composite construction in its wing and fuselage [10]. The evolution in the increased use of composites for Boeing aircraft is shown in Figure 1.2. This momentum continued with the Airbus A350 XWB in the 2010s, utilizing composites in 53% of the structure, including the wings, fuselage skin, and center wing box [8]. This trend continues with the Boeing 777X, which utilizes composite materials in wing construction and introduces folding wingtips [11]. The Russian MC-21 also uses composite materials in its wings, employing an out-of-autoclave manufacturing technique [12].

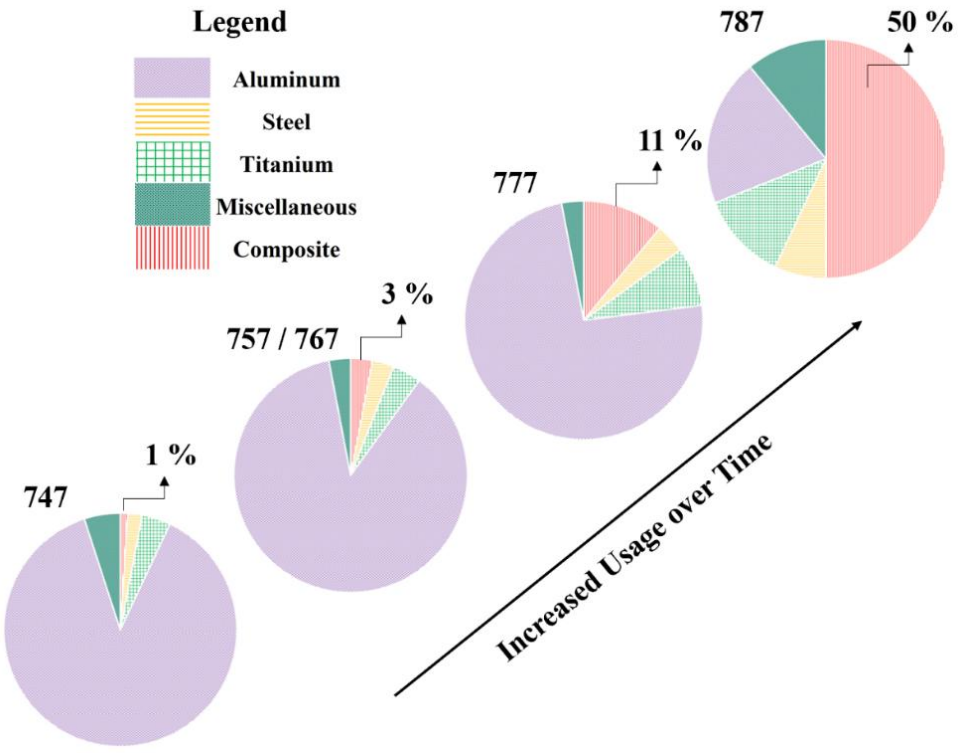

Figure 1.2. Material Composition Trends in Boeing Aircraft
(Readapted from [7])

These materials exhibit wear and corrosion resistance, making them ideal for aerospace applications. They also boast high strength and stiffness along with remarkable impact resistance

and damage tolerance, enabling them to effectively absorb impacts due to external forces [13],[14]. Composite structures require fewer riveted and welded joints, resulting in a smooth surface finish that improves aerodynamic efficiency by reducing drag. Additionally, these materials are also known for their outstanding thermal, electrical, and chemical stability. Manufacturing advancements have enabled them to be molded into complex shapes with ease, transitioning from hand lay-ups and manual fabrication to the use of advanced automated fiber placement machines [15],[16]. However, it is essential to acknowledge certain drawbacks, including the higher costs associated with both materials and fabrication processes. Moreover, recycling composite materials poses significant challenges, resulting in considerable waste. Repairing composites can also be more complicated than traditional materials, as damage may not be visible externally; fracture or delamination can occur internally without any surface indication. This necessitates the development of non-destructive testing methods to detect such failures [4]. Despite these challenges, the benefits of composite materials remain substantial, and ongoing research continues to focus on further enhancing their advantages.

1.2 **Lightning Strikes as a Critical Aerospace Hazard**

1.2.1 Historic Account and Case Studies

It is essential to refer to several significant case studies prior to formalizing and defining the threat posed by lightning strikes in aviation [17]. Furthermore, it is imperative to understand that the loss of life resulting from these incidents has profoundly altered our perception of lightning strikes and their impact on aircraft, consequently resulting in the establishment of stringent guidelines and safety standards [18]. Regulatory measures have confirmed that there has not been a major incident attributable to the direct effects of lightning strikes for the past fifty years [19].

1.2.1.1 LANSA Flight 508

LANSA 508 was a scheduled passenger flight originating from Lima to Iquitos with a stopover at Pucallpa, Peru. The aircraft operating this flight was a Lockheed L-188 Electra, a low-wing turboprop. The flight departed from Lima on December 24, 1971, with eighty-six passengers and six crew members on board. Forty minutes after takeoff, while cruising at an altitude of 21,000 feet, the aircraft encountered severe turbulence and thunderstorms. At this time, the plane was struck by lightning, which resulted in a fire and led to the detachment of the right wing and a portion of the left wing, ultimately causing a structural failure, and the airplane crashed into the jungle. Only one passenger, Juliane Koepcke, survived the incident and spent nine days alone in the jungle. Her tale of survival has been immortalized in multiple movies, documentaries, and her memoir [20],[21].

1.2.1.2 TWA Flight 891

Operated by a Lockheed L-1649A Starliner (Figure 1.3) this aircraft was flying from Athens, Greece, to Chicago, USA, with stopovers in Italy, France, Ireland, and Canada. The incident occurred on the Milan to Paris leg of the flight on June 26, 1959, with sixty-eight passengers and crew members onboard. The plane departed Milan in the evening amid scattered thunderstorms in the vicinity and reached an altitude of 10,000 ft. Within a few minutes, the structure failed, resulting in a mid-air breakup. Italian investigators concluded that the aircraft was struck by lightning, which ultimately caused the aircraft to go down. The in-flight breakup resulted from the ignition of fuel vapors, leading to the explosion of the fuel tank, primarily caused by static electricity discharges that developed on the vent outlets [22].

Figure 1.3. A Trans World Airlines Lockheed L-1649A Starliner [23]

1.2.1.3 Pan Am Flight 214

Pan Am 214 (Figure 1.4 (a)) was flying from San Juan, Puerto Rico, to Philadelphia with a stopover in Baltimore. On its final leg from Baltimore, there were seventy-three passengers and eight crew members on board the aircraft. Philadelphia was experiencing a series of thunderstorms, turbulence, and intense winds, prompting the pilots to maintain a holding pattern near the airport, where they encountered heavy rain, gusts, and lightning at an altitude of 5,000 feet. In under 15 minutes, the aircraft exploded and crashed into a field in Maryland (Figure 1.4 (b)). All souls on board were killed in this crash.

Investigators concluded, within a few days of the investigation, that the occurrence of an explosion was the cause of this event. This determination was made based on the discovery of remnants from the left-wing tip, located a few miles away from the wreckage, which exhibited burn marks and bulges indicative of an internal explosion. Further examination revealed that these burn marks corresponded to lightning strike marks, which affected a substantial area along the rear edge of the wing. This ignited the fuel-air mixture in one of the reserve tanks, which eventually led to the disintegration of the left wing.

This event represented a pivotal moment in the field of air crash investigation and safety, as prior to this incident, lightning strikes were not regarded as a causative factor in aviation accidents. At that time, the Boeing 707 was equipped with only basic lightning strike protection standards. This accident prompted further research into lightning strike incidents, leading to the development of regulations, testing standards, and protective measures that enhanced the safety of all commercial aircraft [24].

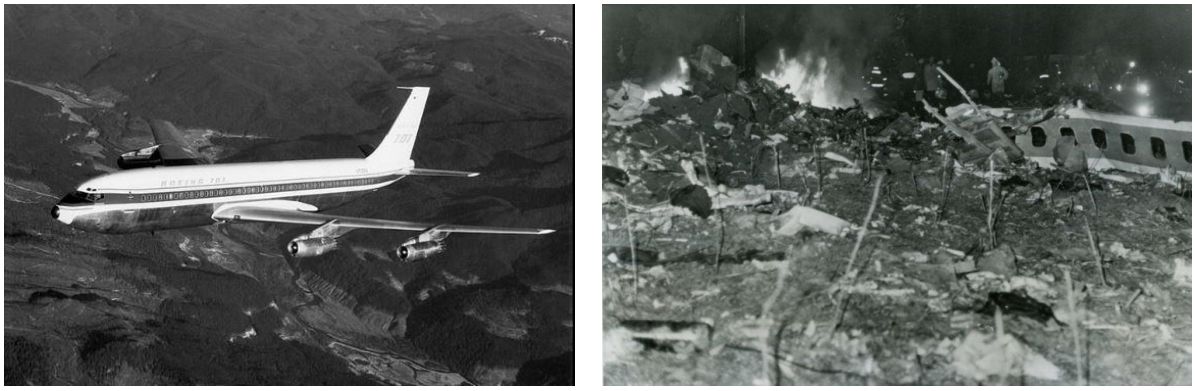

(a) A Pan Am Boeing 707 [25] *(b) Wreckage of Flight 214 [26]*

Figure 1.4. Images for Pan Am Flight 214

Additional information regarding the incidents previously mentioned, in addition to other notable accidents, can be found in [17].

1.2.2 Statistical Likelihood of Aircraft Lightning Encounters

Numerous studies have quantified the frequency and likelihood of lightning strikes, indicating that, on average, a commercial aircraft experiences lightning strikes 1 to 2 times annually [17],[27]. However, the frequency of lightning strikes depends on several factors such as geography and

altitude [28]. The geographic distribution of lightning is shown in Figure 1.5 where high activity is shown in the regions with black, red, brown, and orange, while purple and blue shades indicate low activity. Lightning tends to be more frequent near the equator due to convection that leads to the formation of thunderstorms, whereas it is less frequent near the poles and in certain oceanic regions.

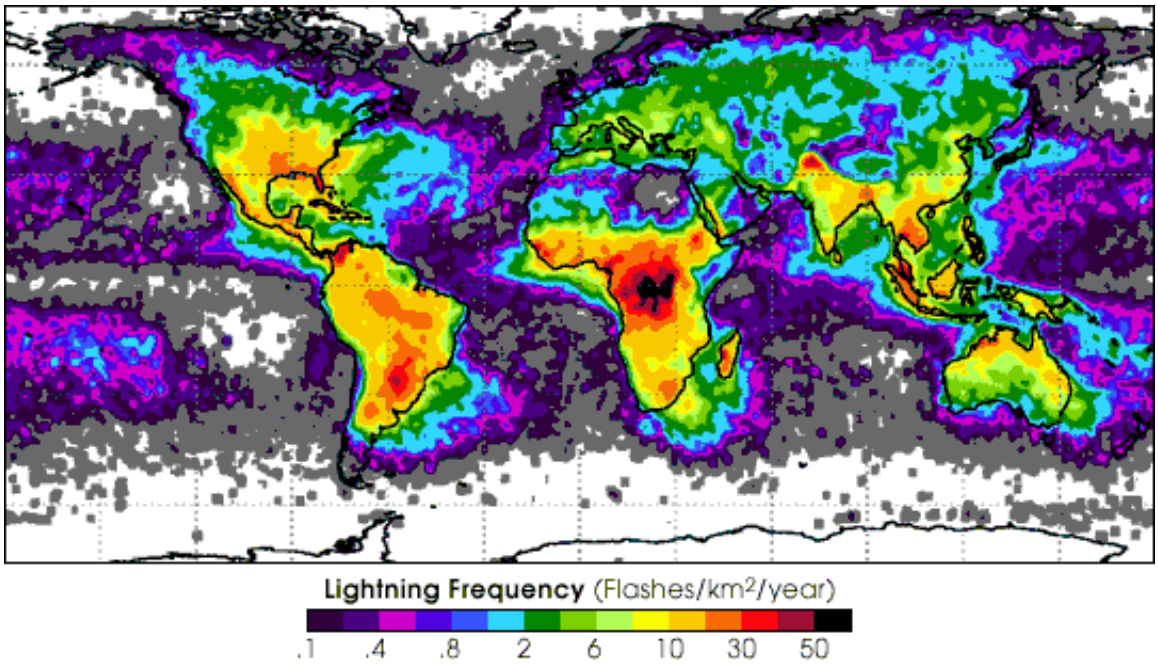

Figure 1.5. Global distribution of lightning frequency, expressed in flashes per square kilometer per year, April 1995 – February 2003 (NASA) [29]

Several studies were conducted in the 1950s and 1970s to statistically analyze the altitudes at which a lightning strike can occur. Figure 1.6 summarizes and plots the data from these studies (right) along with a typical representation of charge distribution in a cumulonimbus cloud (left). The turbojet and turboprop data agree, despite the studies being conducted in different geographies, including the USA, USSR, UK, and Europe. The data show that most transport

aircraft are struck by lightning at intermediate altitudes rather than during cruise [30]. As seen from Figure 1.7, Lightning strikes are more probable in the range of 5,000 to 15,000 feet, which corresponds to airplanes being likely to be struck by lightning strikes during climb, descent, or approach phases of flight. The number of lightning strikes during each regiment of flight is shown in Figure 1.8. Strikes above 10,000 ft. are due to intercloud flashes, i.e., between the positive and negative charge centers in the cloud. In contrast, any strikes below that altitude are due to cloud-ground interactions. The probability of lightning strikes above 20,000 ft. decreases significantly, as pilots can navigate to pass over or avoid the region affected by this weather phenomenon [31].

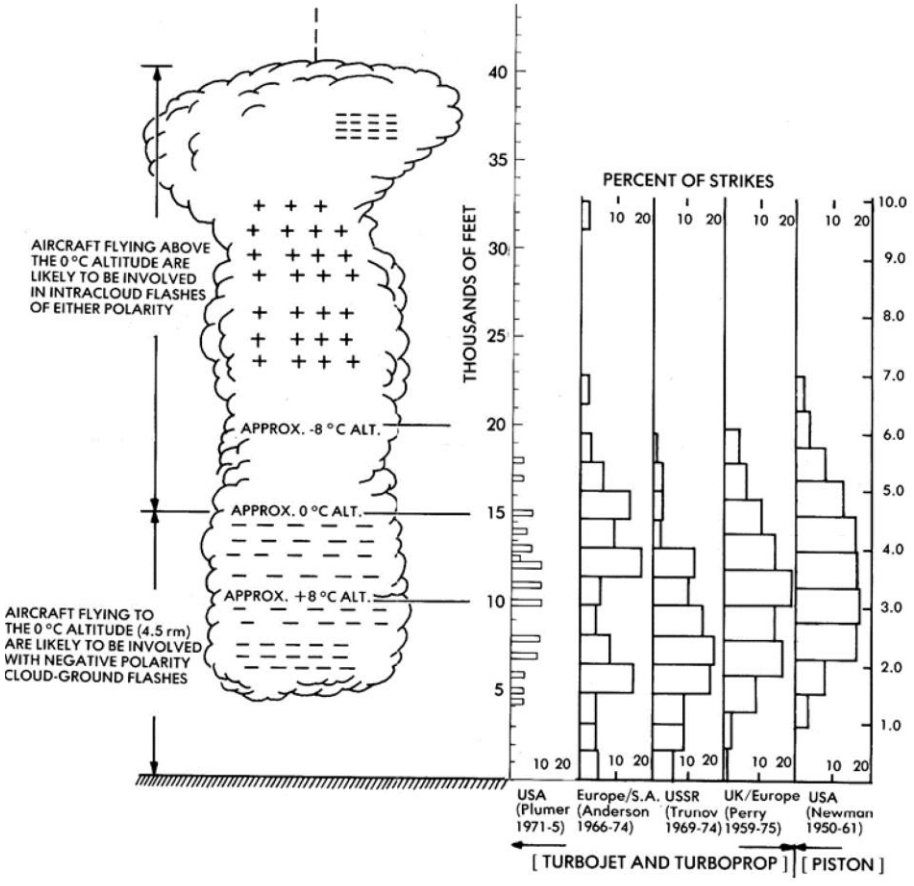

Figure 1.6. Charge Distribution in a cumulonimbus cloud (Left); Altitude distribution of lightning strikes on aircraft based on historical strike data (Right) [17]

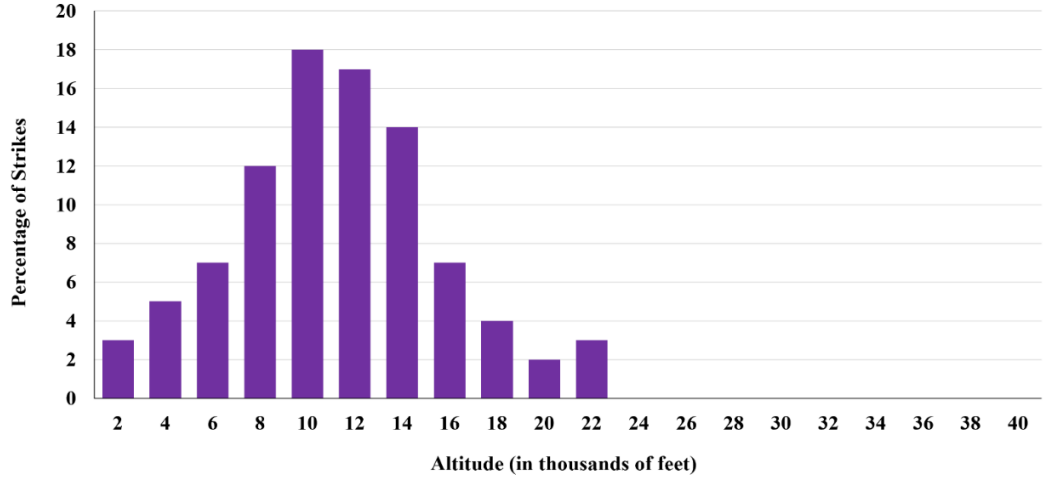

Figure 1.7. Distribution of lightning strikes by altitude (Readapted from[28], [32])

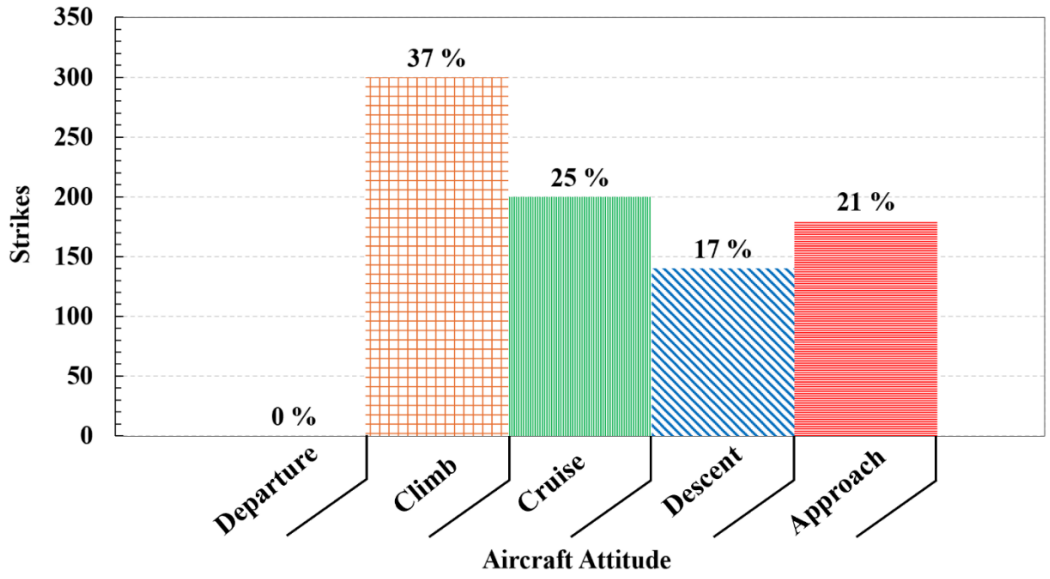

Figure 1.8. Lightning Strikes in percentage for each flight regiment (Readapted from [33],[32])

Synoptic meteorological conditions were analyzed during lightning strike incidents between July 1963 and June 1964 [33]. It was reported that the prevailing conditions leading to precipitation

may also be expected to produce lightning. Most strikes occurred during the spring due to the presence of conditions that typically lead to the formation of thunderstorms and associated phenomena. This is illustrated in Figure 1.9 and Figure 1.10.

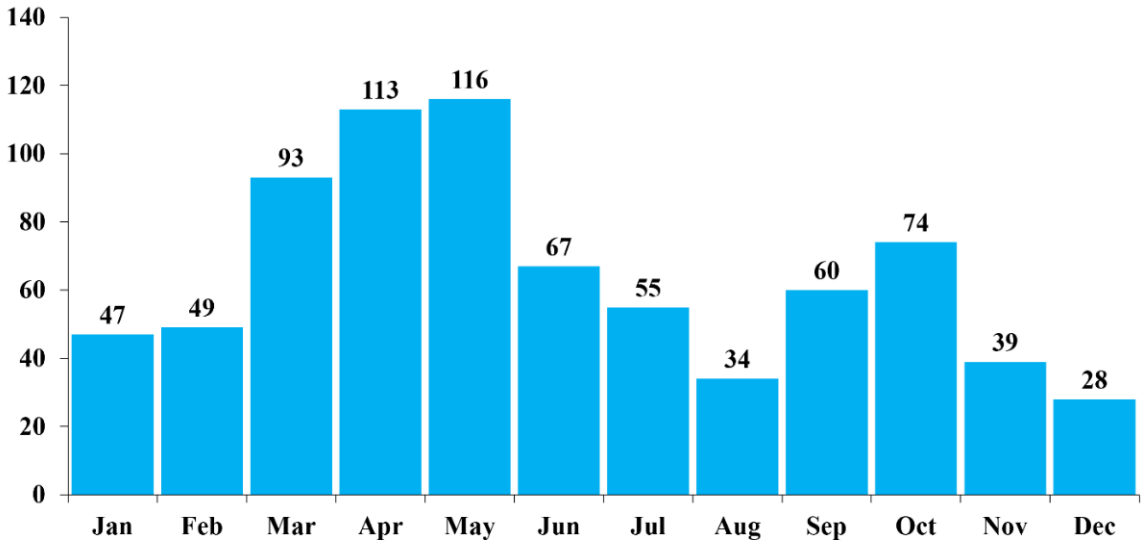

Figure 1.9. Strikes per month (Readapted from [32])

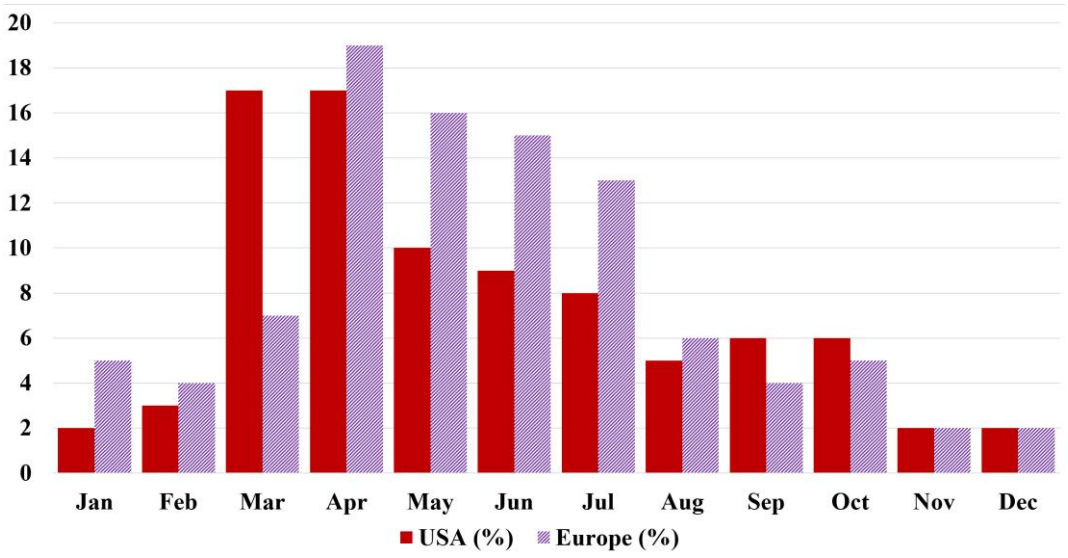

Figure 1.10. Occurrence of lightning strikes relative to months in Europe and the United States (Readapted from [32])

One should also consider the immediate environment at the time of the strike. A study referenced in [33], 80% of the 881 strikes that were reported occurred within a cloud in the presence of precipitation and some turbulence, as shown in Figure 1.11, Figure 1.12 and Figure 1.13. Furthermore, most strikes were encountered by the aircraft when they were in a range of 0 °C within a range of ±10°C, as depicted in Figure 1.14. This observation is crucial as freezing temperatures are associated with the electrical charge separation process.

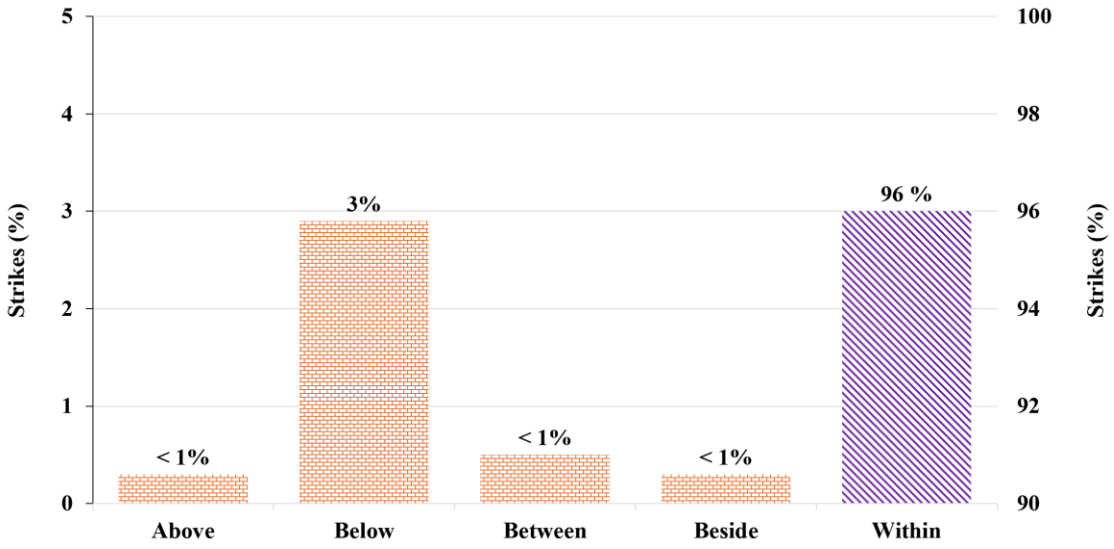

Figure 1.11. Aircraft Location with respect to clouds (Readapted from [32])

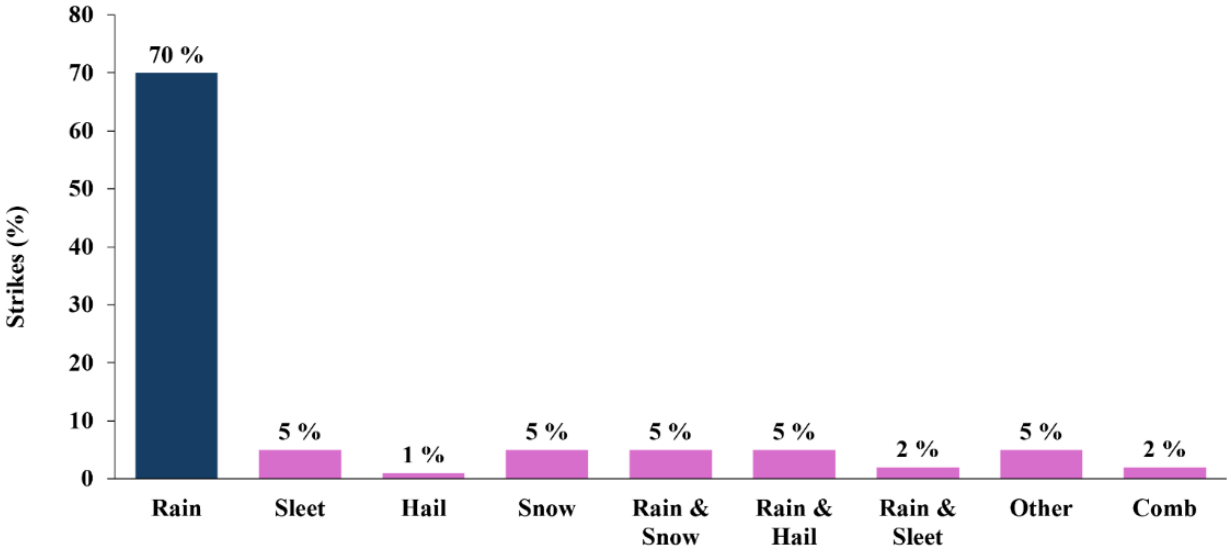

Figure 1.12. Precipitation at the time of aircraft lightning strikes (Readapted from [32])

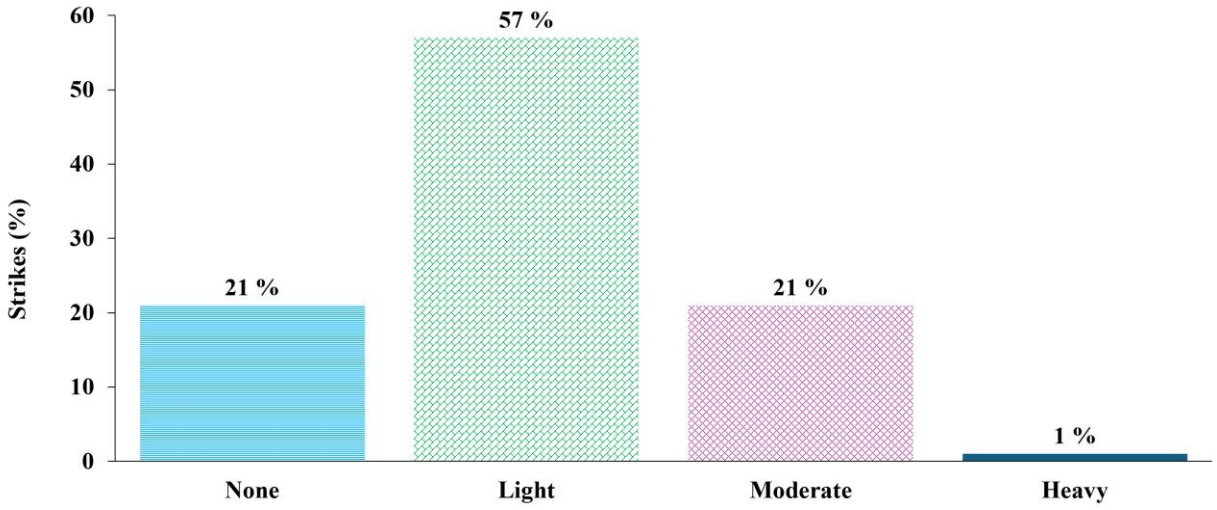

Figure 1.13. Turbulence when lightning strikes occurred
(Readapted from [32])

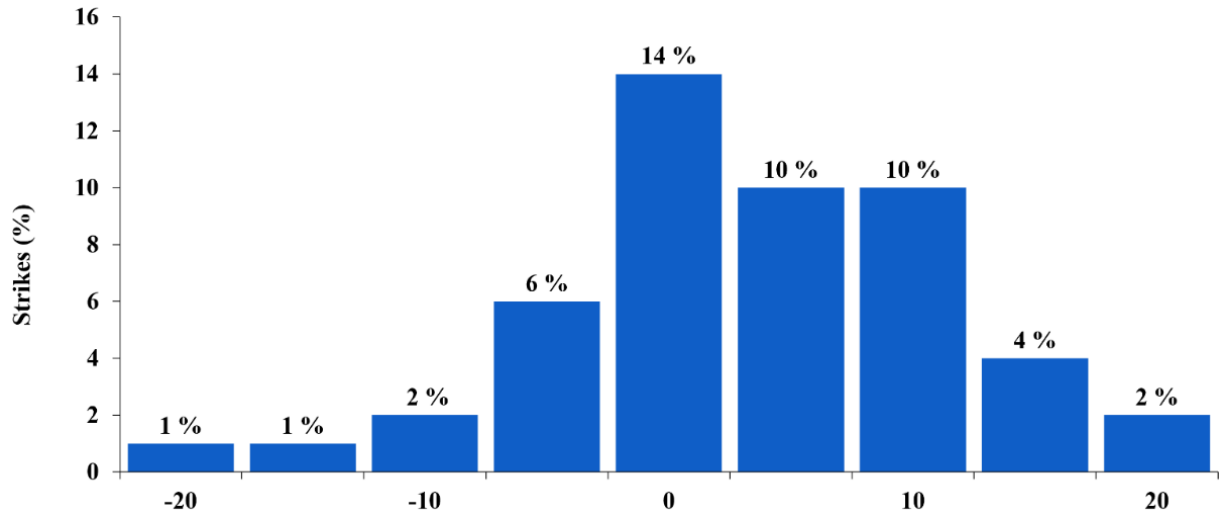

Figure 1.14. Outside air temperatures during lightning strikes (Readapted from [32])

Therefore, considering all the studies and results mentioned above, thunderstorms must be avoided for safe operations, even though modern aircraft are equipped with lightning strike protection systems. This requires a combined effort from airline crews, dispatchers, air traffic controllers, and weather services. Established procedures include circumnavigating around a visible thunderstorm, maintaining a distance of no less than twenty-five miles from regions of significant precipitation, and flying over thunderstorms and cloud formations [31].

Based on data collected from the 50s until the mid-70s, it is anticipated that a commercial aircraft is struck by lightning once every 3000 flying hours, with the data represented in Table 1-1. Additionally, data concerning military aircraft has also been documented (Table 1-2). It is interesting to note that military aircraft are less likely to experience a lightning strike compared to commercial aircraft. This could be attributed to military aircraft not operating in certain conditions, as well as the lack of data availability, since these incidents are not formally documented unless

substantial damage is observed. Other parameters used to access the data from a different perspective have been reported in [34].

Table 1-1: Incidence of Reported Lightning Strikes to Commercial Aircraft [33]

	Newman (1950 – 1961)		**Perry (1959 – 1974)**		**TOTALS**		
Aircraft Type	**Strike**	**Hours**	**Strike**	**Hours**	**Strike**	**Hours**	**Hours / Strike**
Piston	808	2,000,000	-	-	808	2,000,000	2475
Turboprop	109	415,000	280	876,000	389	1,291,000	3320
Jet	41	427,000	480	1,314,000	521	1,741,000	3340
ALL	958	2,842,000	760	2,190,000	1718	5,032,000	2930

Table 1-2: Reported Lightning Strikes to USAF Aircraft;
(mean hours between lightning strikes) [33]

Aircraft Type	**1965**	**1966**	**1967**	**1968**	**1969**	**Average/year**
Bomber	55 500	48 000	47 900	73 000	28 000	50 480
Cargo	68 000	140 000	112 000	124 000	76 000	104 000
Fighter	141 000	105 000	112 000	65 000	73 000	99 200
Trainer	246 000	378 000	500 000	224 000	130 000	295 600

1.2.3 Lightning Strike Mechanism

1.2.3.1 Experimental Studies

Three key research programs from the 1970s and 1980s have played a critical role in explaining the phenomenon of lightning strike interaction and aircraft [35]:

1. NASA Storm Hazards Program using the F-106 aircraft (Figure 1.15); United States of America 1978 – 1986.

2. United States Air Force / Federal Aviation Administration Lightning Characterization program with the CV-580 aircraft, United States of America 1984-1985
3. Office National d'Études et de Recherches Aérospatiales (ONERA) – CEV Transall program using the C-160 in France, 1984 and 1988

Laroche et. al [36] in their review paper provide further details about the experimental studies conducted by these research programs, discussing the methodology, aircraft details, and summarizing some key results. A much more detailed data analysis, summary, and explanations can be found in Uman and Rakov [17], Lalande et al. [37] and Heeter [38].

Figure 1.15. NASA F-106 aircraft [36]

These campaigns included in-flight measurements using instrumented aircraft that flew deliberately into regions with thunderclouds, intending to be struck by lightning. The data collected during these flights have enhanced our understanding of the processes and the mechanisms that lead to the interaction between lightning and airplanes. Subsequently, this led to the development of the bidirectional theory. This theory explains the mechanism by which lightning is initiated by

a conducting object that is not connected to the Earth, such as an aircraft or other airborne vehicles, and is discussed in the following section. An aircraft struck by lightning usually shows three features: a bright and often blinding flash, a loud “boom” sound, and minor damage to the aircraft [17].

1.2.3.2 Initial Lightning Attachment: Naturally Occurring Lightning Strike

To begin with, when a lightning flash forms naturally, a stepped leader originates from a cloud charge center and propagates outward. Although the flash originates at that moment, the destination, which may either be an opposing charge center within the cloud or the ground, remains undetermined. The potential difference between the origin (stepped leader) and the destination (opposite charges) establishes an electrostatic force field between them, represented by imaginary lines depicting equipotential surfaces in Figure 1.16. This field then ionizes the air and leads to the formation of a conductive path, thus becoming the lightning leader. The intensity of the field is greatest where the equipotential surfaces are closest, making it more likely for the leader to move toward the region with the most extreme intensity [39].

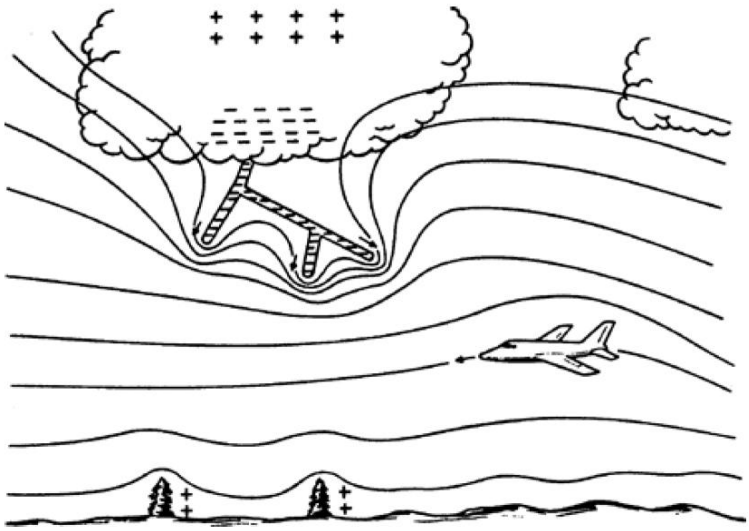

Figure 1.16. Stepped Ladder approaching an aircraft [33]

In cases where an aircraft is in the vicinity, it is assumed that the aircraft adopts the electric potential of that location. An aircraft is conductive in nature, implying that all external surfaces are at the same potential. As the aircraft moves through this electric field, it diverts and compresses local equipotential fields, thereby intensifying the electric field near the extremities of the aircraft.

This can be seen in Figure 1.17. The aircraft's extremities typically include the nose, wing & tail tips, propeller blades, and small protrusions such as antennas. If this occurs far away from the advancing leader, it has negligible effects. However, when this phenomenon occurs within a few hundred meters of the leader, a junction leaders form at the extremities of the aircraft, which moves towards the direction of the lightning leader and attracting it towards the aircraft as depicted in Figure 1.18.

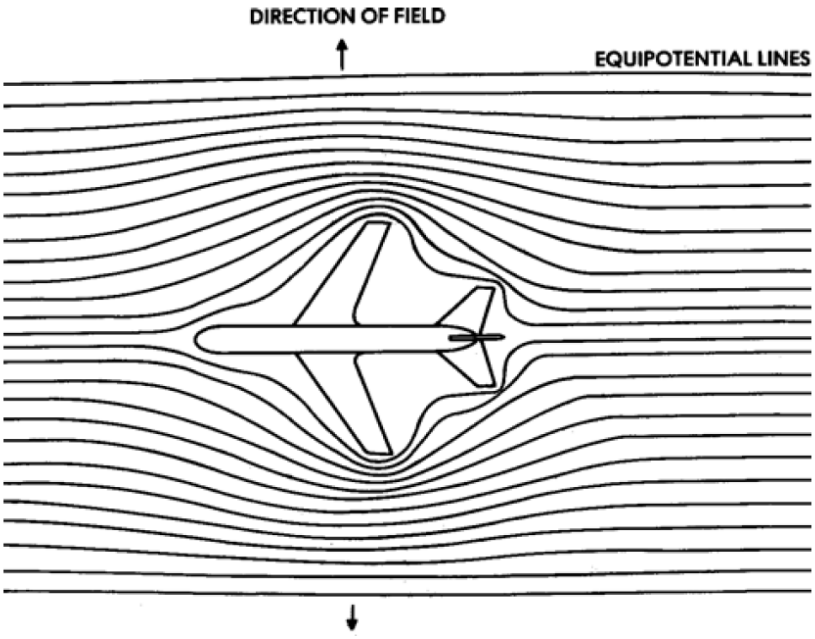

Figure 1.17. Intensification of Aircraft Electric Field around an Aircraft [33]

Simultaneously, the intensity of the electric fields increases, and the lightning and junction leaders continue moving towards each other as in Figure 1.18. The extremities of the aircraft from which the junction leader originates are called initial attachment points [40]. When the electric field near an extremity reaches a value of 30 kV/cm (Sea level pressure), the air ionizes, leading to the formation of electric sparks called streamers at the extremities in the direction of the oncoming lightning leader. When the junction leader encounters the lightning leader or one of its branches, it leads to the formation of a continuous spark from the cloud center to the aircraft (see Figure 1.19). Therefore, an aircraft in proximity to such a system is highly likely to attach to a branch of the lightning leader system [33].

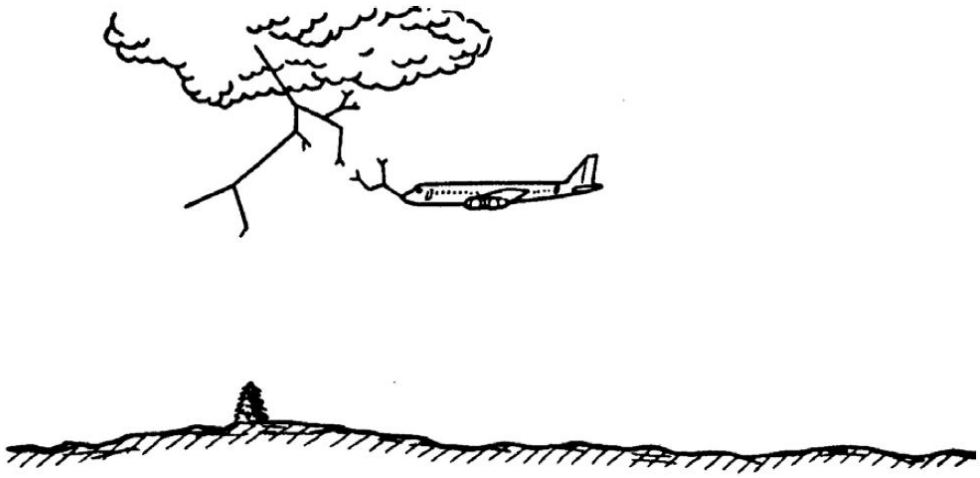

Figure 1.18. Stepped leader attachment to aircraft: Natural leader approaching aircraft. Junction leader responds from aircraft [33]

Since the aircraft cannot store any significant part of the leader's charge, it leads to the formation of branches that exit from the aircraft, becoming an extension of the lightning channel. Thus, the lightning channel continues through the aircraft towards its destination, i.e., the region of opposite polarity. These exit branches propagate from opposite extremities of the aircraft, splitting the developing lightning leader. The branches continue to propagate independently until one of them reaches its destination. Once the leader reaches its destination, it indicates that a continuous ionized channel has been formed, allowing the leader to discharge to the earth. Any subsequent stroke current must flow through the aircraft, which is now a part of the conducting path, thereby forming the lightning channel (Figure 1.20) [30].

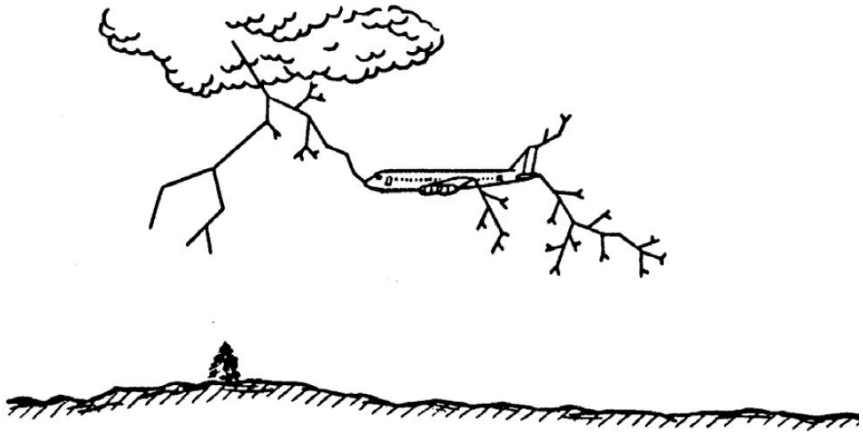

Figure 1.19. Stepped leader attachment to aircraft: Attachment and continued propagation of both branches of natural leader [33]

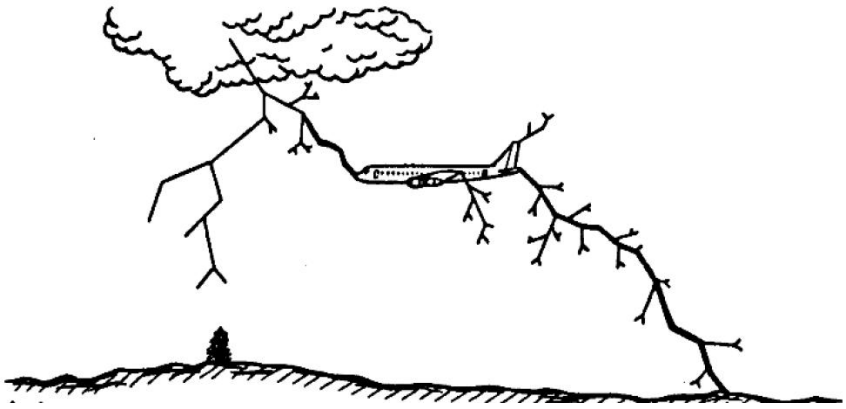

Figure 1.20. Stroke passing through an aircraft as the leader discharges [33]

However, there may exist a scenario in which an alternative branch of the lightning leader reaches the ground before the branch that has flowed through the aircraft. If that occurs, the return stroke discharges through the former branch, thereby reducing the current flowing through the aircraft, as seen in Figure 1.21 [41].

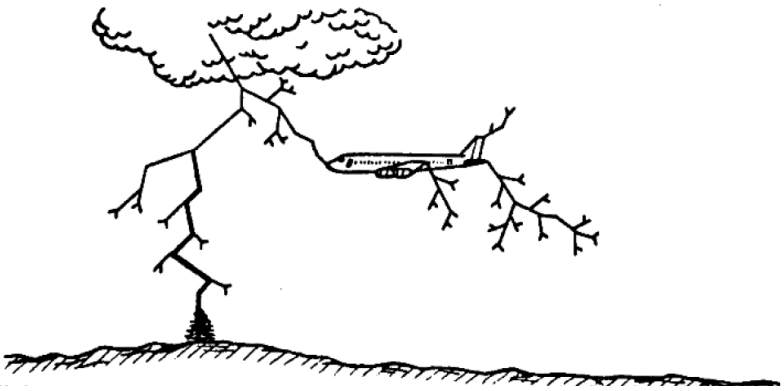

Figure 1.21. Main Stroke not passing through aircraft, only branch current discharges through aircraft [33]

1.2.3.3 Swept Channel Process

After an aircraft is struck by lightning, it becomes part of the conductive path (also known as flash channel or lightning channel), and currents in the channel flow through the aircraft. It is assumed that the lightning channel remains stationary in the air, even though the aircraft is in motion. This situation implies that there is a relative motion between the aircraft and the lightning channel. Even though the lightning flash may exist for a duration of one second, the speed of a typical aircraft allows it to move a significant distance, perhaps even the entire length of the fuselage channel, leading to multiple initial entry and exit points across the surface of the aircraft. As shown in Figure 1.22. The initial attachment point is the pitot tube, and as seen, due to the movement of the aircraft, the channel sweeps back. This is known as swept flash phenomena, otherwise referred to as swept stroke. Because of this sweeping action, the lightning channel attaches and dwells at various locations on the surface along the line of flight and behind the initial attachment point. These points are known as dwell points. Due to the sweeping phenomena, not all the current in a lightning flash is delivered to a single point, which becomes an important design criterion [30], [33], [35].

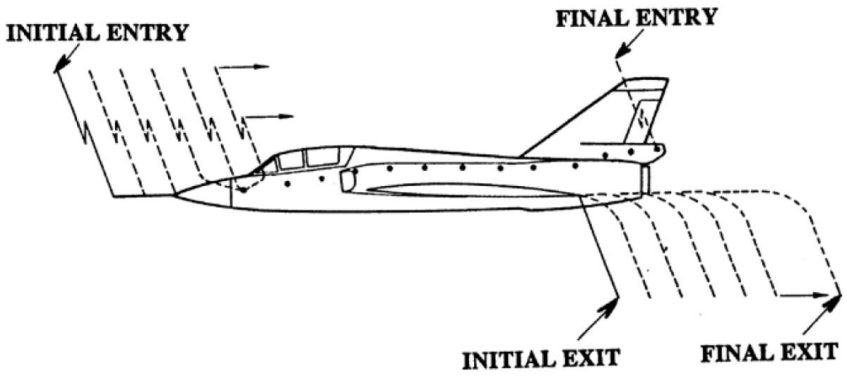

Figure 1.22. Typical path of swept channel attachment points [33]

The aircraft typically does not usually fly out of the channel, as the potential difference between charge centers is sufficient to maintain a prolonged channel until the charges have neutralized each other and the flash dies [39]. During this process, pilots occasionally report short-lived interference in their instruments and flickering of lights [31]. Since the lightning channel sweeps over complex geometries, such as an aircraft, it can cause deformation of the channel. This deformation is particularly dependent on several parameters, including aerodynamic flow and plasma properties.

The channel may approach other parts of the aircraft, potentially leading to reattachment if the potential difference is sufficient to initiate a dielectric breakdown between the aircraft and the lightning channel. The attachment point makes a jump. Subsequently, two phenomena can occur: either the attachment point could dwell at the same spot, moving with the aircraft, or the attachment point sweeps along the surface. However, reattachment may occur if there is a dielectric breakdown due to the potential difference across the channel, coupled with significant deformation. This phenomenon can be seen in Figure 1.23 and Figure 1.24.

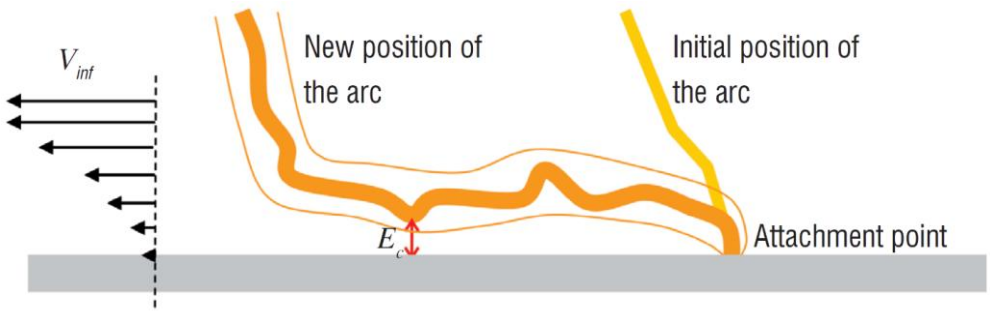

Figure 1.23. Deformation of lightning channel [42]

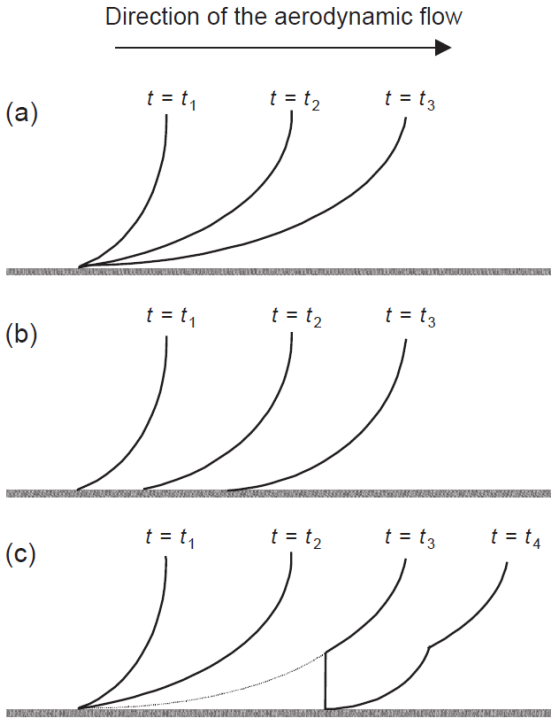

Figure 1.24. Swept-Stroke Phenomena [35]

1.2.3.4 Initial Lightning Attachment: Triggered Lightning

An aircraft can trigger lightning when the local electric field induces a charge on its extremities. This in turn leads to the production of an electric field that can cause the air to break down at various sections of the aircraft. The static electric field around the aircraft must be properly

oriented and be sufficiently large so that the locally enhanced fields at any point on the aircraft exceed the local breakdown strength of the air. These field enhancements usually occur at sharp points or edges, particularly if such points and edges are aligned with the ambient field. The surrounding electric field should be at a sufficient distance to enable the formation and propagation of streamers. If the local electric field is high enough, streamers develop and propagate away from the aircraft, evolving into bi-directional leaders (Figure 1.25). These leaders then propagate between regions of opposite polarity, resulting in the development of lightning current through the airplane [30],[33],[40].

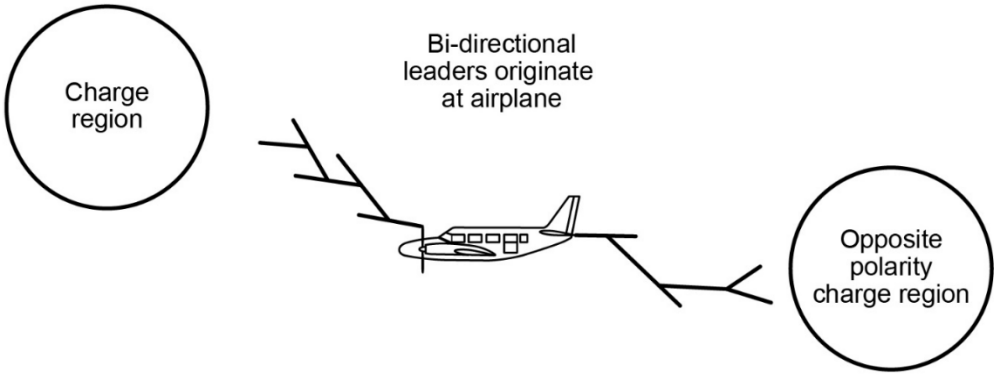

Figure 1.25. Stepped leader attachment to aircraft [40]

1.2.4 Effects of Lightning Strikes

The effects of lightning strikes on aircraft can be categorized into two main types: direct and indirect. The former is associated with actual physical damage that can occur at the attachment point, while the latter relates to the operation of onboard electronic systems as a result of associated electromagnetic phenomena [43].

1.2.4.1 Direct Effects

1. Thermal Damage

   Thermal damage is an immediate and visible effect of a lightning strike on an aircraft. Upon attachment to the aircraft's surface, the channel is extremely hot, reaching temperatures of 50,000 degrees Fahrenheit, which leads to localized heating. This phenomenon may cause resin melting, burning, charring, delamination, and vaporization of the material. Metallic structures may develop holes, whereas composite structures are subjected to matrix degradation and fiber breakage. Additionally, hot spots may form on the surface of the internal aircraft skin, located immediately opposite the lightning attachment point, and are considered significant primarily due to the potential for fuel ignition or the presence of highly flammable vapors. The vaporization of conductors may lead to explosions, especially if the associated cross-section is not large enough. This leads to the formation of a shock wave, which can severely damage within a confined space. This is particularly important in the case of wiring connected to external equipment such as light, antennas, and pitot tubes [40],[44].

2. Structural Damage

   Structural damage occurs when mechanical forces associated with a lightning strike physically compromise the aircraft structure. Such forces may emerge from rapid thermal expansion, electromagnetic forces between current paths, shockwaves generated by the sudden heating of air, and vaporization of materials. The channel of air through which the

lightning flash propagates is instantaneous and reaches significantly high temperatures. The resulting shock wave impinges on the surface, leading to mechanical damage [45]. In metallic aircraft, this may lead to riveting failures, skin cracking, or tearing. In composite structures, the situation is more severe: high localized currents can cause fiber damage (fracture, blowout), matrix damage (cracking), interlaminar delamination, and through-thickness penetration [46],[47],[48],[49].

3. Fuel System

Fuel system hazards represent some of the most catastrophic risks associated with direct lightning effects. In the event that lightning-induced currents penetrate fuel tanks or their associated systems, they may create sparks or localized heating capable of igniting flammable fuel-air mixtures. Historical incidents and laboratory testing have shown that small arcs or hot surfaces inside a fuel tank are sufficient to cause explosions. Consequently, modern aircraft are designed with extensive protection such as bonding of fuel system components, use of lightning-resistant sealants, inerting systems (using nitrogen gas to reduce oxygen levels inside tanks), and lightning-proof venting systems [50],[51],[48].

4. Surface Markings and Erosion

Surface markings and erosion are the most prevalent visible evidence of lightning strikes. Typical indicators include small entry and exit pits, surface pitting, soot marks, and localized burn-throughs, which are usually found at aircraft extremities, such as radomes, wingtips, stabilizer tips, and tail cones. While these markings often indicate relatively

minor damage, their presence requires careful and thorough inspections as deeper structural damage or hidden composite delamination may exist beneath seemingly superficial damage [52],[44].

1.2.4.2 Indirect Effects

1. Electromagnetic Coupling

   Electromagnetic coupling occurs when the strong electric and magnetic fields generated by a lightning strike induce voltages and currents in the aircraft's internal wiring and avionics, even without direct physical contact. These induced effects can disrupt the operation of critical systems such as flight controls, navigation sensors, communication radios, and other sensors. The threat can be catastrophic in modern aircraft that rely heavily on fly-by-wire systems, where small perturbations in signal integrity can cause major operational issues. Electromagnetic coupling can lead to transient faults, data corruption, or, in the worst cases, permanent hardware damage [53],[54]. These currents can flow along the shields of control cables or into the bodies of sensors and actuators, producing erratic or incorrect control commands. In critical flight phases, such as takeoff or landing, even a brief disruption can pose severe risks. Failures may manifest as spurious control surface movements, autopilot disconnection, or trim changes [55], [56],[57].

2. Transient Voltages and Electrical Surges

   Transient voltages and electrical surges are induced when lightning energy couples with power distribution systems and electronic wiring, producing sharp voltage spikes that far exceed normal system tolerances. These surges can instantaneously damage or destroy

sensitive avionics, flight control computers, and other electrical equipment. Even without immediate destruction, surges can weaken components, leading to latent failures weeks or months later [55],[57].

1.2.5 Lightning Strike on Composite Materials

At this stage, it can be asserted with a degree of certainty about the challenges posed by lightning to aircraft and airborne vehicles; however, its effects may not be limited to just that. Infrastructure and energy projects, such as wind turbine blades, are also susceptible to damage from lightning strikes. Moreover, it is necessary to specifically understand the effects and damage mechanisms resulting from lightning strikes on composite materials. Aircraft with metallic construction, such as aluminum, demonstrate greater resilience to lightning strikes. When struck, the electrical current disperses over the exterior surface and exits at another extremity, which typically does not inflict significant damage. This notably reduces localized heating and damage due to penetration. Due to poor bonding, structural continuity, or fasteners, the effects of lightning may lead to arcing, burning, or pitting. Nevertheless, internal systems are just as vulnerable to indirect effects [58],[59],[60].

Composite structures do not conduct electricity as readily as their metallic counterparts, particularly in the event of a lightning strike. This is primarily attributable to differences in electrical properties. While carbon fiber by itself is conductive, the polymer matrix functions as a dielectric, which consequently diminishes the overall electrical conductivity of the composite material. As a result, the electrical conductivity within the material is high in the fiber direction, while through the thickness, its value is determined by the polymer matrix [61]. As materials with

low electrical conductivity typically tend to absorb more electrical energy, the undispersed current during a lightning strike leads to vaporization or delamination in CFRP composites [62],[27].

1.2.5.1 Lightning Strike Damage Mechanism

- Joule Heating: The electric resistance exhibited by composite materials in both the transverse and through-thickness directions causes the lightning current to be converted into thermal energy, which significantly increases the temperature of the composite. This temperature rise often leads to thermal, mechanical, and chemical consequences [63],[64]. It may result in the ablation or sublimation of carbon fibers, resin charring and melting, or corrosion of coatings. Such damage is typically observed as blackened or charred and can extend through multiple plies [65], [66].

- Matrix Decomposition: The rapid increase in temperature from Joule heating, which can reach up to 3316 °C, initiates the decomposition of the matrix that begins around 300 °C by a process called pyrolysis [67]. As a result, the matrix loses its cohesion, thereby weakening the composite structure while concurrently undergoing an exothermic reaction that generates gases that get trapped within the interlaminar layer due to the low permeability of CFRP; these gases cannot escape. This leads to exceedingly high interlaminar pressure, ultimately resulting in an internal explosion that causes fiber breakage, matrix cracking, and delamination. This is also referred to as “gas blow off” [64],[65].

- Shock Wave (Acoustic Force): The phenomenon of Joule heating, resulting from the lightning current, causes the surrounding air to experience increased temperature and pressure. This leads to the rapid expansion of compressed, high-temperature air, consequently generating an acoustic shockwave that propagates at supersonic velocities. When this shock wave occurs, it can impart mechanical stress to the composite material. This is known to be a primary contributor to mechanical damage, resulting in surface cratering and cracking [68],[69].

- Dielectric Breakdown: When a CFRP structure is subjected to an electric field during a lightning strike event, it exceeds the dielectric strength of the matrix. The polymer initiates ionization, thereby resulting in the formation of internal arcs that degrade the material, leading to internal delamination and resin charring. Moisture and defects in the structure can further aggravate the damage, as they tend to reduce dielectric strength [70],[71].

- Magnetic Forces (Lorentz Force): The electric current resulting from lightning generates a magnetic force around the strike zones. This force interacts with the current flowing in the carbon fibers and produces Lorentz forces that act perpendicular to the current. Although this force is transient, lasting merely a few seconds, it induces hoop stresses that may result in the displacement or compression of fiber bundles, leading to matrix cracking [72].

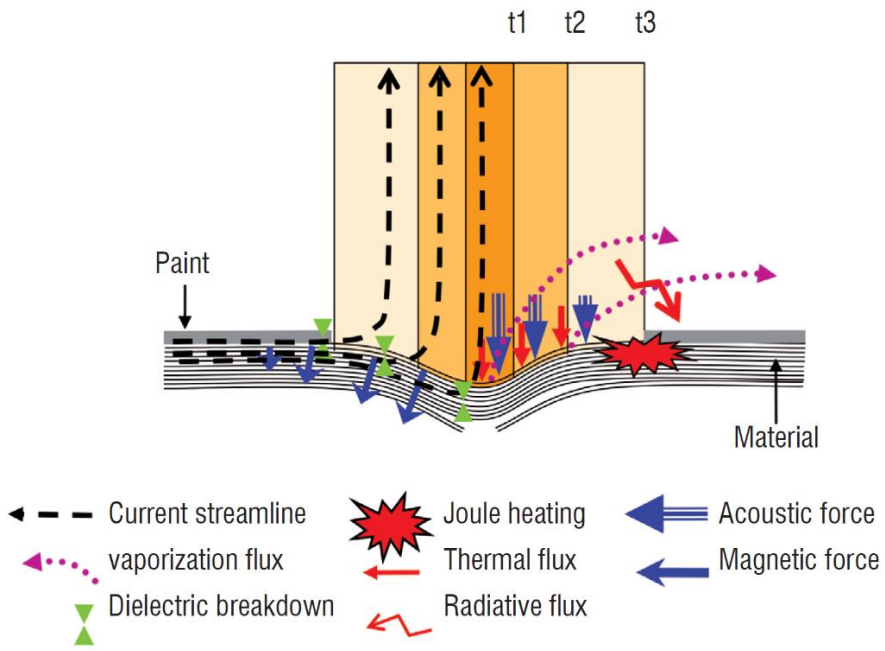

Figure 1.26. Damage Characteristics [35]

1.2.6 Lightning Strike Protection Systems

Damage to composite material structures caused by lightning strikes can have detrimental consequences and may lead to structural failure, as discussed above. This necessitates the implementation of a lightning strike protection (LSP) solution that directs the flow of lightning current and associated electromagnetic forces through the aircraft protection system, allowing it to exit towards the ground without inflicting damage on the structure. Current travels through the shortest and most conductive path possible from the initial attachment point until its exit at an extremity. The primary objective of an LSP is to establish a safe, electrically conductive path on the exterior of the structure that allows the current to remain on the exterior and exit, thereby reducing the thermomechanical damage [73]. Choosing an LSP is a complex process that requires consideration of several technical and commercial factors, such as protection effectiveness, electrochemical compatibility with composite material, adhesiveness, additional weight, cost, and manufacturing and repair complexity [74].

Some lightning strike protection systems that are currently in use and under development are discussed briefly below:

1. Metallic Expanded Foils: These are flat, thin pieces of metal that typically exhibit a thickness ranging from 50 to 100 micrometers and are arranged in a lattice-like pattern. These systems are positioned atop the laminates and are safeguarded by a protective dielectric coating, such as a layer of paint, thereby facilitating the dissipation of lightning strike energy [74].

2. Metallic Meshes: Metallic Meshes are the preferred solution for effective LSP. They are usually integrated in the outer layer of the structure and impregnated with adhesive or sandwiched between adhesive films. Metallic Meshes limit damage to a minimal surface area without significant depth penetration. The division of the lightning arc achieves this into many conductive filaments, which in turn disperse the lightning energy over a wider area. However, they can add a significant amount of weight up to 150 – 200 g/m^2. Metallic wires may also be woven in the outer ply of a CFRP laminate [73],[74],[75].

3. Metallic Coatings and Conductive Paints: Metals can be coated with non-metallic substrates using various techniques such as physical vapor deposition or thermal spraying. The sprayed metal solidifies on the surface, resulting in a hard and rigid conductive layer that requires further processing for additional surface finishing. Paints that are typically non-conductive are used for environmental protection and aesthetic purposes. The addition of conductive metallic particles or carbon allotropes to a polymer matrix results in the

production of conductive paint. Adding special pigments can create ionizable paints as well. The use of this technology is limited due to the loss of electrical conductivity when exposed to the environment as well as processing and solubility issues [73],[74].

4. Carbon-Based LSP Solutions: Conductive carbon materials have emerged as an alternative to metallic systems, offering good conductivity and ease of processing. Using nanofillers such as carbon nanotubes or carbon black can significantly enhance conductivity and strengthen the material, while reducing damage associated with a lightning strike. Graphene exhibits excellent properties, including high conductivity, light weight, and hydrophobicity, making it an ideal material for use in the aerospace industry and a suitable solution for an LSP system. To scale up the use of graphene LSP, focus needs to be spent on enhancing performance, addressing delamination, reducing costs, and improving integration [75],[74].

The primary challenge in replacing current metallic mesh technology is finding an alternative material with a high conductivity-to-density ratio. In addition, the material should be repairable, manufacturable, and easy to maintain. Therefore, the overall trend of research is towards the enhancement of electrical conductivity of structures by the addition of nanoparticles, nanowires or carbon allotropes [73].

1.3 Lightning Strike Testing Standards

There are several testing and certification standards; a non-exhaustive list is shown in Table 1-3. The current industry standard has been the SAE Aerospace Recommended Practices Series, specifically ARP 5412, 5414, and 5416. Each of these has been instrumental in defining the

parameters aligned with experimental studies to establish a consistent testing regimen. These standards will be discussed in detail in this section. These three documents cover the whole spectrum of aircraft lightning interaction (Figure 1.27).

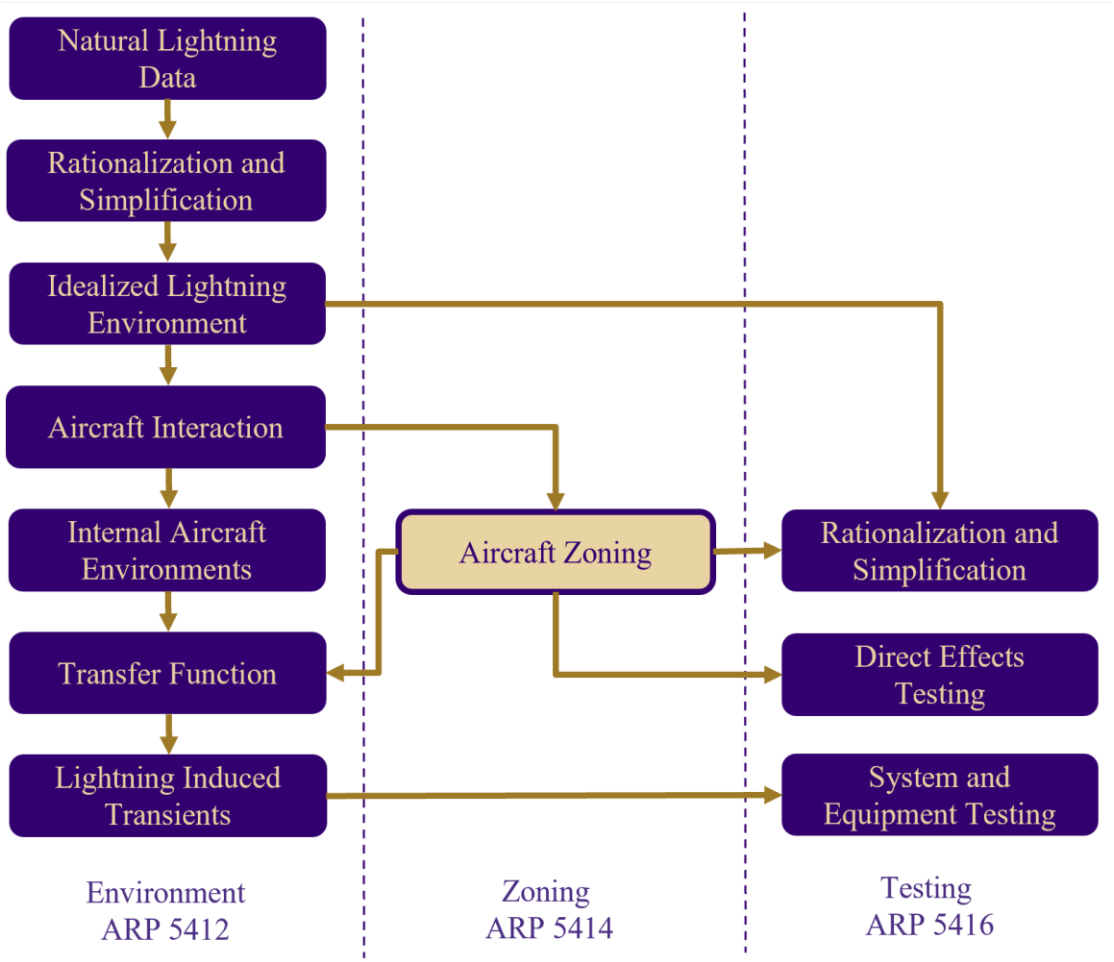

Figure 1.27. Relationship between Aircraft Environment (ARP 5412), Zoning (ARP 5414), and Testing (ARP 5416) (Readapted from [40])

Table 1-3: Lightning Strike Test Standards

S. No.	Standard	Title	Organization
1	SAE ARP 5412C	Aircraft Lightning Environment and Related Test Waveforms	SAE International [76]
2	SAE ARP 5414 B	Aircraft Lightning Zoning	SAE International [40]
3	SAE ARP 5416 B	Aircraft Lightning Test Methods	SAE International [46]
4	SAE AIR 5662	Lightning Indirect Effects Testing Handbook	SAE International [77]
5	SAE ARP 5577	Aircraft Lightning Direct Effects Certification	SAE International [78]
6	ED-14G	Environmental Conditions and Test Procedures for Airborne Equipment	EUROCAE [79]
7	ED-84	Aircraft Lightning Environment and Related Test Waveforms	EUROCAE [80]
8	ED-105	Aircraft Lightning Test Methods	EUROCAE [81]

1.3.1 SAE ARP 5412

This document characterizes the lightning encountered by an aircraft by defining idealized waveforms referred to as the aircraft lightning environment. This quantification and standardization offer consistency to regulators, particularly in the certification of systems and structures. The current and voltage waveforms are intended to represent the external lightning environment and differ from the actual waveform observed during in-flight testing, as discussed in Section 1.2.3.1.

A typical current waveform observed during in-flight testing is shown in Figure 1.28. A continuous current of 1 A is formed by the positive leader lasting a few milliseconds, which is followed by a train of 10 pulses at a repetition rate of 250 microseconds, having a peak amplitude of 850 A,

generated by the negative leader. Subsequently, there is a continuous current with a magnitude of 330 A for about 200 milliseconds. The waveform ends with 15 pulses, which may occur either after or simultaneously with the continuous current, and it can have a peak magnitude of as high as 20 kA [36].

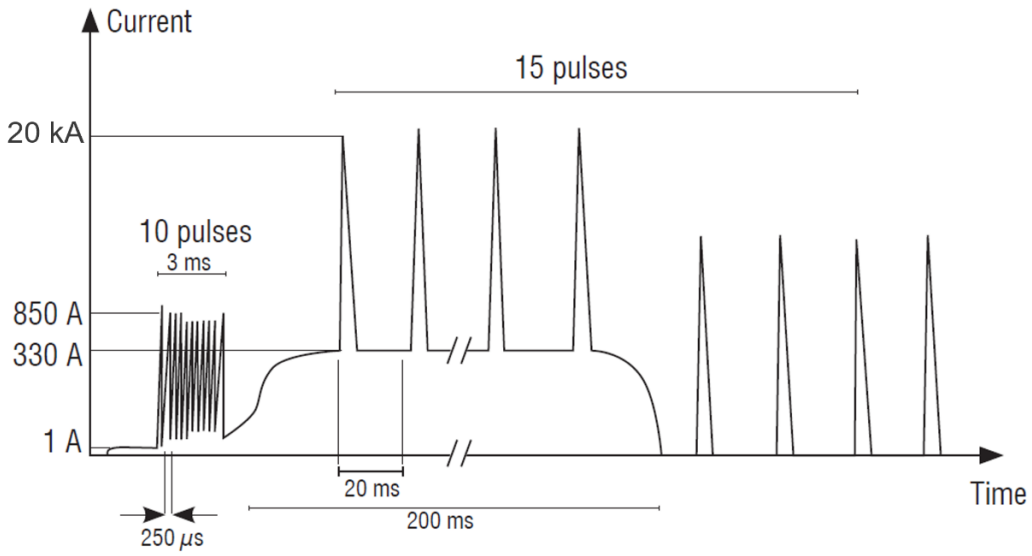

Figure 1.28. Typical Current Waveform observed during in-flight testing [36],[82]

The waveform as defined in SAE ARP 5412 [76] represents an idealized environment intended for analysis and testing of an aircraft. These waveforms typically do not represent a particular lightning event, but rather describe the waveforms whose effects the aircraft will encounter during a lightning event. There are components of both voltage and current waveforms designed to characterize a natural lightning event. Some important parameters to evaluate direct effects are:

1. Peak Current Amplitude: The maximum amount of electric current that can flow during a lightning strike. A 10% increase in magnitude corresponds to a 15.2% increase in thermal damage depth as per Millen et. al. [83].

2. Action Integral: The measure of energy delivered by the lightning current over time. It is a critical factor to quantify the extent of damage. This parameter shows a strong correlation with the measure of damage [83]. It is represented mathematically by Eq.1-1

$$\text{Action Integral} = \int I(t)^2 dt \qquad 1\text{-}1$$

3. Time Duration: The length of time over which a specific component of the lightning current is applied to the aircraft.

Figure 1.29 shows the idealized current waveform for evaluating direct effects comprising Components A, B, C, and D. Important parameters pertaining to these components are mentioned in Table 1-4. Component A encapsulates the severe parameters experienced during the first return stroke, negative subsequent strokes, and the positive return stroke, representing the pulse that an aircraft can experience when flying at lower altitudes. For testing component A waveform can be simulated as an oscillatory or unidirectional waveform. Component B is for the intermediate current that is observed after a negative return stroke. This waveform is crucial, as it has been observed to puncture thin wing skins, which are often used to cover fuel tanks. It should be plotted as a unidirectional waveform.

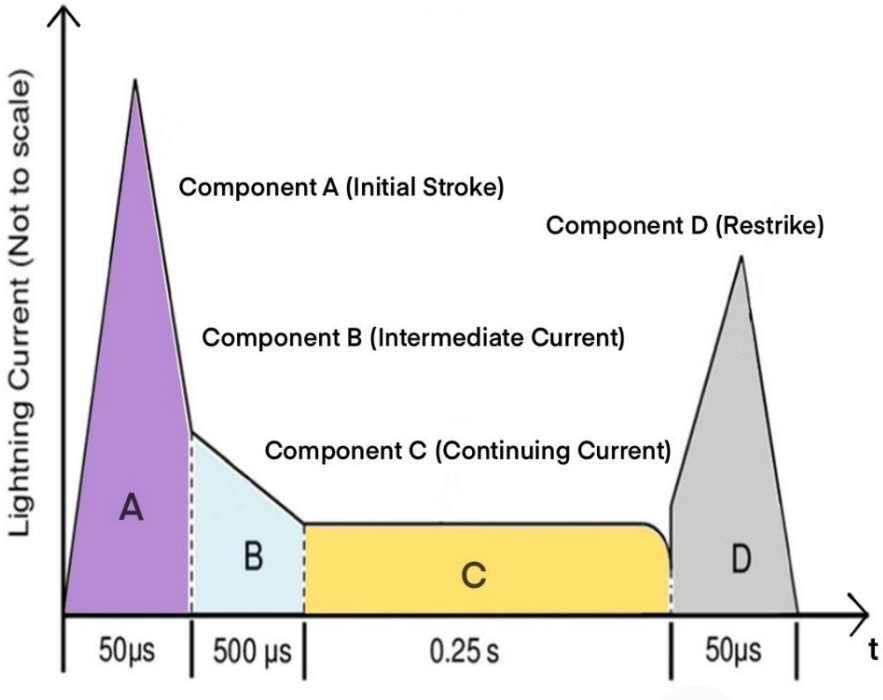

Figure 1.29. SAE ARP 5412 Standardized Current Waveform (Readapted from [36],[82])

Component C represents the long-duration lightning current, particularly the subsequent strokes of negative cloud-to-ground lightning and the return stroke of positive cloud-to-ground lightning. The standardized waveform should be depicted as a square or rectangle. Waveform D can be utilized to test both direct and indirect effects. Specifically for direct effects, it accounts for subsequent return strokes. Component D may be represented as unidirectional or oscillatory. Further details about the waveform representation and application can be found in SAE ARP 5412C [76].

It is noteworthy that each damage mode exhibits a strong correlation with a specific lightning parameter. Fiber damaged area and damage thickness are governed by the peak current of the

lightning stroke, while the resin deterioration area and the delamination projection area are determined by the electrical charge and the action integral of the waveform, respectively [84].

Table 1-4: SAE ARP 5412 Current Components [76]

Component	Nomenclature	Parameters	
A	First Return Stroke	Peak Amplitude: Action Integral: Time Duration:	200 kA (+/- 10 %) 2 x 10^6 A^2s (+/- 20 %) (in 500 μs) ≤ 500 μs
B	Intermediate Current	Max. Charge Transfer: Average Amplitude: Time Duration:	10 Coulombs (+/- 10 %) 2kA (+/- 20 %) ≤ 5 ms
C	Continuing Current	Amplitude: Charge Transfer: Time Duration:	200 – 800 A 200 Coulombs (+/- 20 %) 0.25 to 1 s
D	Subsequent Return Stroke	Peak Amplitude: Action Integral: Time Duration:	100 kA (+/- 10 %) 0.25 x 10^6 A^2s (+/- 20 %) (in 500 μs) ≤ 500 μs

1.3.2 SAE ARP 5414

This document defines lightning attachment zones and outlines the procedure for locating and identifying these zones. This is a necessary exercise to ensure that the aircraft has adequate protection against both direct and indirect effects. The classification of zones is done based on the likelihood that a surface might experience lightning channel attachment. This should be performed in addition to hazard assessment to determine the protection required for a particular region, as well as systems such as fuel. It is a two-step process: determining the point of initial attachment and then locating the attachment point after the first one. A detailed flow chart is shown in Figure 1.30.

The aircraft is divided into three zones as follows:

1. Zone 1: Regions that are likely to encounter the lightning attachment and the first return stroke.
2. Zone 2: Regions which are unlikely to encounter the first return strokes; however, they are likely to encounter the following return stroke. This is particularly important during the swept channel process, as discussed in Section 1.2.3.3.
3. Zone 3 refers to the regions that would not experience a lightning strike during the initial attachment and sweeping process, but will conduct lightning between the attachment points.

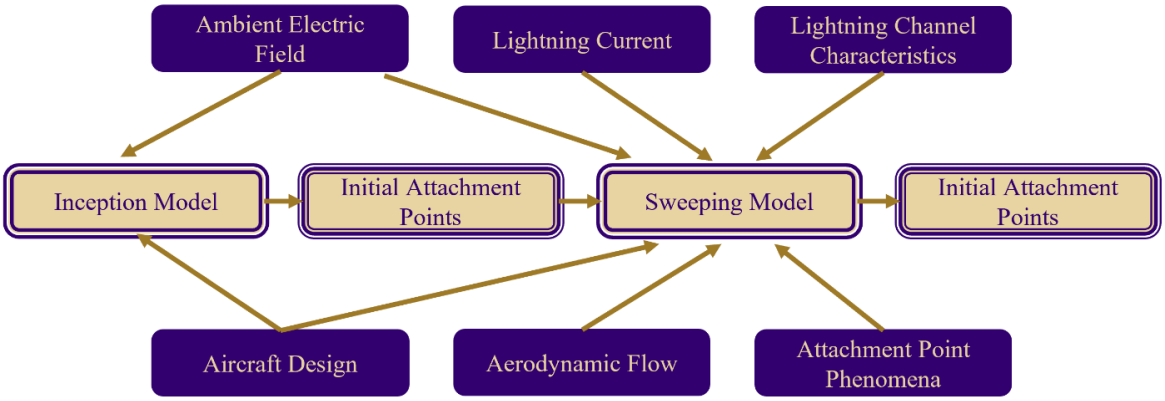

Figure 1.30. Process of Zoning an Aircraft (Readapted from [35])

There is a further classification for Zones 1 and 2 in A and B. Zone 1A and 2A are for regions where a long hang-on is unlikely, as due to the motion of the aircraft, the attachment point will move across the length of the aircraft. On the other hand, Zones 1B and 2B are for regions where the lightning channel attachment point is unlikely to shift because the location is a trailing edge where it cannot sweep further. There is also a 1C classification referring to the change in current

parameters and time taken to sweep the attachment point across the surface, which reduces the threat to the aircraft. All the zones have been summarized in Table 1-5. Further description on the process of zone location and descriptions is outlined in SAE ARP 5414 [40]. Figure 1.31 depicts the zoning for a typical commercial aircraft.

Table 1-5: SAE ARP 5414 Aircraft Zoning [40], [85]

Zone	Nomenclature	Description
1A	First Return Stroke Zone (Initial Attach)	Areas of the aircraft where a first return stroke is likely; low expectation of flash hang on
1B	First Return Stroke Zone with long hang on (Discharge Region)	Areas of the aircraft where a first return stroke is likely; high expectation of flash hang on
1C	Transition zone for first return stroke	Areas of the aircraft where a first return stroke of a lower amplitude is likely; low expectation of flash hang on
2A	Swept Stroke Zone	Areas of the aircraft where a subsequent return stroke is likely; low expectation of flash hang on
2B	Swept Stroke Zone with long hang on	Areas of the aircraft where a subsequent return stroke is likely; high expectation of flash hang on
3	Current Conduct Region	Areas not in Zone 1A, 1B, 1C, 2A, 2B where attachment is unlikely; they lie beneath or between other zones

1.3.3 SAE ARP 5416

The final document in the series describes the testing techniques used to evaluate the material under both direct and indirect lightning effects. It is specifically intended for testing aircraft and associated systems. This document should be used in conjunction with a certification plan to be eventually accepted by the relevant regulatory authorities. This document defined three kinds of

tests – Development for non-conforming and off-the-shelf components which does not meet certification requirements but further enhance design refinements, Qualification that is used to certify the overall system and get airworthiness approval, and Certification which contains all the requirements metrics and paperwork required to be submitted to regulatory authorities for aircraft lightning certification package. Detailed descriptions of Direct Effects tests, Indirect Effects tests, and Fuel System tests can be found in SAE ARP 5416 [46].

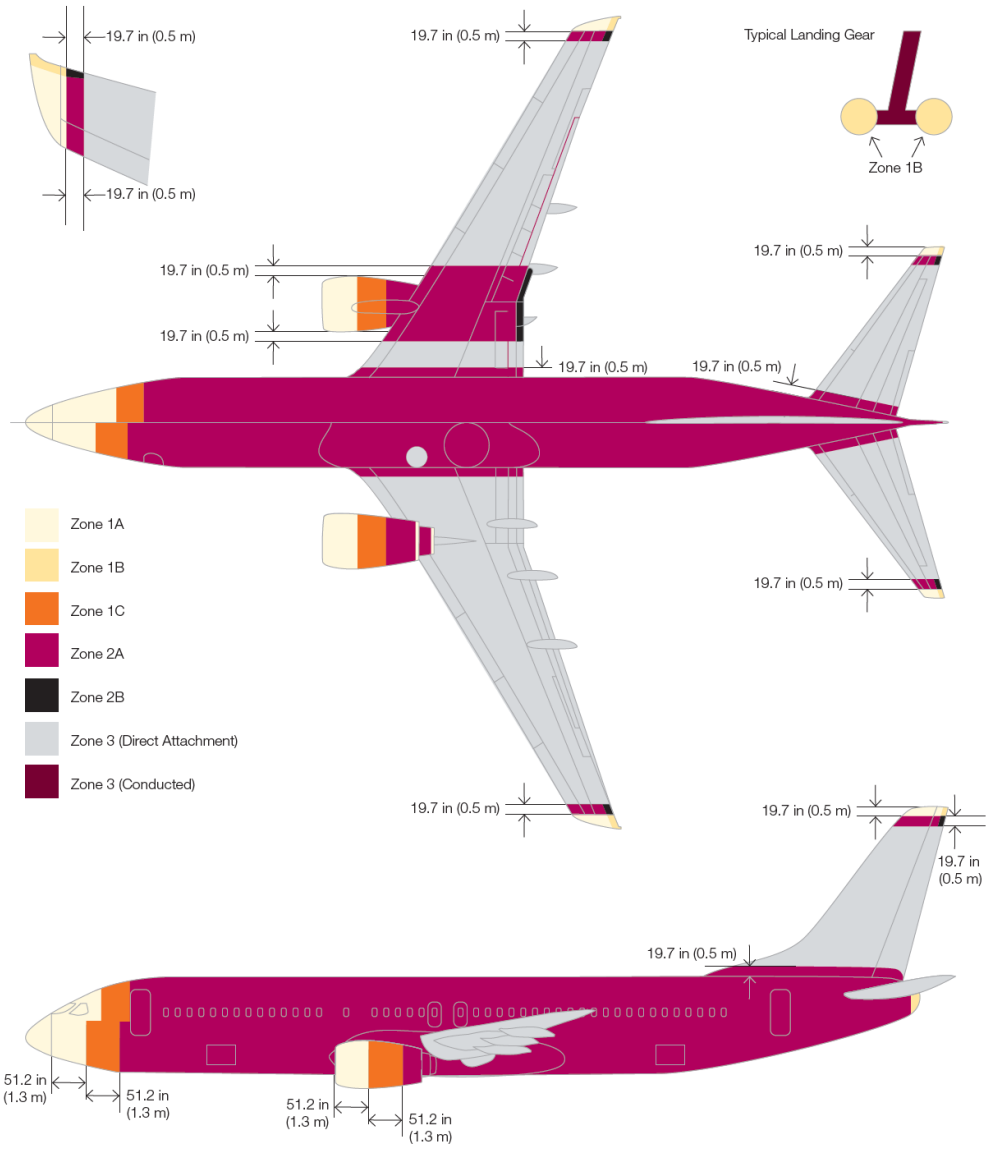

Figure 1.31. Zoning on a typical commercial airliner [28]

1.4 **Literature Review**

1.4.1 Foundational Experimental Papers

Feraboli and Miller [86] define the fundamentals for the current study. To reiterate, the importance of carbon fiber reinforced polymer (CFRP) structures is unmatched primarily due to their high strength-to-weight ratio and enhanced mechanical properties. This, in turn, directly results in increased fuel efficiency, reduced pollution, and decreased acoustic emissions. However, with the introduction of CFRPs in the primary structure of the aircraft, the threat of lightning is significantly greater than that of metallic airframes. Carbon fibers are good conductors by themselves, but in contrast with the polymer matrix, a known dielectric, the resulting material has reduced conductivity. CFRP is particularly vulnerable to direct effects, with its damage mechanism driven by acoustic shock and resistive heating. A lightning arc delivers a large amount of energy, rapidly expanding the ionized channel at supersonic speed, resulting in the formation of a shockwave. When this shockwave encounters a hard surface, its kinetic energy transforms into a pressure rise, leading to delamination. Resistive heating raises the temperature, initiating a breakdown of the resin/fiber interface through pyrolysis. As the resin burns, gas may become trapped within the layers, potentially causing an explosive release and further damaging the structure. This paper assesses the damage to carbon/epoxy prepreg samples subjected to simulated lightning strikes in the range of 10 to 50 kA. The samples have dimensions of 304.8 mm x 38.1 mm with a thickness of 0.18 mm and adhere to Boeing standards for unnotched tension and compression, as well as filled-hole tension and compression. Optical techniques such as visual inspection, ultrasound, and microscopy were employed to observe the morphology of pristine and damaged samples, alongside tension and compression tests post-impact, to quantify the residual strength. The filled hole compression sample exhibited the most significant decrease in compressive strength between the

strikes, and the samples displayed different damage morphologies, indicating that further investigation would be necessary. For the unnotched specimen, damage is limited to the top two to four plies, with a restricted distribution of damage across the surface compared to the sample with the fastener. The author mentions that due to the finite width of the specimen, the damage is confined, and therefore, the study's results may not be extrapolated to larger panels.

In the following paper, Feraboli and Kawakami [87] investigated the equivalence in simulated lightning strikes and mechanical impact, specifically the relative effects of the damage mechanisms. At that time, limited literature was available regarding the damage mechanisms of composite materials under lightning strikes; however, the well-established field of impact damage on composites may provide further clarification on lightning strike damage. This study utilizes a larger specimen with dimensions of 330 x 330 mm compared to previous research to ensure that damage due to lightning strikes is fully contained within the specimen's boundary. The evaluation employs compression after impact tests (CAI), non-destructive inspection methods such as pulse-echo ultrasound C-scan, and destructive inspection through cross-sectioning the sample and optical microscopy. CAI tests indicated higher strength degradation in samples subjected to impact rather than lightning strikes. The projected damage area is circular for impact damage and elliptical for lightning strike damage. Additionally, the damage caused by mechanical impact is greater than that caused by the lightning strike. From microscopic inspection, both specimens exhibit extensive matrix damage attributed to intraply cracks and interply delamination. The electromagnetic–thermomechanical nature of damage due to lightning strikes results from resistive heating that can pyrolyze the resin, causing cracks and burns, as well as electrical conductivity mismatches at the interface of plies, which lead to delamination. The authors determined that the stacking sequence

is influential for analyzing this threat. The equivalence here seeks to equate the energy dissipated in a lightning strike by measuring current and voltage with the impact energy from the impact damage tests. Based on the results of this study, impact damage was deemed a greater threat to carbon/epoxy composite plates than lightning strikes. Furthermore, the energy dissipated by the lightning strike was significantly larger than that from a mechanical impact, making an energy-based comparison impractical. Instead, a threat level parameter was introduced. However, the findings may not be applicable in a broader context due to several limitations, such as the use of pre-preg material, testing of unpainted, unprotected, and filled hole samples influencing lightning strike behavior, and the specimens having a fixed stacking sequence. A similar study was conducted by Soulas et al [88].

Kawakami and Feraboli [89] conducted a series of tests on CFRP samples featuring scarf repair. Since CFRP has significantly lower electrical conductivity, it requires the addition of a lightning strike protection system, such as a metallic wire mesh. This mesh is placed on the outer surface of the structure and effectively dissipates both direct and indirect lightning effects. It can be made from aluminum, copper, or bronze and may be co-woven with carbon fiber prepreg or adhered separately to the outermost laminate layer. The importance of bonded scarf repair is evident, as it entails the removal of the lightning strike protection mesh; thus, any damaged area beneath the electrical flow path may be compromised unless a replacement layer is applied to the outer skin. Results indicated that bonded scarf repair effectively restores structural integrity [90]. Standard procedures advise against overlapping the mesh, as this would lead to surface irregularities that adversely affect aerodynamic characteristics and require extensive sanding for finishing and painting. The samples used in this study measure 305 mm x 102 mm, with a layer of copper wire

mesh placed on top for lightning strike protection. Some samples underwent scarf repair according to established procedures, resulting in either satisfactory or unsatisfactory outcomes based on whether full electrical conductivity was achieved. The specimens are coated with aircraft-grade acrylic paint, creating an effective dielectric on the surface. Visual inspection, micrography, and ultrasonic C-scans were employed to evaluate specimen damage on the surface, alongside four-point bending tests to assess residual strength. The findings indicated that copper mesh protection significantly influences damage areas by preventing electric discharge from harming the underlying carbon fiber piles. Specimens lacking copper mesh showed extensive damage areas and a marked reduction in residual strength. While the outer layer of paint slightly increases the damage depth, it also reduces the surface damage extent. Samples identified as "good" repairs exhibited structural and electrical characteristics similar to those of a protected pristine sample. In contrast, for the "poor" repair samples, the location of the lightning strike attachment was crucial in measuring the damage area and evaluating residual strength. The author concludes by emphasizing the significance of scarf repair in restoring structural integrity and electrical conductivity.

1.4.2 Experimental Work

Some older literary works include Reid in 1991 [91], which established a linear correlation between damage and the action integral, and has since been validated by several other research projects. Additionally, other essential references that analyze damage, lightning strike mechanisms, and the experimental characterization of lightning strike protection methods have been briefly discussed.

Hirano et al. [92] studied the damage mechanisms of graphite/epoxy laminated composites and established a relationship between lightning strike waveforms and damage characteristics. The authors categorize the damage into three modes: fiber damage, resin deterioration, and delamination. The propagation of damage in the in-plane direction is highly dependent on the electrical properties of the graphite/epoxy laminate. Variations in specimen size and thickness did not significantly affect the damage response under the conditions of this study. Similarly, Harrell et al. [93] investigated the damage to CFRP laminates using three different waveforms. The specimen represented the typical materials used in the fabrication of wind turbine blades. The samples were evaluated using residual strength tests and visual inspection while also considering the temperature evolution of the lightning event. A strong correlation was observed between the sample temperature and the severity of lightning strikes. This correlation is particularly evident in samples subjected to concurrent impulse and DC, which experienced significant damage leading to reductions in compressive and shear strength of over 70% and 40%, respectively. On similar lines, Dong et. al. [94] evaluated the damage on CFRP samples exposed to components C and D sequentially and developed a numerical model. The ultrasound C scan revealed diamond-shaped damage morphology, with damage from component D dominating along the fibers, corresponding to a resistive heating mechanism. Additional damage associated with component C exhibited typical lightning arc heat flux characteristics. The author concluded that component D dominated in-plane damage, and with the sequential addition of component C, both the damage area and depth increased.

Tian et. al. [95],[96] in their papers aim to analyse lightning strike damage on CFRP composites with a fastener by both experimental and numerical methods, while also investigating the factors

that influence the damage modes. The damage morphology and sparking joint behaviour depend on the location of the initial attachment point. The damaged area spreads around the fastener and will likely lead to delamination, sparking, and outgassing when it directly strikes the fastener due to concentrated current flow. When lightning strikes away from the fastener, the damaged area is located around the lightning attachment area, and delamination does not occur as easily. The authors developed a conductive network and ran a coupled thermal-electrical simulation to understand the conductive path in both cases. Another independent study on CFRP with mechanical fastener by Kuang et. al. [97] arrived at similar conclusions. The author initially studied the effects of a single-lap composite joint and CFRP laminate with a metallic rivet, both experimentally and numerically. This was followed by investigating how the number of rivets and their spacing affected damage characteristics. Delamination emerged as the primary mode of failure, resulting from the pyrolysis of the matrix. The presence of nine rivets resulted in a smaller damage area than just one rivet, as the increased quantity effectively suppressed delamination induced by gas explosions. On the same lines, Heidlebaugh et. al. [98] independently studied the effects of lightning strikes on notched samples and samples with fasteners, which were assessed using destructive and non-destructive testing. The damage to the filled hole coupons was proportional to the magnitude of the current applied, and the surrounding damaged area was localized to the fastener. Residual testing indicated that filled hole specimens are stronger than large-notched specimens. Zhou et. al. [99] experimentally investigated the direct effects of simulated lightning strikes on carbon/epoxy and E-glass/epoxy laminates. Carbon/epoxy primarily exhibited resin sublimation at low currents, with increased fiber tufting at higher currents. In contrast, glass/epoxy laminates were affected mainly by delamination due to shock waves,

showing little to no evidence of joule heating. In this experiment, penetration was confined to the first two plies.

Coming to papers experimentally analyzing LSPs, Wang et al. [100] used four different CFRP laminates – no protection, full aluminum coating, local aluminum coating, and aluminum coating on glass cloth on the fastener head to understand the characteristics of ablation damage. This was achieved by conducting experimental studies and using the data to develop a 3-D finite element model. The numerical model accurately predicts failure when compared to experimental results. Damage assessments revealed that current flowed along the top ply of the specimen in the direction of the fibers, with an increase in damage area and thickness as peak current increases. Unlike local coatings, an aluminum spray applied across the specimen's entire width protects the sample from lightning strikes. Plated glass cloth effectively prevents current from conducting through the fastener. Moreover, Zhang et al. [101] introduced a lightweight interlaminar made from polyether ketone combined with carbon nanotubes as a lightning strike protection film. Laminates with this film and silver coating were tested alongside the development of a numerical method. Tests conducted under waveform D indicated that the novel method achieved a 34% and 44% reduction in damage area and weight compared to the silver-coated sample. However, only the first two layers of the silver-coated sample sustained damage, while the upper five plies were affected in the novel one. A coupled thermal-electric finite element model was also developed and validated against the experimental results. The numerical model facilitated modifications to the system by altering the ply layup and optimizing weight.

Hirano et al. [102] developed a carbon fiber-reinforced polymer with a special polyaniline (PANI)-based conductive thermosetting resin to enhance lightning damage suppression in the resulting material, and compared it to a carbon fiber/epoxy composite. The specimens were subjected to 40 kA and 100 kA simulated lightning currents of modified Waveform A. The CF/epoxy laminate exhibited significant damage at both waveforms, while the PANI laminate showed barely visible resin deterioration around the center. Observations through ultrasonic inspection indicated that the PANI specimen did not experience any defects in thickness and retained 90% of its strength after a residual strength test. An assessment of the thermal properties of both specimens yielded similar results, validating the enhancement in electrical properties due to the PANI matrix, thereby improving resistance to lightning damage. A related investigation by Guo et al. [103]studied the effectiveness of copper or aluminum expanded foils as a lightning strike protection layer when exposed to Waveform D. Samples subjected to visual inspection and ultrasonic scans post-strike showed a smooth and intact surface, thereby mitigating CFRP damage. Although the metallic grid had melted and vaporized, the underlying plies remained intact, thus effectively working against lightning strikes. Furthermore, through experimental and numerical simulations, it was observed that the electrical conductivity of the sample is anisotropic. Taking this property into account, the author established foil designs for Zones 1, 2, and 3. In a subsequent paper, the same authors also investigated the effect of fiberglass as an isolation layer for the lightning strike protection of CFRPs [104]. This layer was introduced between the CFRP substrate and aluminum or copper expanded foils, which then experienced lightning strikes of waveform C and D. The fiberglass layer, employing an isolating mechanism, was adequate to prevent lightning from penetrating downward to the underlying CFRP, thereby eliminating material ablation and joule heating. On the same lines Xu et. al. [105] discuss developing a thin, highly conductive nylon filter/nickel

(NFNi) film using a chemical deposition method, which is then applied to CFRP through hot pressing. This film was specifically designed for lightning strike protection and electromagnetic shielding. Lightning strike tests of waveform D were conducted on CFRP samples with the NFNi film and compared against LSP solutions, such as commercially available bucky paper, copper mesh, and unprotected samples. C-Scans and B-Scans indicated that the NFNi film reduced the damage area and depth by 20.29% and 37.5%, respectively. Compression after impact tests revealed that the NFNi sample maintained a residual strength of 95.8%, comparable to the sample protected by copper mesh. Since the areal density of NFNi is 11.3% lighter than copper mesh, it offers a weight-saving solution.

Another potential LSP, as discussed by Kumar et al. [106], is graphene thin film (GTF) paper. Their study showed three conceptual LSP designs: direct incorporation of CFRP, 3-D stitching, and four stitch configurations. GTF papers enhance the thermal and electrical conductivity of the material, preventing delamination based on stitching configuration and slightly reducing tensile strength. Rajesh et. al. [107] developed hybrid and metallic coatings, followed by a lightning impulse strike to evaluate damage. The hybrid coating contains silver nanoparticles dispersed in a conducting polymer and silver-coated carbon nanofibers on an epoxy surfacing film. The metallic coating consists of a continuous layer of silver with 10% copper in tin. The latter performed better than the former, based on the damage area observed from ultrasonic C-scans. However, when this coating is compared to expanded copper foil, the traditional method outperformed it, thus leaving the door open for future studies and experiments.

1.4.3 Numerical Work

Selected research projects focused on developing numerical methods to analyze the CFRP lightning strike mechanism, as well as designing optimized lightning strike protection systems, have been discussed. Millen and Murphy [108] present an assessment of various simulation strategies for evaluating lightning strike damage in CFRPs in their review paper. The models can be classified into three main types – thermal-electric, mechanical, and thermal expansion, with significant variability in material data, meshing, and boundary conditions. This paper particularly highlights the necessity for standardization and the introduction of additional parameters that should be considered to develop accurate models.

To begin with, Ogasawara et. al [109] conducted a coupled thermal-electrical analysis of CFRPs subjected to lightning strikes. They first calculated the electrical potential of a system under electrical boundary conditions and a concentrated electric current. Following this, they applied transient heat transfer analysis and described the temperature dependency of electrical conductivity. The results, particularly the delamination area, damage depth, and thermal decomposition behavior, aligned well with experimental findings. Joule heat significantly impacted lightning strike damage, especially regarding delamination and fiber breakage. Likewise, Duongthipthewa et. al [110], using an electrical-thermal-structural model, the analysis focused on the electrical, thermal, and stress distribution of LSP systems, specifically copper mesh (CM) and graphene-fuzzy fiber (GF). The author also examined the impact of lightning parameters and damage distribution. Simulation results indicated that the GF layer is highly effective in reducing thermal damage and stress levels while remaining lightweight. The thermal damage and stress response depended on waveform duration and peak current. Along with this, Dong et al. [111]

established a degradation model of the stiffness matrix with thermal-mechanical coupling under the umbrella of continuum damage mechanics to simulate lightning-induced damage. Using the experimental model in [92] to validate results, it was observed that the coupled model was much more consistent with experimental outcomes, even more so than a thermal ablation model. On the same lines, Yao et. al [112] set up a numerical method similar to those used by Dong et al. [111] to characterize lightning strike coupling damage. The authors used Feraboli and Miller [86] to correlate testing and numerical data, which was achieved with a 5 % error.

Yang et. al. [113] proposed a sequential thermal-electrical-mechanical finite element coupling model to analyze the damage to woven carbon-fiber reinforced polymer laminates (W-CFRPs) and woven composite honeycomb sandwich panels (W-CHSPs). This model captures the transient temperature variation due to the anisotropic conductivity of the laminate, which is then transferred to a mechanical model. The author employs a thermo-mechanical coupling damage constitutive model to simulate matrix failure and fiber damage. The results of the model closely matched the experimental findings, and the model successfully predicted delamination failure, which had not been achieved until then, thereby providing a more comprehensive approach to simulation. A progressive damage method developed by Millen et. al. [114] accounts for strain and heating rate effects, and a customized failure model incorporating Hashin / Puck failure criteria. The approach employs a three-stage simulation, where the first stage is an initial plasma model that predicts electrical, thermal, and pressure loads on the surface. This is followed by a coupled thermal-electrical model predicting surface temperature, and finally, a coupled temperature-displacement explicit model that predicts the mechanical response of the material state. The application of

Waveform A and B concluded that the former dominates multi-mode damage, while the latter primarily causes delamination.

Lee et al. [115] introduced an alternative approach for developing a machine learning model using regression algorithms to serve as a first-pass estimator of lightning strike damage, thereby reducing time-consuming and costly laboratory tests. The author employed supervised machine learning models, specifically linear regression, decision tree, and multilayer perceptron. The absence of a standardized methodology to assess damage and limited and inconsistent datasets in the literature restricts the development of such models.

1.4.4 Summary and Unresolved Challenges

To summarize the sources listed above, everything revolves around a sample that is being tested. This sample could be a novel material under investigation, such as a conductive material, materials with a lightning strike protection system like Copper Mesh, Carbon Nanotubes, or Bucky paper; various configurations, such as notched, unnotched, and filled holes; or a repair technique. Following this is the evaluation of the sample or specimen, which can be performed experimentally using simulated lightning strike waveforms, numerical and computational models, or a combination of both. Evaluation after experiments includes visual inspection, sectional observation, scanning technologies such as ultrasound, X-ray, or microscopy, residual strength testing, whether tensile or compressive, thermography, and DIC, to name a few. Apart from some suggestions mentioned in Wang et. al. [116], it should be noted that research conducted in recent years does not account for a sample that is under stress and subjected to a lightning strike. A few efforts have been made in the past to evaluate the damage characteristics due to lightning on loaded

samples. A summary of the currently available lightning strike simulators can be found in Leichaur [117].

Howell [118] in 1983 conducted lightning strike tests on unidirectional and quasi-isotropic laminates at various current levels. The specimens in this study were conditioned for moisture, and some were strained to 4000 μ-cm/cm before being subjected to current. Residual strength and damage were reported as results. This paper is possibly the first instance of applying a lightning current to a tensile-loaded sample. The specimens consisted of graphite/epoxy (Gr/E) composite material and were 30 cm long. Results indicated that the residual strength was significantly affected by the pre-loaded samples subjected to the current, showing a strength degradation of 6% at an action integral of 0.25 kA^2s and a degradation of 31% at an action integral of 1.7 kA^2s. The author mentioned that the presence of strain increases the susceptibility of Gr/E composites to damage under simulated lightning. The following paper, showing a similar study, was by Reid [119], [120] in 1989 and 1993. The author explicitly states that this research aims to understand the effect of loading the sample under compressive loads of up to 4500 με at various lightning currents and to assess the residual compressive strength. The paper states that "the effects of the test specimen being mechanically loaded at the time of current flow" have received little attention. Compressive loads have also been given consideration, as the compressive performance of a carbon fiber composite limits its design. The stress values considered were 200, 100, and 20 MPa, as well as no stress corresponding to the strain values. A test rig was developed to hold the specimen, alongside a hydraulic jack and an air spring to apply a load. The author concluded that a sample with a large cross-sectional area will be needed to assess the damage under high action integral and loading conditions. The author suggested adding a safety factor of 3 for the action

integral and 2 for the area of material to account for damage on loaded samples. An important point to note is that there have not been any recent papers primarily focusing on lightning strike analysis of a loaded sample. These papers are also limited in scope, as the dimensions of the sample, particularly the width, are not long enough to capture the detailed damage characteristics. Additionally, due to the lack of modern and accessible optical techniques available at the time, the understanding of damage morphology is limited.

1.5 Knowledge Gap and Motivation

This project aims to design and construct a one-of-a-kind artificial lightning strike simulator that also replicates in-flight mechanical stresses, specifically compression, to assess composite materials used in the aerospace industry. This will provide more realistic data on material performance, ultimately leading to safer, more economical, and fuel-efficient operations. Existing testing standards and prior research highlight a gap, particularly in characterizing loaded and unloaded samples during lightning strikes. Investigating this gap is essential to ensure that current protection methods adequately safeguard the aircraft.

Lightning strikes possess the potential to inflict significant damage to aircraft. The increasing use of composite materials, especially carbon fiber-reinforced polymers, which are mainly favored for their weight-saving benefits, is being curtailed due to the addition of lightning strike protection systems that adhere to strict regulations and certification standards. This extra structural weight undermines the weight-saving advantages of composite materials, thereby limiting the potential for increased payload capacity, reduced emissions, and lower fuel costs, ultimately impacting profitability.

Material data obtained through this system will be essential for further optimizing the design of lightning strike protection systems and evaluating the damage morphology of loaded versus unloaded samples with different configurations. A significant difference in damage characteristics or a considerable reduction in strength may require an immediate review of current testing and certification standards, thus prompting an urgent need to update existing regulations.

Chapter 2: Experiment Design and Setup

2.1 Load Application System

The primary requirement for developing the lightning strike simulator was selecting a load application system. Several options were analyzed qualitatively and quantitatively, then down-selected based on engineering complexity, time constraints, cost, manufacturability, and integration. One of the most critical design criteria was to reach 20% of the yield strength value of the sample being tested.

2.1.1 Simple Pulley System

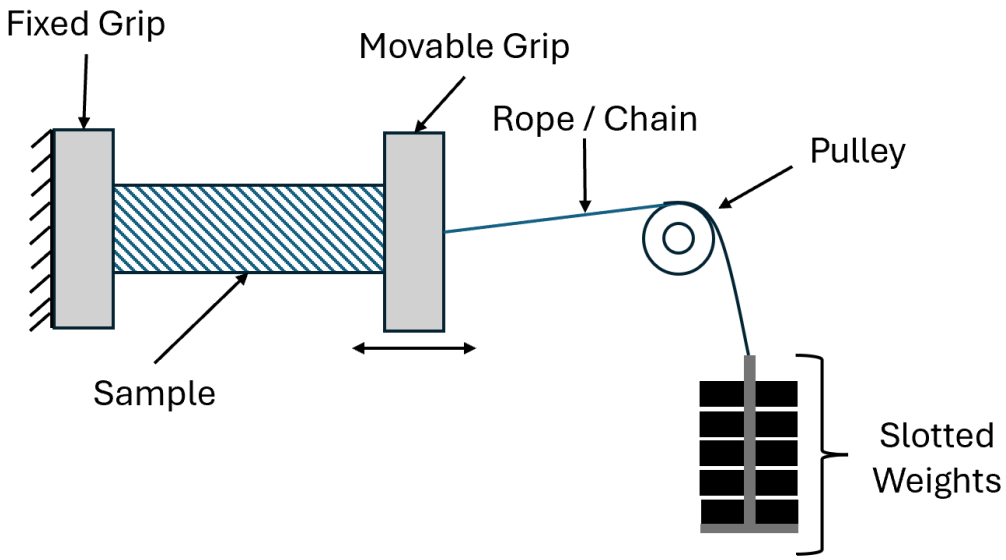

Figure 2.1. Simple Pulley System Schematic

A simple system was initially designed to reduce complexity and ease implementation. The sample is placed between two grips—one fixed and one movable. The fixed end secures the sample in

place, while the other grip is connected either through a rope or a chain that runs horizontally through a pulley, followed by a hanging weight system.

The addition of slotted weights results in a controlled tensile load being applied to the sample by gravity. Grips will be perforated along with tabs on the sample to enhance friction between the appropriate surfaces. This system offers a straightforward and efficient method for applying uniaxial tension to a material. The use of basic components makes it affordable and easy to assemble, eliminating the need for complex electronics and control systems, in turn requiring minimal maintenance. The applied load can be precisely adjusted by adding or removing the slotted weights. This, however, adds a manual component for altering the loads. An alternative method will also be necessary to determine the stress and strain parameters, given the absence of a measuring system. The loading rate is also fixed, meaning it is dependent on weight increments, which is not ideal for controlled strain rate testing. The most significant drawback is the lack of scalability, particularly with high-strength materials like composites, due to the mechanical limitations imposed by weight and rope. To illustrate this, assume an ultimate strength of 1500 MPa for a CFRP sample measuring 100 mm x 2 mm. A case involving 20% of ultimate strength would require an equivalent of 300,000 N or about 30,581 Kg, which is simply unfeasible to implement.

Iterating on this design, a traditional bench-wise system was developed to address the impracticality of applying large loads. This version maintains the cost-effective and straightforward approach of the previous design while enabling the application of both tension and compression loads in the sample. The overall design features a sample installed in the grips of a

bench-like frame. A manual lever will be utilized to apply tensile or compressive force through controlled rotations. Extensometers and a Digital Image Correlation (DIC) system will be used to address the existing data collection gaps. A conventional load frame will calibrate this system by establishing a relationship between displacement and material stress. The associated strain values will be corroborated with values obtained from the DIC and extensometer, along with the number of rotations. The resulting system can control mechanical loading with real-time strain monitoring, enabling stress estimation through pre-established calibration. Although this iteration addresses some drawbacks of the previous design, it still has a limited load capacity, which may not be sufficient to test materials such as CFRP. Additionally, it introduces a component of prior calibration that is highly dependent on sample quality and testing standards. While adding DIC and extensometers provides the required data, it also increases the time needed for setup and post-processing, which may reduce the repeatability of tests.

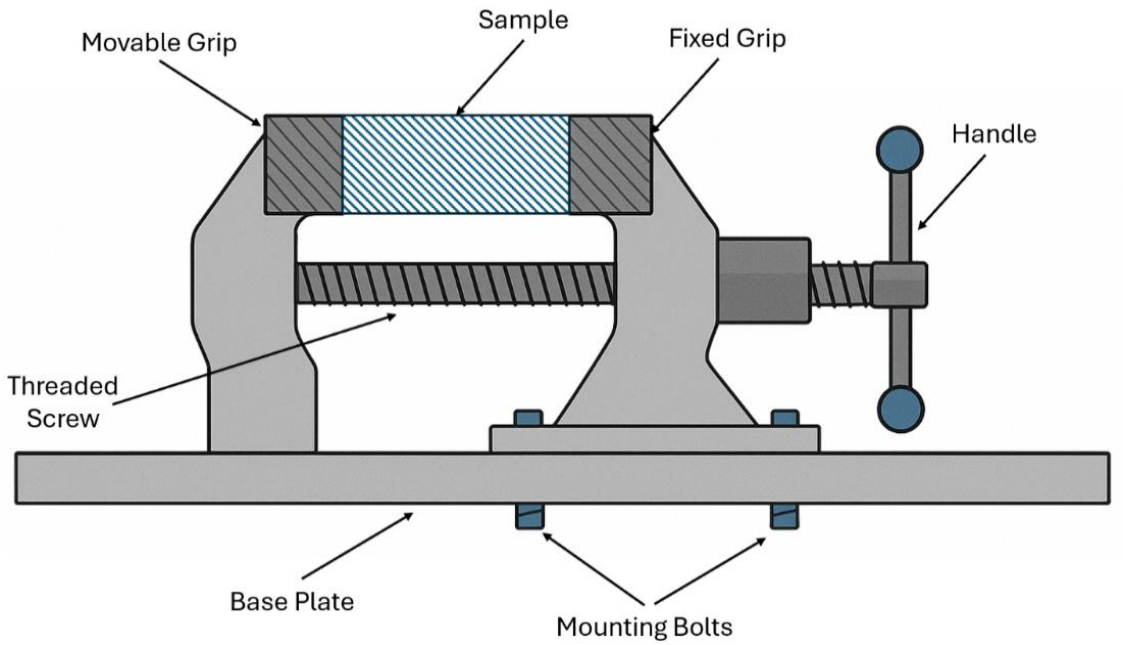

Figure 2.2. Bench vise-like system Schematic

2.1.2 Motorized Test Setup / Custom Universal Testing Machine

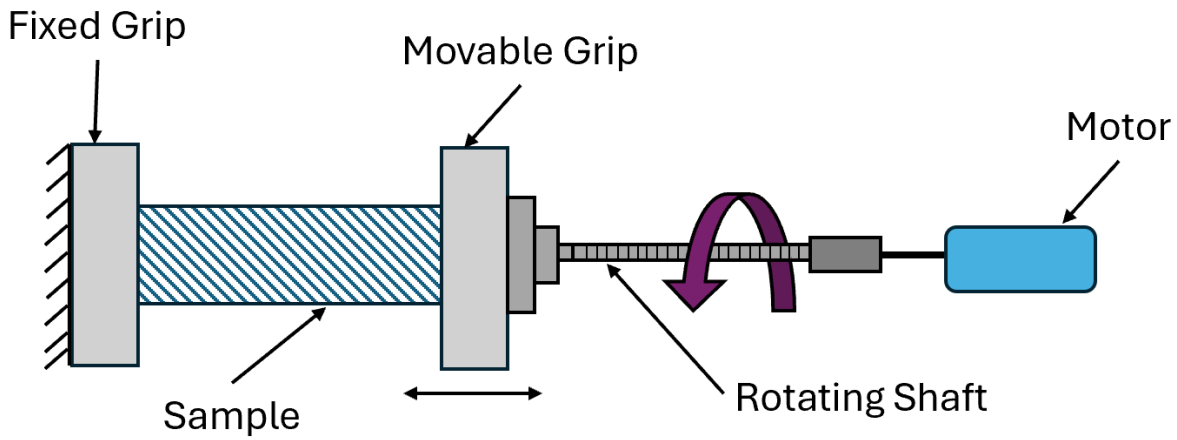

Figure 2.3. Motorized Test Setup (Direct Drive)

A motorized test setup was developed to enable precision and control in mechanical loading without manual actuation, thereby improving upon previous designs. Like the initial iteration, the test specimen is mounted horizontally between two grips—one fixed and the other attached to a threaded shaft. The movable grip can translate along the shaft's axis as it rotates. The system is powered by a motor that can be attached directly or via a coupler, allowing for smooth and continuous rotation. As the shaft rotates, the movable grip translates linearly either towards or away from the sample, depending on the direction of rotation, thus enabling the application of tensile or compressive loads. The inclusion of the motor eliminates the need for a manual lever or weights, facilitating the application of load in an automated, controlled, and repeatable manner. It can also be easily integrated with extensometers or displacement sensors for accurate strain measurement. This system will lead to the development of a complex setup that will require

additional resources for its advancement. A control system would be necessary, thus adding electronics and coding that would demand more time to implement.

The description above essentially refers to a custom-designed universal testing machine. Further research led to the discovery of a fully open-sourced machine developed by Stefan Hermann [121], which is described here. The engineer developed a cost-effective alternative to commercial systems, capable of performing both tensile and compressive tests. This system is specifically designed to evaluate the mechanical properties of 3D-printed parts. However, it serves as a good starting point for further exploration of the idea of designing a UTM for this project. The machine is constructed from machined wood elements, 3D printed parts, screws, and linear rails. It features an integrated load cell to measure force and an optical extensometer. The system is driven by a stepper motor that can apply controlled loading to a sample with interchangeable grips, making it suitable for various sample geometries. When comparing this system to previous proposals, it offers the ability to measure force, automated operation, programmability, versatility in application, and customization options. However, the increased complexity and build time required for developing this machine may not fit within the project timeline.

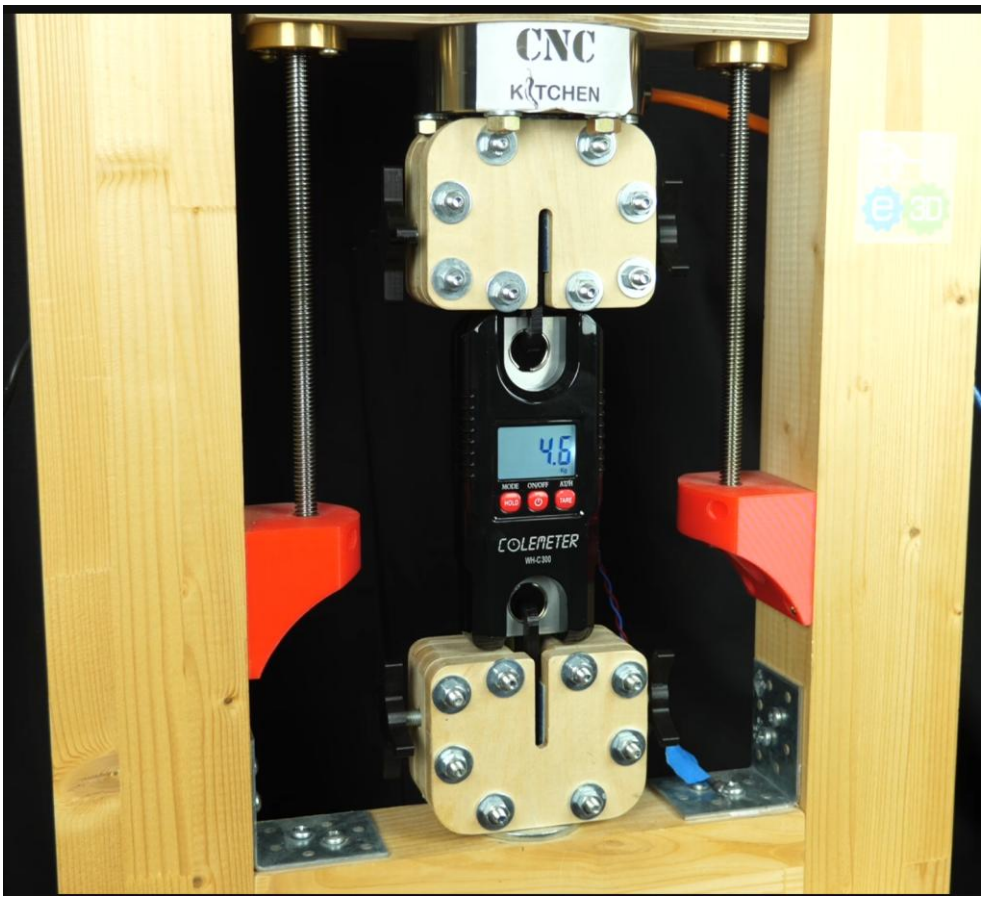

Figure 2.4. Open Source UTM by CNC Kitchen [121]

2.1.3 Commercial System

Although the design discussed in the previous section addressed several issues with manually or motor-operated systems, the complexity of development led to the exploration of commercially available systems. A horizontal universal testing machine was considered based on previous literature, particularly the orientation of the sample in relation to the lightning strike probe. A UTM can provide accurate and reliable data with versatile testing capabilities. These machines also comply with standards such as ASTM and are robustly built with industrial-grade components that can handle large loads, far exceeding the capacity of custom or in-house design options, making them an excellent choice for testing composite materials. However, these machines are quite

expensive, especially when purchased for just a single primary application. Additionally, strict construction limits the degree of customization, which may be necessary during the project.

All the proposed systems have been summarized in Table 2-1 below:

Table 2-1: Summary of Proposed Solutions

Feature	**UTM**	**Motorized Test Setup**	**Pulley / Bench – Vise System**
Force Measurement	Built-in precision load cell	Load cell or indirect by external calibration	Indirect Calibration
Loading Modes	Tension, Compression, Flexural, Shear	Tension or Compression	Tension or Compression
Accuracy & Repeatability	Very High	Moderate to High	Moderate (more error prone)
Testing Standard Compliance	ASTM, ISO Compliant	Non-Standardized	Non-Compliant
Data Logging	Automated, real-time	Requires the integration of additional systems	Requires the integration of additional systems
Cost	Very High	Low to Moderate	Very Low
Customizability	Low	High (open–source, customized parts)	High (user-defined geometry and actuation)
Ease of Use	Additional Training required	Medium (Requires hardware and software setup)	Easy to use
Development Time	Low	High	Moderate to High

2.1.4 Proposed Solution

Considering all the factors mentioned above and weighing the project's priorities, a commercially available hydraulic system was determined to be the ideal solution, given the project's constraints. It can apply large compressive forces to the sample, which is ideal, as composite material design is often limited by its compression performance. Additionally, this load case aligns with Boeing's current practice of assessing the compressive strength of filled-hole composite specimens, reinforcing its relevance and validity. It is robust and straightforward, making it a durable, low-maintenance solution that is also cost-effective compared to other commercially available systems. Hence, a Harbor Freight Hydraulic Shop Press with a maximum force capacity of 500kN or 50 tons was chosen. The upper limit of the force is discussed in the following section.

Figure 2.5. Harbor Freight Hydraulic Shop Press (Image Courtesy: [122])

2.2 Sample Size Analysis

Since no specific standard defines the dimensions of the sample that will undergo the lightning strike test, an extensive analysis was conducted sequentially. Based on the results obtained at the end of each stage, constraints were added and/or modified to be included in the analysis for the next stage.

The initial constraints were to design a sample with a dedicated zone in the center that is 4 inches in diameter to account for damage due to lightning, assuming a sample with an ultimate strength of 2000 MPa.

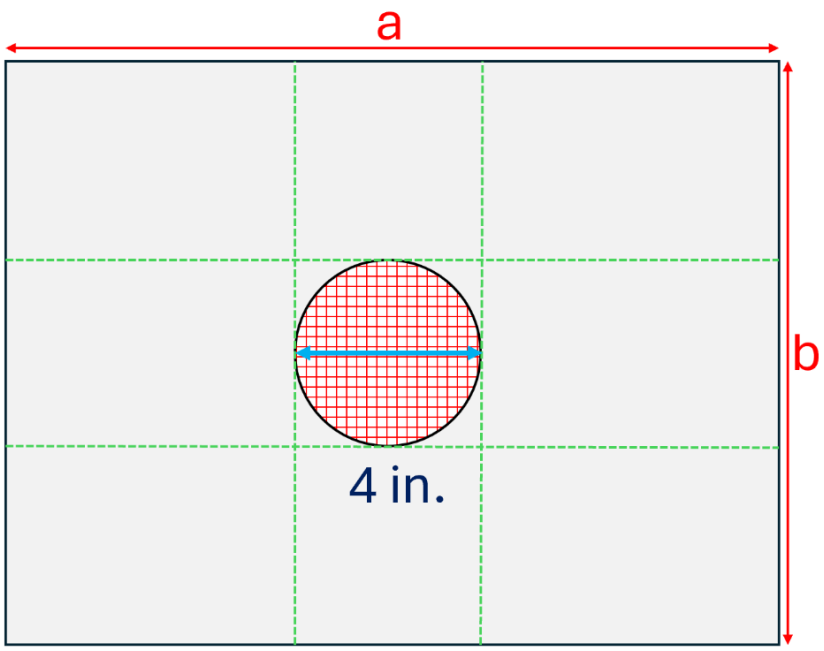

Figure 2.6. Initial Constraint

2.2.1 Initial Dimensional Analysis

To begin, it was decided to analyze the force distribution of samples with varying widths and thicknesses. The schematic by Johnson [123] shown in Figure 2.7 for a thin plate under compression was taken as a standard representation. Johnson also defined the equation for analysis.

$$F^{Cu} = \frac{P_f}{b.t} \qquad 2\text{-}1$$

Here, F^{Cu} is the compressive strength, P_f is the applied force, b is the width of the sample, and t is the sample thickness.

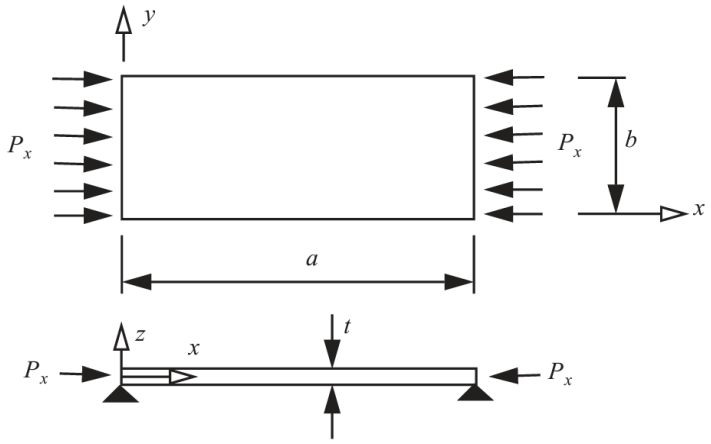

Figure 2.7. Schematic of a thin plate [123]

ASTM D7137 [124] is a standard test method that evaluates the residual compressive strength of fiber-reinforced polymer composites after impact. The standard provides published data on the cured ply thickness used in this analysis. ASTM D6641[125] is a standard test method for determining the compressive properties of polymer matrix composite materials using a combined loading compression fixture. The compressive strength properties in the data were taken as a

baseline for this analysis, along with 20% of the ultimate strength value defined above. The width of the sample ranged from 105 to 220 mm. The data points have been summarized in Table 2-2and Table 2-3. An area vs. force graph (Figure 2.8) was plotted to understand the distribution and the maximum force experienced. A maximum force of 200.98 kN was observed.

Table 2-2: Summary of Data Points

ASTM 7137 [124]	**ASTM 6641** [125]	
Thickness (mm)	Material ID	Compressive Strength (MPa)
0.085	A	701.89
0.1	B	734.98
0.13	C	778.42
0.15	D	618.11
0.18	E	686.99
0.25	F	913.56
0.36	G	336.46
0.5	H	387.83
1	J	408.65
	K	470.36

Table 2-3: Material ID Description [125]

MATERIAL ID	**Material**	**Lay Up**
A	Gr145 IM-Fiber/Epoxy Tape	$[45/90/-45/0]_{2s}$
B		$[45/90/-45/0]_{2s}$
C		$[45/90/-45/0]_{2s}$
D	Gr228 IM-Fiber/Epoxy Tape	$[-45/90/45/0]_{2s}$
E	SM-Fiber/Epoxy Tape	$[90/0]_{3s}$
F		$[0]_8$
G	E-Glass/Epoxy Fabric	$[90]_8$
H		$[0]_8$
J	E-Glass/Vinyl-Ester Fabric	$[90]_8$
K		$[0]_8$

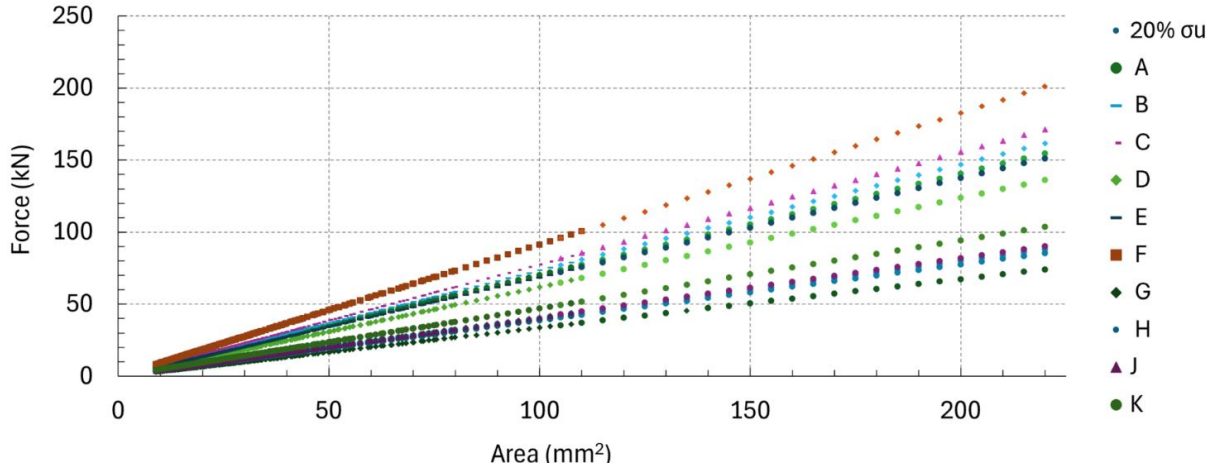

Figure 2.8. Force (kN) v/s Area (mm^2) Distribution (Preliminary Analysis)

However, having such thin samples may not be suitable for lightning strike analysis. Thus, a secondary analysis was necessary for a more representative thickness. The thickness of samples undergoing lightning strike tests was summarized in Xu et. al [126] and Millen and Murphy [108] were used and plotted against the same value of compressive strength in Table 2-2. A force v/s thickness plot (Figure 2.9) was used to understand the distribution of forces.

Table 2-4: Sample Dimensions in mm from [126] & [108]

Length (a)	Width (b)	Thickness (t)	Length (a)	Width (b)	Thickness (t)
150	100	4	450	450	3
304	304	4.404	450	450	1.5
150	100	4.704	450	450	2.096
500	250	3	304.8	38.1	2.88
500	250	2	150	100	4
150	100	4.4	102	152	4.6
500	500	2	500	250	3.6
150	100	3	150	100	2
200	200	2.47	150	100	5.2
150	150	2	150	100	3.6
150	150	4.4	300	300	3.2

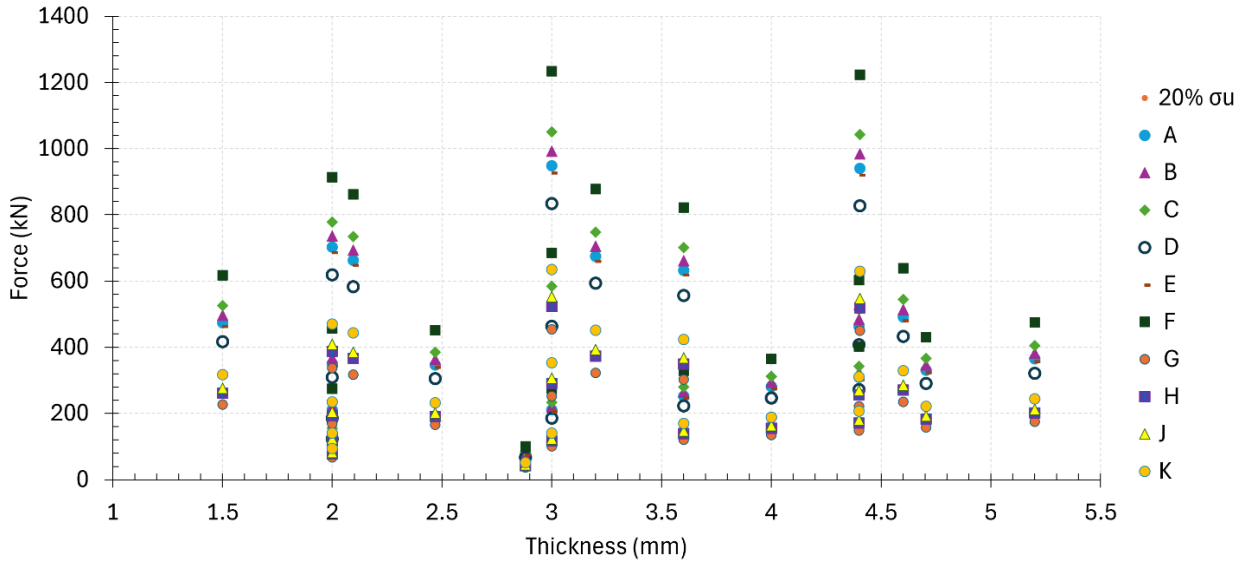

Figure 2.9. Force (kN) v/s Thickness (mm) Distribution (Secondary Analysis)

As observed, there was significant variation in the force, ranging from 80 kN to approximately 1400 kN, which required additional constraints to narrow the sample size. Of the 264 plotted points, 188 were below 500 kN, accounting for 71.21% of the data points. Given the considerable cost difference between a 500 kN hydraulic press and a larger capacity press, this was established as the upper limit for loading, thereby influencing the sample sizing process. Many samples were relatively thick (> 4 mm) and hence were not a good representation of the composites applied in practical aerospace applications. Consequently, a thickness of about 2 mm was targeted, with the goal of achieving an ultimate strength of 50% with the same sample.

Therefore, a sample thickness of 2 mm with a variable width served as the foundation for the tertiary analysis. The force versus area curve, along with the upper limit, has been plotted in Figure 2.10. As noted, most data points lie below the 500 kN upper limit. A heat map was also created to visualize the distribution of force values, placing greater emphasis on the 20% and 50% force

constraint values. Data points marked in red exceeded the load capacity of the hydraulic press and were discarded from consideration as seen in Figure 2.11.

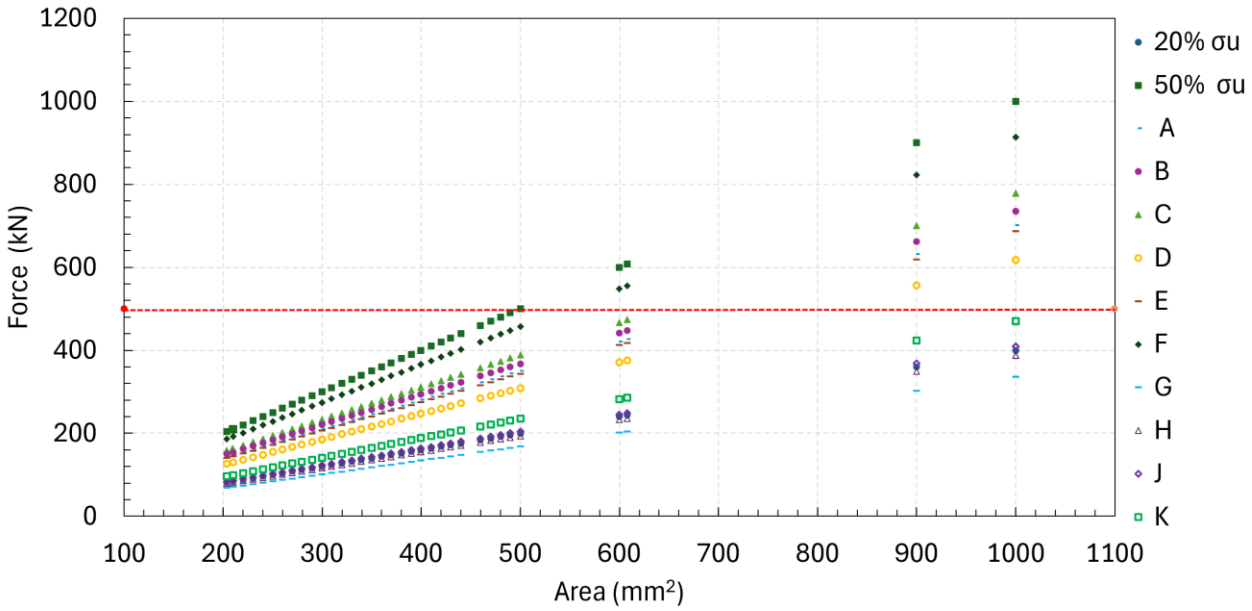

Figure 2.10. Force (kN) v/s Area (mm^2) Distribution (Tertiary Analysis)

								MPa						
			400	1000	701.89	734.98	778.42	618.11	686.99	913.56	336.46	387.83	408.65	470.36
			20% σ_u	50% σ_u	A	B	C	D	E	F	G	H	J	K
t (mm)	b (mm)	Area (mm^2)						Force (kN)						
2	105	210	84	210	147.40	154.35	163.47	129.80	144.27	191.85	70.66	81.44	85.82	98.78
2	110	220	88	220	154.41	161.70	171.25	135.99	151.14	200.98	74.02	85.32	89.90	103.48
2	115	230	92	230	161.43	169.05	179.04	142.17	158.01	210.12	77.39	89.20	93.99	108.18
2	120	240	96	240	168.45	176.40	186.82	148.35	164.88	219.25	80.75	93.08	98.08	112.89
2	125	250	100	250	175.47	183.75	194.60	154.53	171.75	228.39	84.12	96.96	102.16	117.59
2	130	260	104	260	182.49	191.10	202.39	160.71	178.62	237.52	87.48	100.84	106.25	122.29
2	135	270	108	270	189.51	198.44	210.17	166.89	185.49	246.66	90.85	104.71	110.34	127.00
2	140	280	112	280	196.53	205.79	217.96	173.07	192.36	255.80	94.21	108.59	114.42	131.70
2	145	290	116	290	203.55	213.14	225.74	179.25	199.23	264.93	97.57	112.47	118.51	136.40
2	150	300	120	300	210.57	220.49	233.53	185.43	206.10	274.07	100.94	116.35	122.60	141.11
2	155	310	124	310	217.58	227.84	241.31	191.62	212.97	283.20	104.30	120.23	126.68	145.81
2	160	320	128	320	224.60	235.19	249.09	197.80	219.84	292.34	107.67	124.11	130.77	150.52
2	165	330	132	330	231.62	242.54	256.88	203.98	226.71	301.47	111.03	127.98	134.86	155.22
2	170	340	136	340	238.64	249.89	264.66	210.16	233.58	310.61	114.40	131.86	138.94	159.92
2	175	350	140	350	245.66	257.24	272.45	216.34	240.45	319.74	117.76	135.74	143.03	164.63
2	180	360	144	360	252.68	264.59	280.23	222.52	247.32	328.88	121.13	139.62	147.11	169.33
2	185	370	148	370	259.70	271.94	288.01	228.70	254.19	338.02	124.49	143.50	151.20	174.03
2	190	380	152	380	266.72	279.29	295.80	234.88	261.06	347.15	127.86	147.38	155.29	178.74
2	195	390	156	390	273.74	286.64	303.58	241.06	267.93	356.29	131.22	151.25	159.37	183.44
2	200	400	160	400	280.75	293.99	311.37	247.25	274.80	365.42	134.59	155.13	163.46	188.14
2	205	410	164	410	287.77	301.34	319.15	253.43	281.67	374.56	137.95	159.01	167.55	192.85
2	210	420	168	420	294.79	308.69	326.94	259.61	288.54	383.69	141.31	162.89	171.63	197.55
2	215	430	172	430	301.81	316.04	334.72	265.79	295.41	392.83	144.68	166.77	175.72	202.25
2	220	440	176	440	308.83	323.39	342.50	271.97	302.28	401.96	148.04	170.65	179.81	206.96
2	230	460	184	460	322.87	338.09	358.07	284.33	316.02	420.24	154.77	178.40	187.98	216.37
2	235	470	188	470	329.89	345.44	365.86	290.51	322.89	429.37	158.14	182.28	192.07	221.07
2	240	480	192	480	336.91	352.79	373.64	296.70	329.76	438.51	161.50	186.16	196.15	225.77
2	245	490	196	490	343.92	360.14	381.42	302.88	336.63	447.64	164.87	190.04	200.24	230.48
2	250	500	200	500	350.94	367.49	389.21	309.06	343.50	456.78	168.23	193.92	204.33	235.18
2	304	608	243.2	608	426.75	446.87	473.28	375.81	417.69	555.44	204.57	235.80	248.46	285.98
2	500	1000	400	1000	701.89	734.98	778.42	618.11	686.99	913.56	336.46	387.83	408.65	470.36
2	500	1000	400	1000	701.89	734.98	778.42	618.11	686.99	913.56	336.46	387.83	408.65	470.36
2	450	900	360	900	631.70	661.48	700.58	556.30	618.29	822.20	302.82	349.05	367.79	423.32
2	102	204	81.6	204	143.18	149.94	158.80	126.10	140.15	186.37	68.64	79.12	83.37	95.95
2	300	600	240	600	421.13	440.99	467.05	370.87	412.20	548.13	201.88	232.70	245.19	282.22

Figure 2.11. Tertiary Analysis Heat Map

2.2.2 Damage Area Analysis

Following the force analysis, there were still many variables to consider. Therefore, the percentage of damaged area was deemed the next elimination criterion.

The damaged area of the samples in [86], [87], [89] has been shown in Table 2-5.

Table 2-5: Damage Area: Literature

Reference	Sample Dimensions (in.)	Damage Area (in^2)	Sample Area (in^2)	Max. Damage Area (in^2)	Damage Area (%)
[86]	12 x 1.5 x 0.112	2.43, 1.84, 1.02, 6.43, 2.85, 0.36, 0.05	18	6.43	35.722
[87]	12 x 1.5 x 0.180	0.6, 4,42, 4,62, 1.75, 5.94, 14.91	18	14.91	82.833
[89]	12 x 4 x 0.180	3.92, 2.865, 0.153, 0.277, 0.157, 0.219, 3.069, 5.572	48	5.573	11.610

A damage area equivalent to a circle with 4 in. diameter is equal to 12.57 in^2; hence, assuming a square specimen, the given damage area was calculated as a percentage of the sample area, and the results are in Table 2-6.

Table 2-6: Damage Area: Square Specimen

a x b (mm)	Sample Area (in^2)	Damage Area (%)	a x b (mm)	Sample Area (in^2)	Damage Area (%)
105 x 105	11025	73.56	175 x 175	30625	26.48
110 x 110	12100	67.02	180 x 180	32400	25.03
115 x 115	13225	61.32	185 x 185	34225	23.70
120 x 120	14400	56.32	190 x 190	36100	22.46
125 x 125	15625	51.90	195 x 195	38025	21.33
130 x 130	16900	47.99	200 x 200	40000	20.27
135 x 135	18225	44.50	205 x 205	42025	19.30
140 x 140	19600	41.38	210 x 210	44100	18.39
145 x 145	21025	38.57	215 x 215	46225	17.54
150 x 150	22500	36.04	220 x 220	48400	16.76
155 x 155	24025	33.76	230 x 230	52900	15.33
160 x 160	25600	31.68	235 x 235	55225	14.68
165 x 165	27225	29.79	240 x 240	57600	14.08
170 x 170	28900	28.06	245 x 245	60025	13.51

Cases in which the damage was exceptionally low or high were taken out of consideration since it would lead to complexity in the design of the fixture or may not be able to capture the full extent of damage. Quoting Feraboli and Miller [86] “The finite width of the specimen imposes limitations on the propagation of damage” and Xu et. al. [126] “use of long, thin specimens produced undesirable failure modes such as compressive failure away from the lightning damage zone due to buckling.” & “Feraboli and Miller used a specimen only 38.1 mm wide exposed to Waveform D with peak currents of 10, 30, and 50 kA. Therefore, the use of 250 mm × 220 mm quadrants should be sufficient to contain the damage of the current waveforms used in this study.” The specimens can be seen in Figure 2.12 and the limited width is unable to capture the full extent of the damage.

This led to the conclusion that choosing a sample with a larger surface area would be beneficial in understanding the complete extent of damage in the specimen. Thus, the updated heat map looks like Figure 2.13.

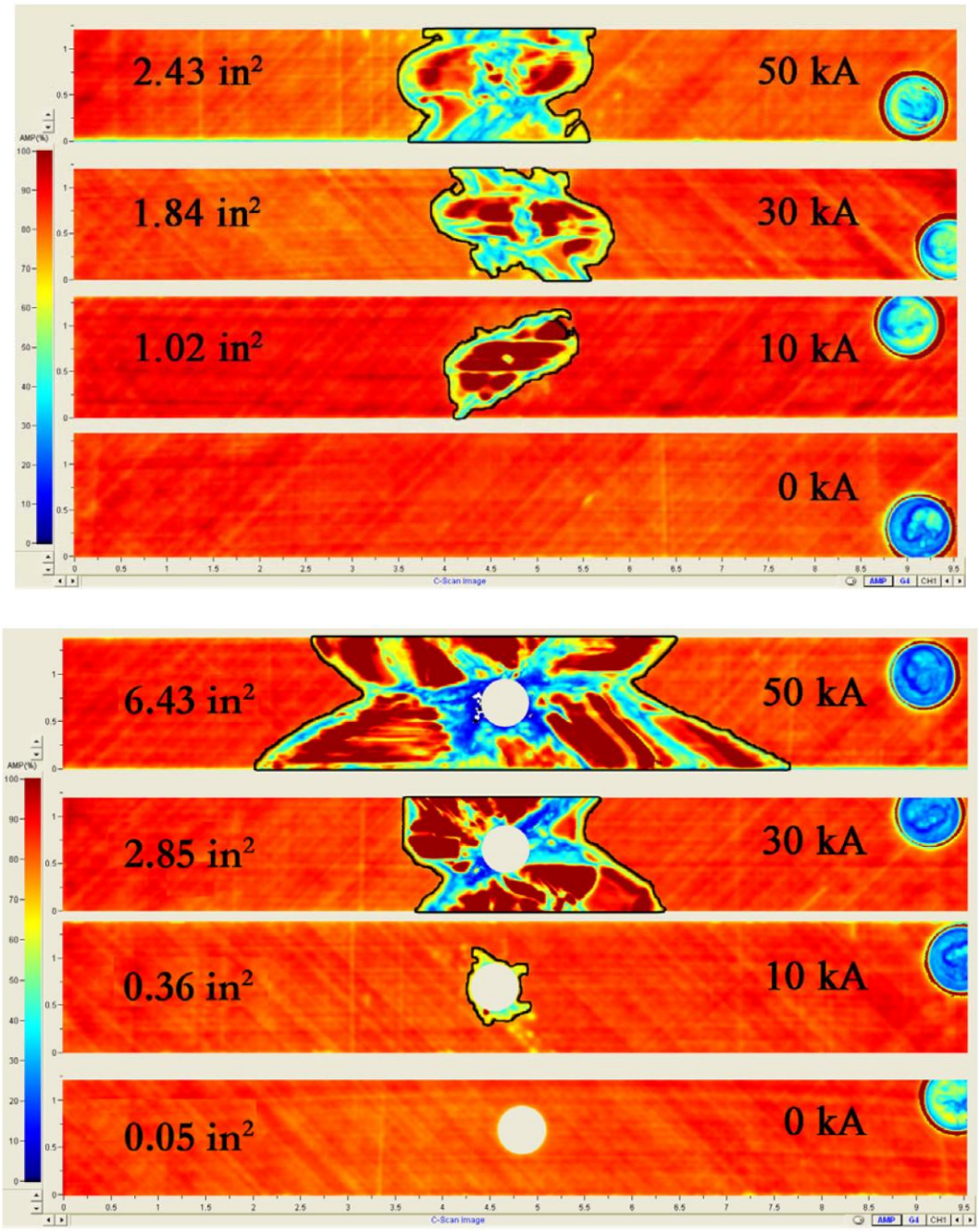

Figure 2.12. C Scan of Specimens in Feraboli and Miller [86]

					MPa									
			400	1000	701.89	734.98	778.42	618.11	686.99	913.56	336.46	387.83	408.65	470.36
			20% σ_u	50% σ_u	A	B	C	D	E	F	G	H	J	K
t (mm)	b (mm)	Area (mm^2)			Force (kN)									
2	150	300	120	300	210.57	220.49	233.53	185.43	206.10	274.07	100.94	116.35	122.60	141.11
2	155	310	124	310	217.58	227.84	241.31	191.62	212.97	283.20	104.30	120.23	126.68	145.81
2	160	320	128	320	224.60	235.19	249.09	197.80	219.84	292.34	107.67	124.11	130.77	150.52
2	165	330	132	330	231.62	242.54	256.88	203.98	226.71	301.47	111.03	127.98	134.86	155.22
2	170	340	136	340	238.64	249.89	264.66	210.16	233.58	310.61	114.40	131.86	138.94	159.92
2	175	350	140	350	245.66	257.24	272.45	216.34	240.45	319.74	117.76	135.74	143.03	164.63
2	180	360	144	360	252.68	264.59	280.23	222.52	247.32	328.88	121.13	139.62	147.11	169.33
2	185	370	148	370	259.70	271.94	288.01	228.70	254.19	338.02	124.49	143.50	151.20	174.03
2	190	380	152	380	266.72	279.29	295.80	234.88	261.06	347.15	127.86	147.38	155.29	178.74
2	195	390	156	390	273.74	286.64	303.58	241.06	267.93	356.29	131.22	151.25	159.37	183.44
2	200	400	160	400	280.75	293.99	311.37	247.25	274.80	365.42	134.59	155.13	163.46	188.14

Figure 2.13. Updated Heat Map

Considering the two extreme cases of a 15 cm x 15 cm and 20 cm x 20 cm cross-section, the latter was chosen particularly for the reasons outlined above: to have a specimen with a large enough cross-sectional area to understand the damage morphology.

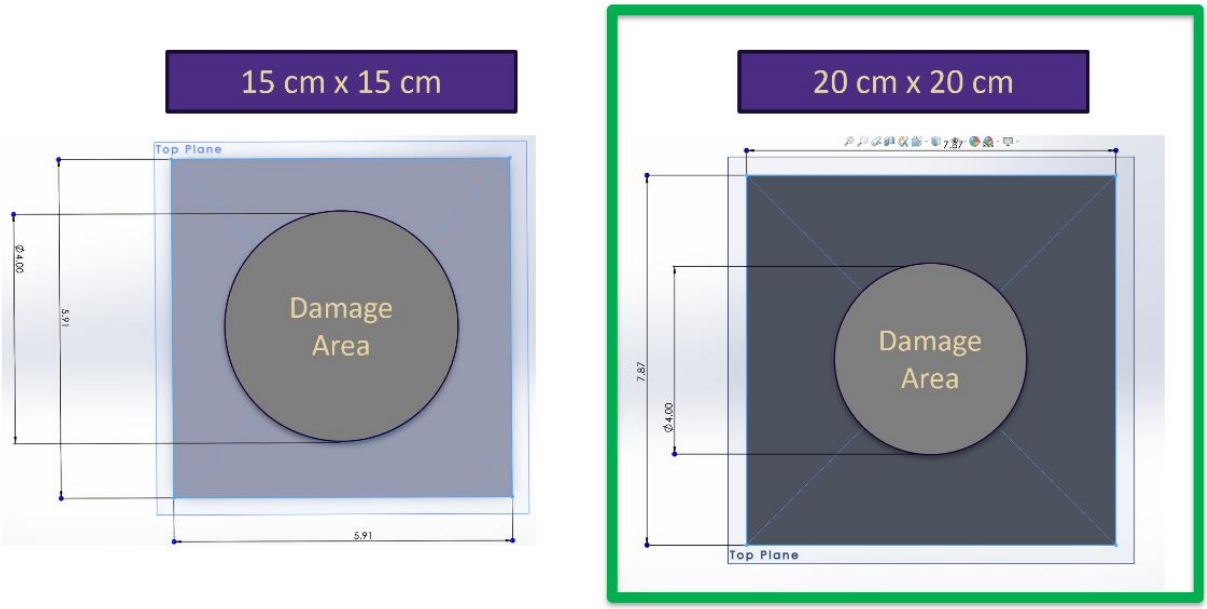

Figure 2.14. Specimen Dimensions with damage area (Actual Scale)

2.2.3 Buckling Analysis

A buckling analysis was conducted to ensure the specimen could reach the desired load without failure. An assumption was explicitly made regarding a specimen with a Quasi-isotropic layup; therefore, the following equations were initially used to calculate the critical load.

$$P_{xcr} = \frac{\pi^2 Db}{a^2};\ where\ D = \frac{Et^3}{12(1-\nu^2)} \qquad 2\text{-}2$$

With the given dimensions derived above, in addition to the value of elastic modulus mentioned in ASTM 6641 [125] the critical load was calculated with a Poisson's ratio of 0.29 and tabulated in Table 2-7.

Table 2-7: Buckling Analysis

E (MPa)	P_{cr} (kN)
150000	5.39
55020.2	1.98
55364.9	1.99
56192.3	2.02
59915.4	2.15
110798.7	3.98
27510.1	0.99
28751.1	1.03

At this stage, it was clear that the sample would not be able to meet the desired loading conditions. However, previous literature shows that using a robust fixture can help in reaching the desired loading condition. The following two examples can illustrate this.

1. Sanchez-Saez et. al. [127]

   The specimens measured 78 mm x 78 mm with thicknesses of 2.2 mm or 1.6 mm. Following impact tests conducted using a drop tower, the samples were placed into custom-designed compression fixtures after impact. Although the samples sustained damage, they were still able to reach high levels of force, as calculated and shown in Table 2-8.

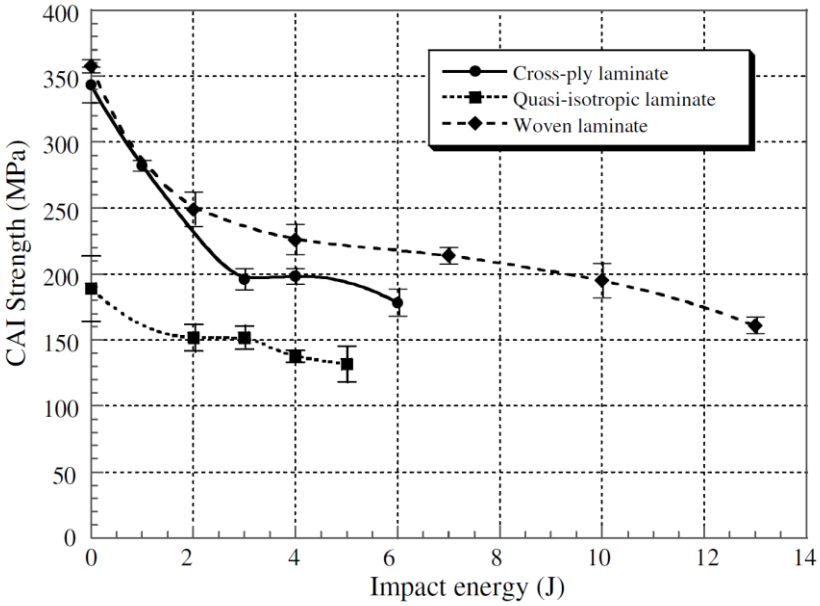

Figure 2.15. CAI Strength v/s Impact Energy [127]

Table 2-8: Failure Force for Laminates in [127]

	Cross-ply Laminate (t = 2.2 mm)	**Quasi-isotropic Laminate (t = 1.6 mm)**	**Woven Laminate (t = 2.2 mm)**
Force (kN)	58.34, 48.04, 34.32, 30.88	24.96, 18.72, 16.22	53.19, 42.9, 39.46, 36.9, 32.60, 28.31

2. Guo et. al. [128]

Figure 2.16 shows the compression after impact tests on samples measuring 150 mm x 100 mm and 4.48 mm thick. Like in the previous case, the samples can reach high enough force values.

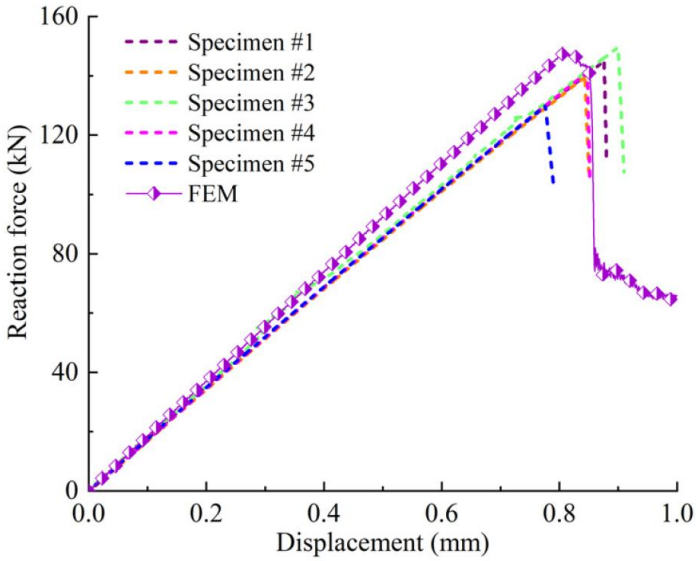

Figure 2.16. Reaction Forces and CAI Strength [128]

Thus, based on historical precedents, the fixture would have a robust design to prevent the sample from buckling. Additionally, a sensitivity analysis of the dimensional parameters was conducted to explore potential modifications. For this analysis, the process and equations laid out by Yang [129] were followed. The buckling analysis of clamped plates under uniaxial compressive load conditions is examined. The equation for the critical buckling load for this case is given below.

$$= \begin{cases} \dfrac{4\pi^2 D_{11} m^2}{a^2} + \dfrac{4\pi^2 D_{22} a^2}{b^4 m^2} + \dfrac{16\pi^2}{3b^2}\left(\dfrac{1}{2}D_{12} + D_{66}\right), m = n \\ \dfrac{D_{11}\dfrac{\pi^2}{a^2}(n^4 + 6n^2m^2 + m^4) + D_{22}\pi^2\dfrac{16}{3}\dfrac{a^2}{b^4} + \left(\dfrac{1}{2}D_{12} + D_{66}\right)\dfrac{16\pi^2}{3b^2}(n^2 + m^2)}{n^2 + m^2}, m \neq n \end{cases} \quad 2\text{-}3$$

Figure 2.17 illustrates a plot to critically analyze how variations in geometrical parameters affect the sensitivity of the buckling load. Thickness significantly impacts the critical load, as even a minor change can lead to a substantial variation in its value as compared to the other parameters.

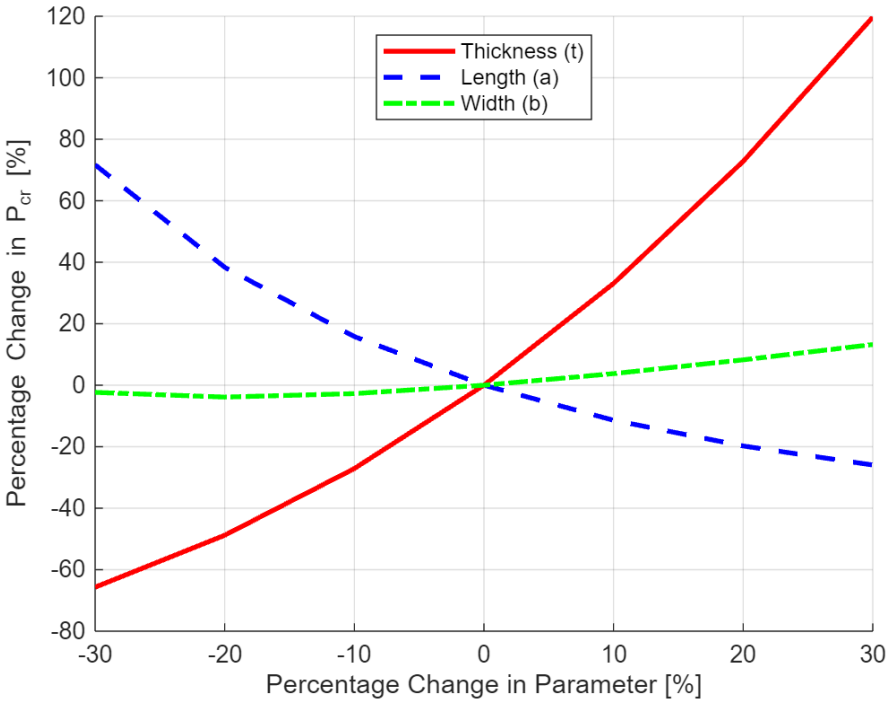

Figure 2.17. Specimen Dimensions Sensitivity Analysis

Considering the sensitivity analysis, the dimensions of the sample were modified to 15 cm x 20 cm with a thickness of 2.5 mm.

2.2.4 Layup Analysis

The number of layers and the layup schedule have a significant impact on the damage tolerance of composite materials. The layup sequence determines the path of electric currents and how they distribute through the material. In the case of a unidirectional layup, since current travels through the fibers, it may potentially lead to localized heating and damage along those fibers. Quasi-isotropic or cross-ply layups distribute the current more evenly, reducing the extent of damage [130]. The criteria were that the thickness should be as close as possible to 2.5 mm and that the plies should be within a range of 12 to 16.

To begin with, data from previous literature and ASTM standards were analyzed and compiled, specifically focusing on the layup schedule, ply thickness, number of piles, specimen thickness, and material used. Cases were further selected based on the defined criteria. The final options being considered are shown in Table 2-9.

Table 2-9: Sample Layup Options

S. No.	Lay Up	Ply Thickness (mm)	No. of Plies	Sample Thickness (mm)
1.	$[45/0/-45/90]_{2S}$	0.18	16	2.88
2.		0.15	16	2.40
3.	$[45/0/-45/90]_{3S}$	0.1	24	2.40
4.		0.125	24	3.00
5.	$[+45/0_2/-45/0_3/90]_s$	0.18	16	2.88

At the end, a layup schedule was chosen because it meets several criteria: the total number of plies falls within the specified range of 12 to 16, the resulting laminate thickness closely aligns with the previously targeted value, and the layup itself represents a standard quasi-isotropic configuration that has been extensively studied in earlier research.

2.2.5 Final Sample Characteristics

The final characteristics of the sample are summarized in Table 2-10.

Table 2-10: Sample Characteristics

Parameter	Value
Area of Interest	15 cm x 20 cm
Thickness	2.88 mm
No. of Plies	16
Layup	$[45/0/-45/90]_{2S}$
Ply Thickness	0.18 mm

2.3 **Fixture Design**

As discussed in Section 2.2.3 the design of the fixture is crucial as it is central to preventing the buckling of the sample. The fixture must secure and align the sample to avoid undesirable loading, such as bending, asymmetric, or eccentric loading. It should be capable of distributing the load appropriately so that the sample is always under compression. The design must be robust to enhance repeatability and reproducibility. The fixture should include restraints to limit lateral deflection, ensuring that the sample does not buckle. It will be sized according to the dimensions of the hydraulic press and the sample. Additionally, the fixture should have elements that insulate it from the current supply to prevent a current path through the press. The fixture was designed using an iterative approach, incorporating changes based on the feedback received.

2.3.1 Fixture Design Literature Review

A specific literature review was conducted to learn about previously designed fixtures for thin composite laminates. These papers provided a foundational understanding to initiate the initial design iterations.

1. Compression after Impact Fixture

   Initially, a Compression After Impact (CAI) fixture was considered primarily due to its extensive use and standardization, which makes it compatible across various research and industrial applications. This fixture must be scaled up to accommodate the larger sample size used in this study compared to the conventional CAI specimen. The design is intended to prevent global buckling, particularly for thin laminates. However, the specimen promotes local buckling in the damaged area, typically at the center. Key design features include support rails

along the edges of the specimen, which are beneficial for constraining the specimen laterally, and end supports that facilitate the application of in-plane compressive load. In addition, ASTM 7137 [124] provides a detailed drawing of the fixture and a procedure to aid in designing and using the custom-made fixture for this study. A snapshot of a simplified version of the fixture is shown in Figure 2.18. An illustration of the actual fixture is shown in Figure 2.20. Airbus, Boeing, and NASA have their custom CAI fixtures, which are more precise to ensure no deviations can invalidate the result, particularly in aerospace and defense applications.

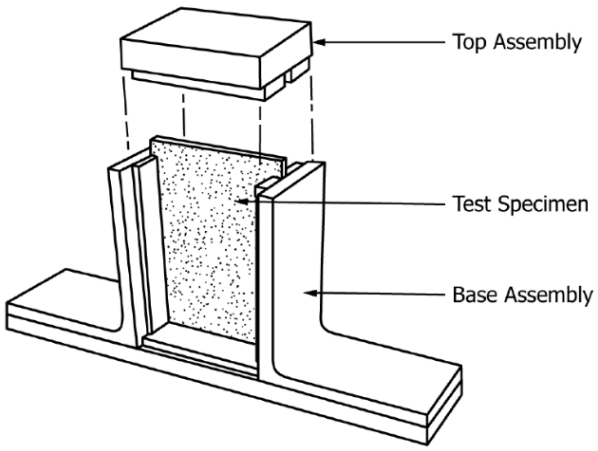

Figure 2.18. CAI Fixture ASTM 7137

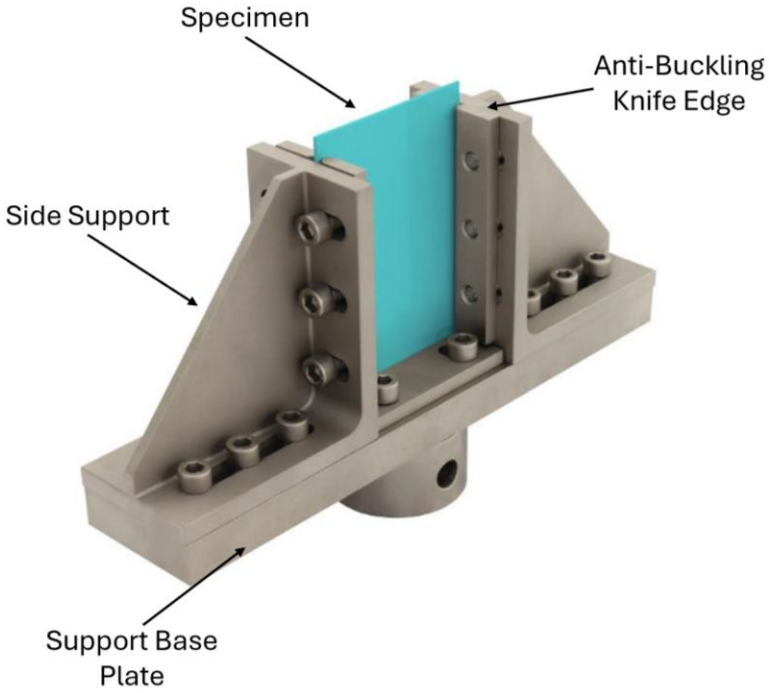

Figure 2.19. CAI Fixture ASTM 7137 (Modified; Image Courtesy: [131])

2. Modified CAI Fixture

Previous literature has utilized traditional CAI Fixtures with modifications. These have primarily been used to test samples subjected to a lightning strike or impact. (as described in Francesconi et al [132]). Xu et al. [126] conducted a systematic experimental study to modify standard CAI fixtures and specimen geometry, specifically for what the author defined as compression after lightning strength evaluation, aiming to induce specimen failure from the area of lightning damage to obtain more accurate values.

The modified CAI jigs shown in Figure 2.20 were primarily selected for their ability to accommodate samples with varying widths. Steel jaws were used to clamp the top and bottom edges of the specimen. Anti-buckling constraints were utilized to stabilize wider specimens.

These constraints were crucial in preventing out-of-plane deformation while ensuring the specimen remains aligned. G clamps secured the fixture to the test frame, enhancing the stability of the arrangement. These modifications were vital for minimizing the risk of global buckling, particularly when testing large specimens with lightning damage. The larger fixture incorporates a flattened steel rod on the top and bottom, providing consistent lateral support.

(a) 120 mm wide notched specimen *(b) 220 mm wide notched specimen*

Figure 2.20. Modified CAI Fixture (Xu et al. [126])

However, initial testing of a few samples revealed a significant problem, particularly during the CAI test; failure occurred at the location of an unsupported gap in the jig, rather than at the center of the specimen. Consequently, these results were deemed undesirable. The failure was attributed to compression, buckling, and the unsupported gap in the corner. The unsupported gap does not laterally constrain the specimen, allowing it to deform or buckle earlier. Furthermore, the constraint on the top and bottom edges is uneven, introducing additional load asymmetry. Modifications were implemented to eliminate this gap by using a wider sample than the traditional CAI specimen. This adjustment allows the steel jaws to move further down, ensuring that all edges for this test are constrained, as

evidenced in Figure 2.21. With that, the top edge is fully supported, which reduces the risk of premature buckling. This modification helped ensure that the failure occurred at the center of the specimen, indicating a successful test. These modifications were considered effective in minimizing out-of-plane bending and failure at the unsupported gap. Further details regarding these fixtures can be found in Xu et al. [133].

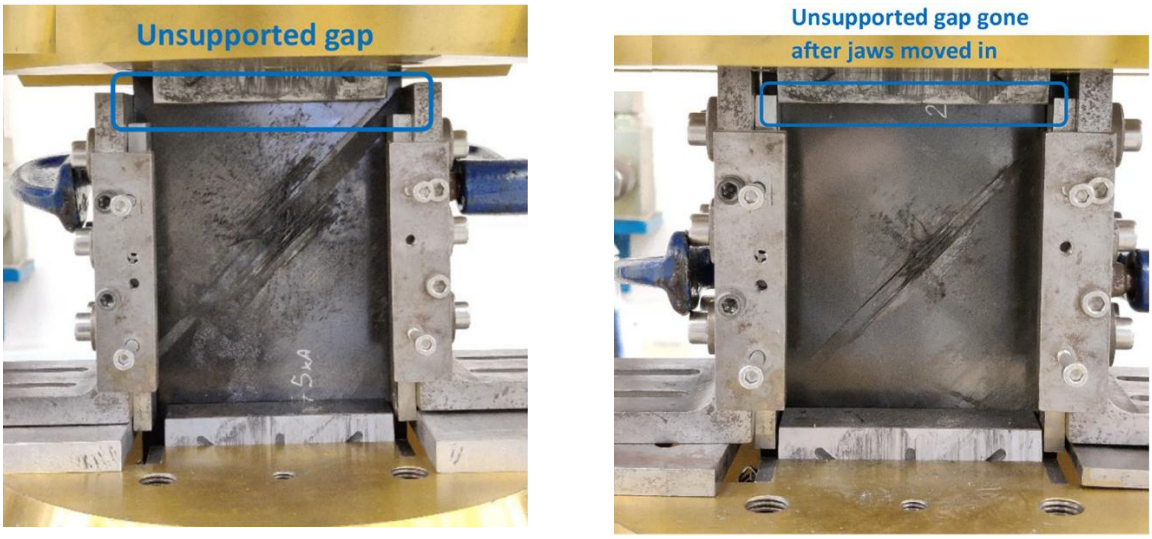

(a) Fixture highlighting unsupported gap *(b) Further modification to reduce the gap*

Figure 2.21. Modified CAI Fixture (Xu et al. [126])

3. Custom-Built Fixtures

Sanchez-Saez et al. [127] evaluated the damage tolerance of various thin carbon-epoxy laminates using a new testing device specifically designed for thin laminates. The thickness of the specimens tested by the authors ranged from 1.5 mm to 2.2 mm, so the fixture would need to accommodate this variability. The preliminary fixture designs are shown below in Figure 2.22. Set up 'A' features a fully supported fixture with anti-buckling elements on all edges, providing comprehensive lateral support. This demonstrates excellent buckling

restraint. However, like the edge loading failure in the previous case discussed above, compression-shear failure occurred near the top edge between the supported and clamped zones. Set up ‘B’ includes fixed support on the edges acting as anti-buckling elements with a square window opening. Nonetheless, a similar failure is observed in Case ‘A’. Set Up ‘C’ was designed to address this issue by splitting the fixture into two halves – upper and lower. The rectangular opening in the middle helped maintain the central surface free of additional supports.

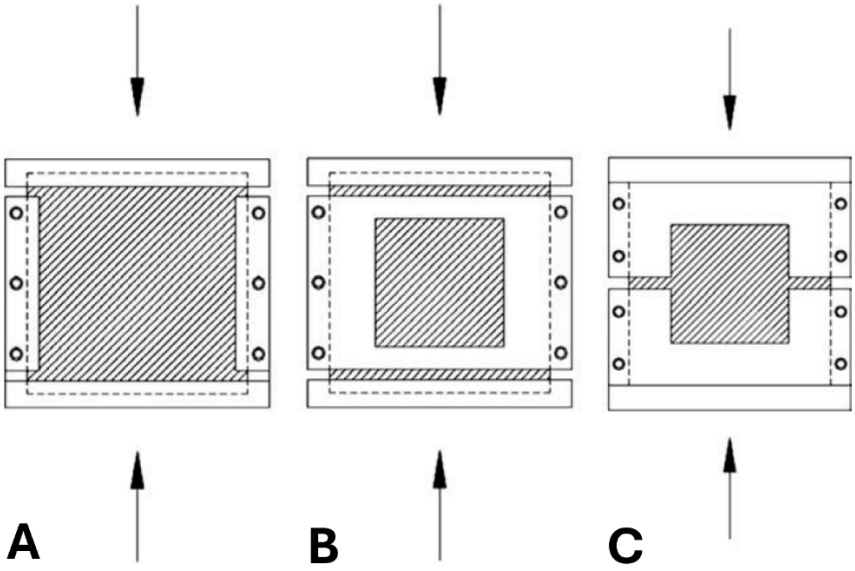

Figure 2.22. Initial CAI Devices (Sanchez-Saez et al. [127])

Figure 2.23 shows the final fixture design. The specimen is positioned in the fixture vertically between the front and rear anti-buckling plates. The rear anti-buckling plates are bolted to the top and bottom plates, thereby acting as fixed supports and providing rigid support behind the specimen. The front anti-buckling plates are removable; they help secure the sample with hand-tightened screws, allowing for free compression and

preventing global buckling of the sample. This design also accommodates samples of varying thicknesses. Tests indicated that this setup ensured failure occurred in the area damaged by the impact.

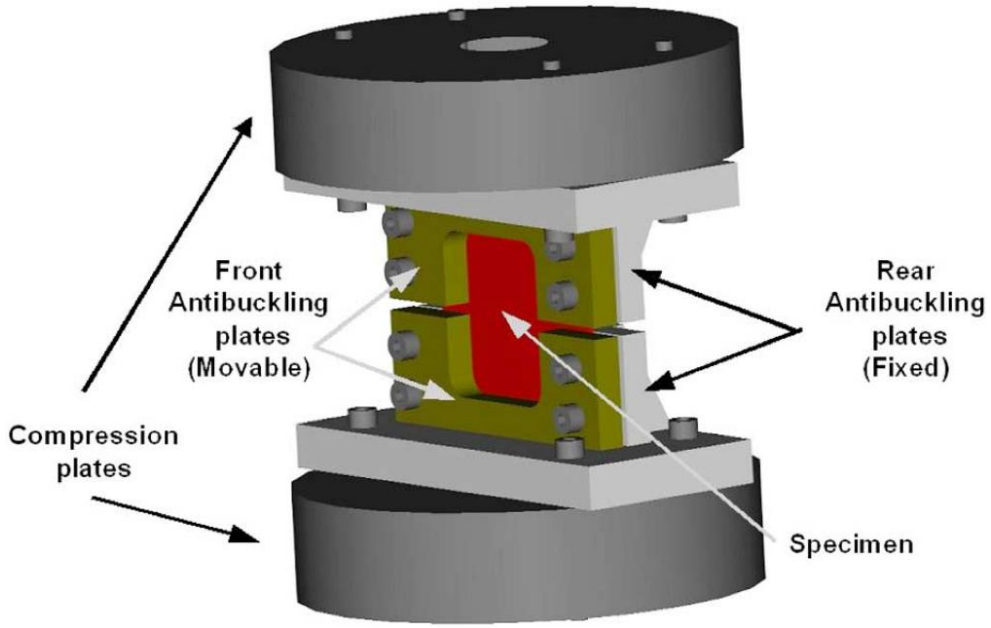

Figure 2.23. CAI Device (Sanchez-Saez et al. [127])

Wang et al. [134] predicted and verified the mechanical properties of a composite laminate struck by lightning through numerical simulation and experimentation. The authors utilized a specific CAI fixture as seen in Figure 2.24. The top clamp is a rigid plate that transmits compressive force from the testing machine to the sample. It supports the top edge of the sample and prevents any eccentric loading. Likewise, the bottom clamp secures the bottom edge and stops translation and rotation. There are side guides on both sides, which are essentially vertical plates that serve as anti-buckling supports to prevent out-of-plane deformation.

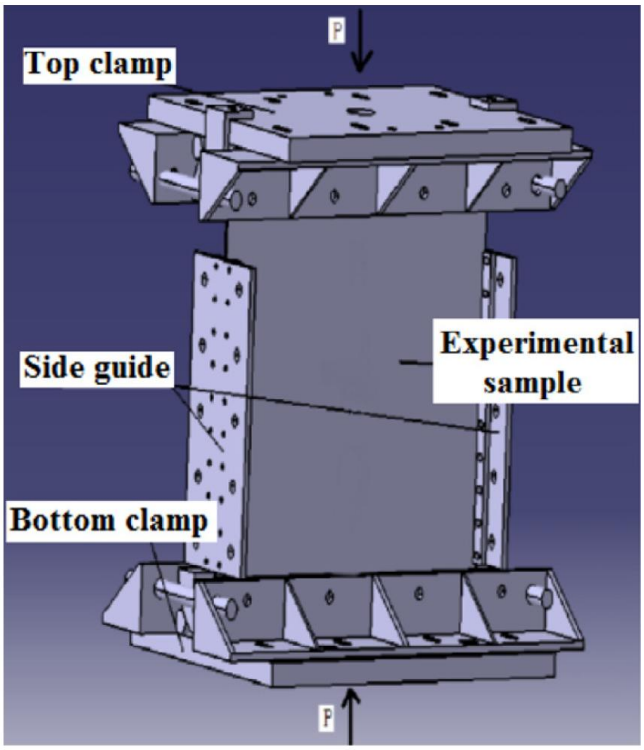

Figure 2.24. CAI Device (Wang et al. [134])

The preliminary designs obtained from the literature were crucial in further defining the characteristics of the fixture design, especially in the context of this study. Following this evaluation, a systematic and iterative approach was employed to refine and finalize the design.

2.3.2 Conceptual Designs

1. Design A

   Design A, also known as the “Photo Frame Design" is a symmetrical U-shaped frame featuring internal grooves to secure the test coupons and providing anti-buckling support. It will be a two-part assembly to ensure the specimen is vertically aligned. The open section in the middle offers sufficient visibility for the specimen to be struck by lightning.

Additionally, it provides space to expose the surface for visual monitoring, incorporating strain gauges and other measuring sensors. The intentional gap between the top and bottom sections ensures that the specimen is not over-constrained.

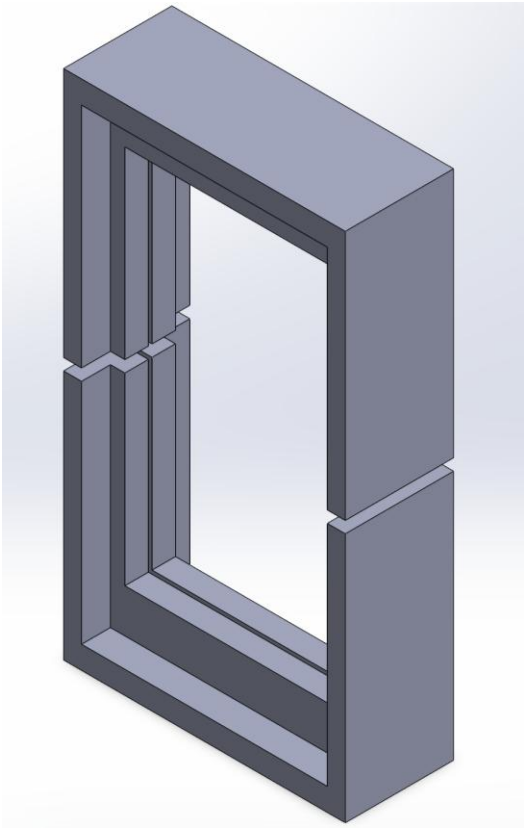

Figure 2.25. Conceptual Design A

2. Design B

Boeing or Airbus CAI Fixtures essentially inspire this design and have been sized according to the dimensions of the sample. It resembles Design A but features an extended base frame, which enhances the overall stability of the design. This effectively reduces the risk of tipping during loading. However, the absence of additional reinforcements may result in deformation when subjected to higher loads.

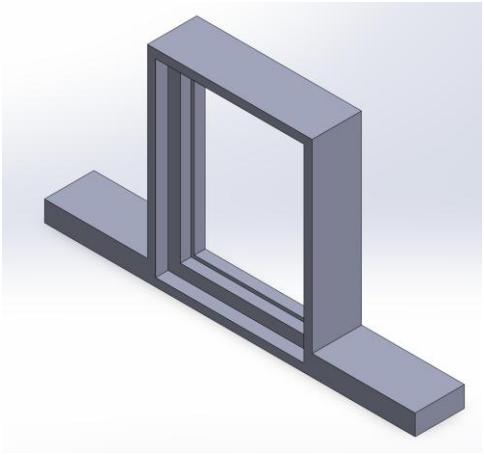

Figure 2.26. Conceptual Design B

3. Design C

   Design C builds upon Design B by adding triangular ribs on the sides that reinforce the structure. These features also enhance resistance to bending and shear deformations. This design will be advantageous for high-load composite testing; however, it will complicate the manufacturing and machining processes.

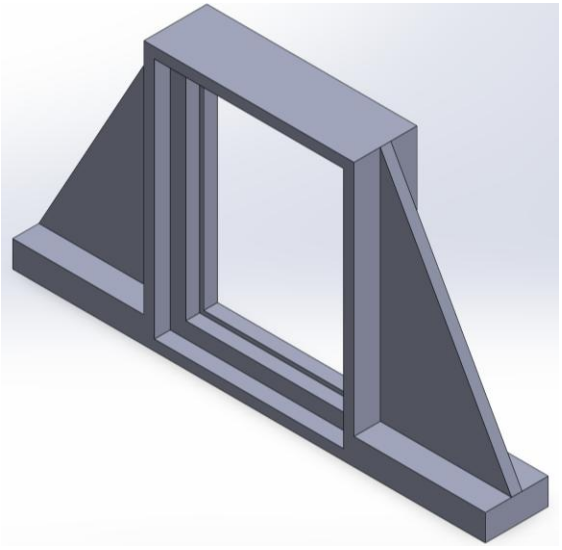

Figure 2.27. Conceptual Design C

Table 2-11 summarizes the three conceptual designs on qualitative metrics.

Table 2-11: Summary of Fixture Conceptual Designs

Parameter	A	B	C
Structural Simplicity	High	Moderate	Complex
Relative Ease of Manufacturing	Easy	Moderate	Complex
Modularity	Easy	Less Modular	Least Modular
Stability	Needs more quantification	Stable	Very Stable

At this stage, Design A was selected for its simple design and modularity. Although the current design lacks key elements, such as additional stiffeners and anti-buckling knife edges, it serves as a platform for further enhancements. Particularly concerning designs B and C, more complex modifications would be required to improve the fixture's ability to accommodate specimens of varying thicknesses. Additional iterations will refine Conceptual Design A by incorporating fasteners and removable anti-buckling plates to secure the sample and prevent out-of-plane deformation.

2.3.3 Iteration 1

The next design, which incorporates some of these modifications, is shown in Figure 2.28. This design incorporates additional modularity and details regarding assembly. The fixture consists of two front antibuckling plates and a fixed rear antibuckling plate, featuring additional protrusions with a perforated surface to secure the sample. This is accomplished through a dense arrangement of bolts running along the horizontal and vertical edges, which clamp the internal antibuckling

guides. This setup also ensures that uniform clamping pressure is applied to the specimen. The three-part fixture facilitates easy assembly and disassembly centered around the specimen.

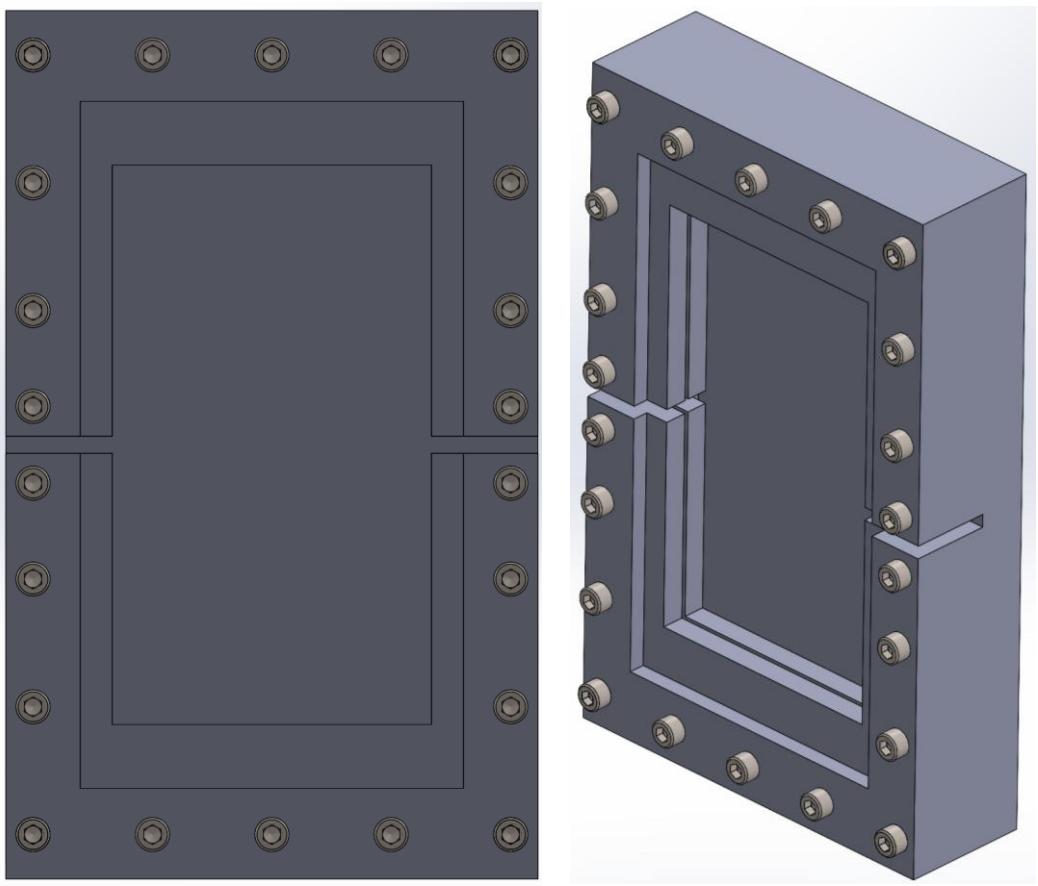

(a) Front View *(b) Isometric View*

Figure 2.28. Iteration 1

Thus, this fixture was able to maintain the essence of Conceptual Design A, yet it presented its own set of challenges. Particularly now that there is a fixed rear anti-buckling plate, it suggests that an undesirable moment may occur. A finite element analysis has validated this, as seen in Figure 2.29. The fixture is modeled as a steel structure, whereas the specimen is defined as a CFRP plate in a quasi-isotropic layup. It shows the total displacement to be 0.977 mm at a loading case

of 400 MPa. The deformation appears symmetrical, implying a balanced loading distribution; however, due to the rear antibuckling plate and the horizontal gap, the deformation only affects the top half of the fixture, thereby introducing an element of out-of-plane displacement.

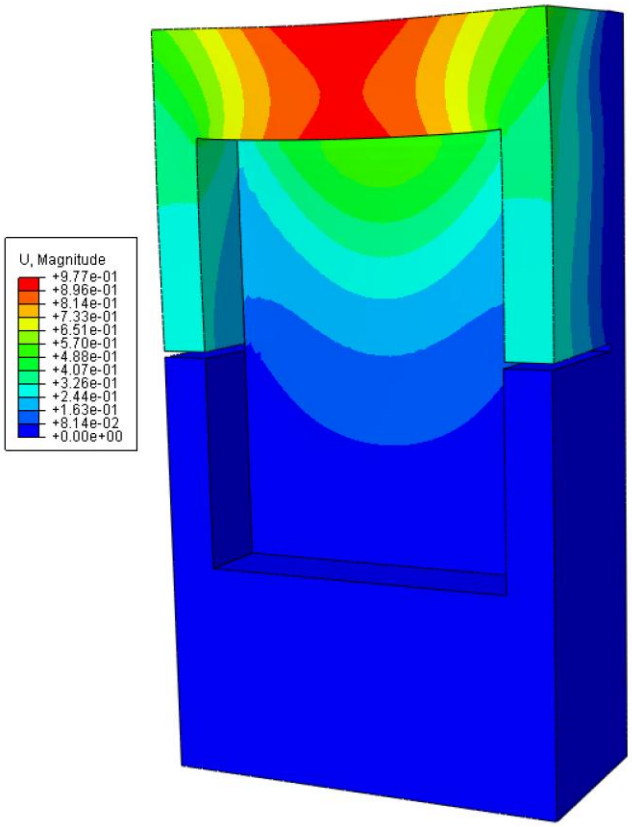

Figure 2.29. Fixture 1 Deformation (Scaled by 5, in mm)

Nevertheless, since the buckling of the sample was also a significant concern and constraint for designing the fixture, a buckling analysis was also conducted, as shown in Figure 2.30. The visualization is for Mode 1. It can be inferred that the fixture is rigid enough to permit deformation only within the sample, which confirms the effectiveness of the anti-buckling plate and the stability of the fixture. No additional asymmetry or lateral displacement of the specimen is observed. Since the fixture is not distorted from the FEA, it can be stated that it is functioning as intended.

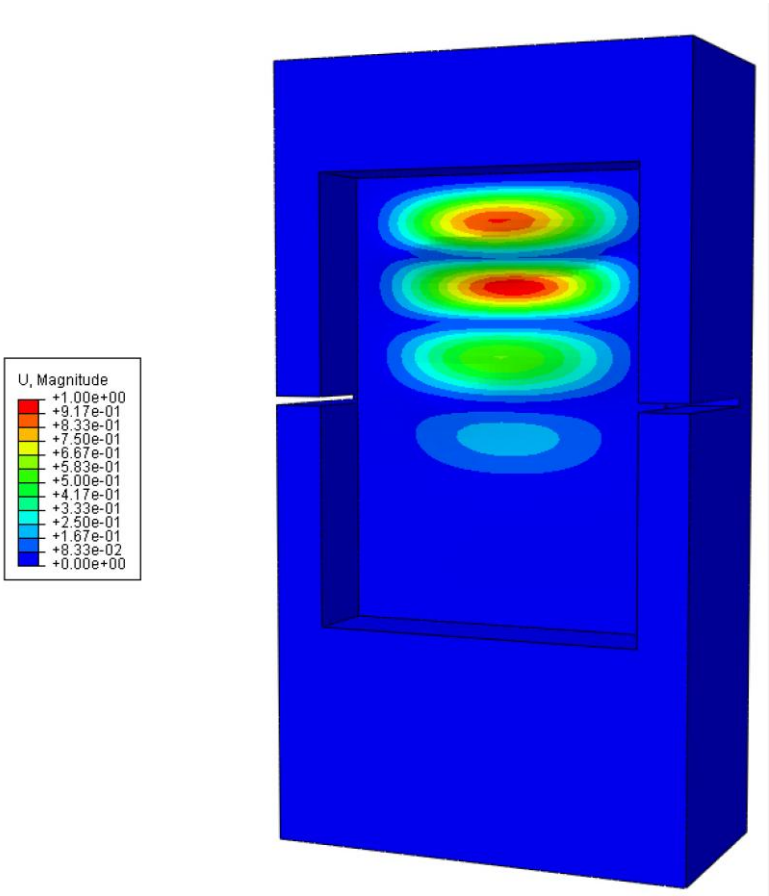

Figure 2.30. Fixture 1 Sample Buckling Mode 1 (Scaled by 10)

Based on the FEA and modifications made to this iteration during the conceptual design phase, the next iteration was developed.

2.3.4 Iteration 2

CAD models depicting Iteration 2 are presented in Figure 2.31. It integrates elements from Iteration 1 while preserving the essence of Conceptual Design A, particularly by maintaining a consistent gap between the upper and lower halves and incorporating a substantial window that exposes the surface to be struck by a lightning bolt.

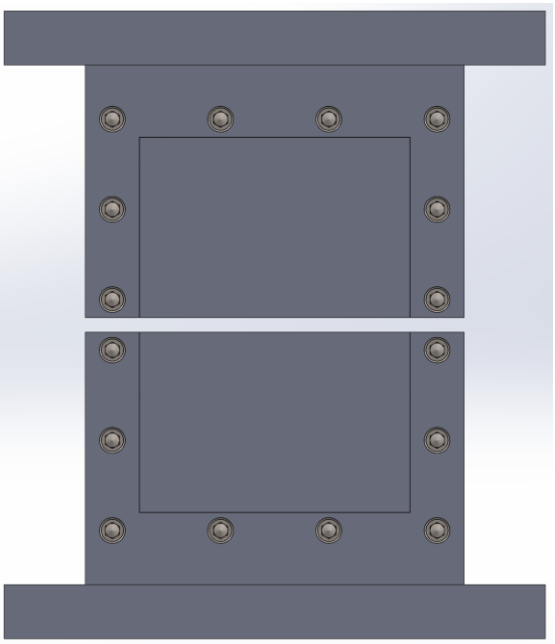

(a) Front View

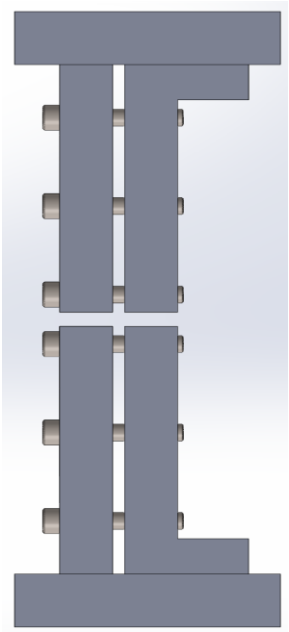

(b) Side View

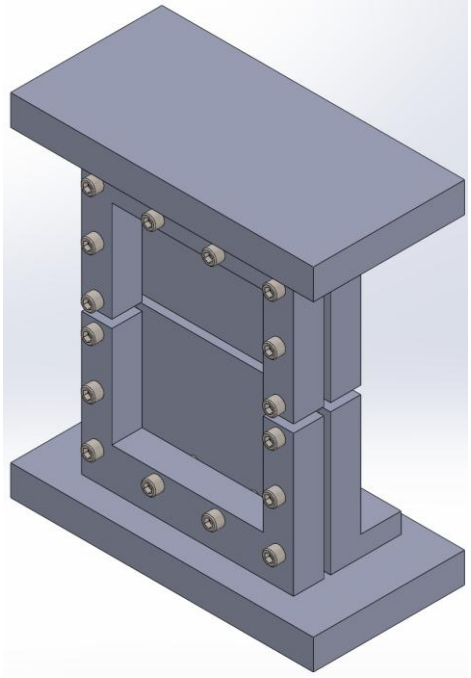

(c) Isometric View

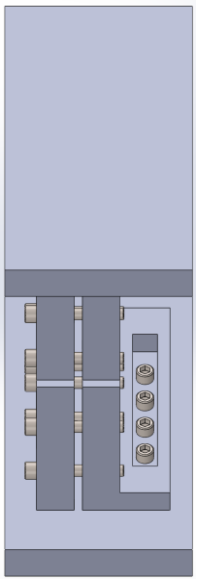

(d) Top-Down View of the Left Side

Figure 2.31. Iteration 2

Iteration 2 is a split-frame concept that can accommodate specimens of varying thicknesses and lengths. The fasteners used provide strong lateral bracing, ensuring mechanical stability. This fixture consists of an upper and lower half for easy insertion of specimens. Each half includes a base plate, which serves as a load transfer surface between the specimen and the load application system. These base plates secure the ‘L' shaped rear anti-buckling plates with five bolts that are horizontally aligned in a recessed rectangular pocket. The rear anti-buckling plates offer additional support to the specimen. The front anti-buckling plate secures the sample using uniformly distributed bolts that connect the front and rear anti-buckling plates, thereby restricting lateral deformation. The setup enables a systematic assembly process, facilitating standardization and repeatability. However, incorporating the rectangular pocket at the rear would require additional machining, particularly in managing tight tolerances, thus increasing production time and material costs. Moreover, this fixture design features sharp corners that can lead to areas of stress concentration.

2.3.5 Grounding Concerns

2.3.5.1 Definition and Previous Literature

The grounding of the sample presented a design challenge that required consideration, not only for safety but also for testing purposes. Lightning Strike Tests of CFRP laminates are conducted in such a manner that the discharge current strikes the center of the panel, followed by radial propagation to the ground electrode, typically through the edges of the specimen. Improper grounding of the specimen can lead to misrepresented results, as the discharge current is more likely to hit the edges of the ground electrode rather than interact with the sample. Here, grounding the sample specifically refers to maintaining equal potential across the specimen's boundaries,

thereby achieving circumferential grounding. This ensures there is a path for the electrical current even if it does not connect to the laminate. A series of experiments and a literature review were conducted by Yousefpour et al. [135]. Additionally, previous literature was examined, revealing three common trends as follows:

1. Use of a Dielectric Frame / Base Plate

   Some setups utilize a dielectric support frame, similar to the one used in the Feraboli Setup ([86], [87], [89]). These supports provide mechanical stability and electrical insulation by separating high-voltage electrodes from the base structures. This arrangement ensures that the current flows only through the intended discharge path, represented here by the copper strips used to ground the specimen. The copper strips connect the short ends of the specimen to copper electrodes.

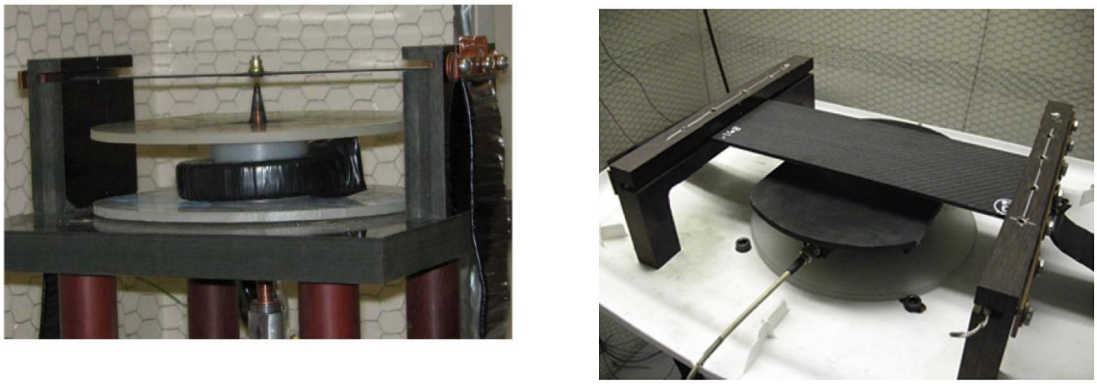

Figure 2.32. Feraboli Fixture ([86], [87], [89])

Similar to the previous setup, the Hirano Setup (Figure 2.33) uses two glass fiber-reinforced polymer (GFRP) laminate plates, each 15 mm thick. One plate holds the discharge probe, while the other supports the specimen. CFRP threaded rods adjust the distance between the probe and the plate. A copper sheet is placed beneath the lower plate

to establish a grounding surface and facilitate a path for electrical discharge from the side surfaces to the copper plate. However, one potential concern with using a similar grounding setup is that it may lead to asymmetric grounding, resulting in nonuniform current distribution. This can cause uneven damage and data inconsistencies, especially in wide specimens.

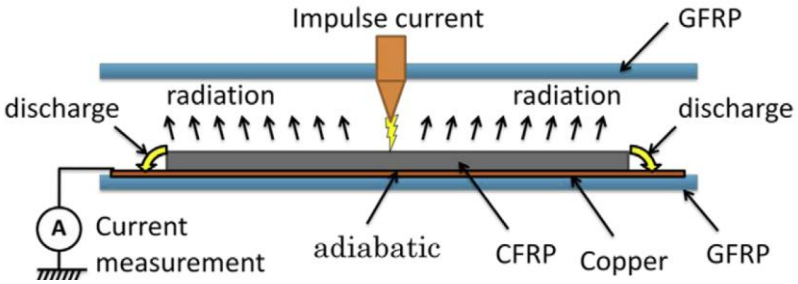

Figure 2.33. Hirano Setup ([92], [109])

2. Use of Silver Paint / Complaint Foil / Copper Bars

Another frequently employed strategy is the use of copper foil and silver paint on the specimen's edges. This setup has been shown to improve the quality of grounding and current injection performance. Silver paint forms a conductive layer, and copper provides a highly conductive grounding terminal, forming an efficient electrical interface. An example as used by Harrell et. al [93] is shown in Figure 2.34.

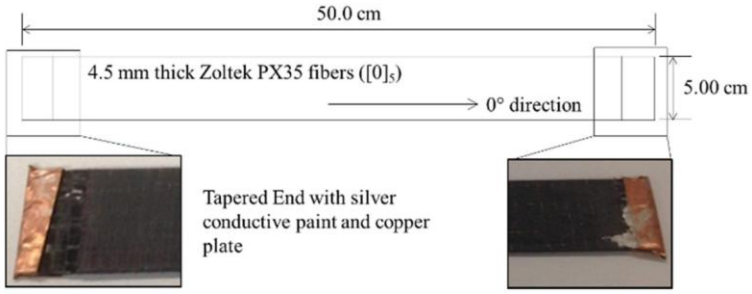

Figure 2.34. Harrell et. al. ([93])

Similarly, another method involves using copper bars as electrodes. They can be integrated into the fixture or attached to the edges. This can be seen in the fixture used by Tian et. al. ([95], [96]). The discharge electrode is the positive electrode that sends current to the CFRP specimen. Negative copper electrodes at both ends of the specimen serve as ground terminals, allowing current to flow laterally from the discharge point to the ground terminals.

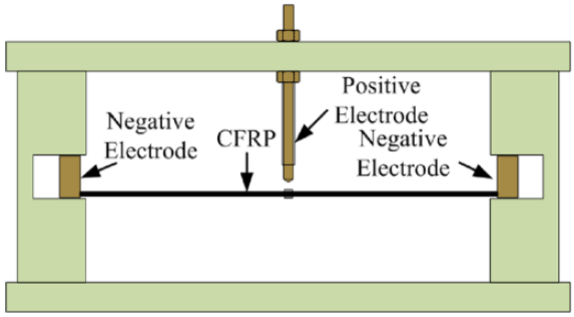

Figure 2.35. Tian Fixture. ([95], [96])

In a similar fashion, the grounding scheme used by Guo et al. ([94], [103], [104]) shows the specimen mounted horizontally, with the discharge electrode positioned perpendicular

to it. All four sides of the specimen are wrapped in conductive acrylic adhesive copper foil tape, which is tightly embedded between two copper bars. The clamping force is provided by G-clamps made from polyamide, resulting in the formation of an equipotential boundary essential for circumferential grounding. The entire fixture is secured to a glass fiber/epoxy bed, which uses two brass bars to connect the system to the ground.

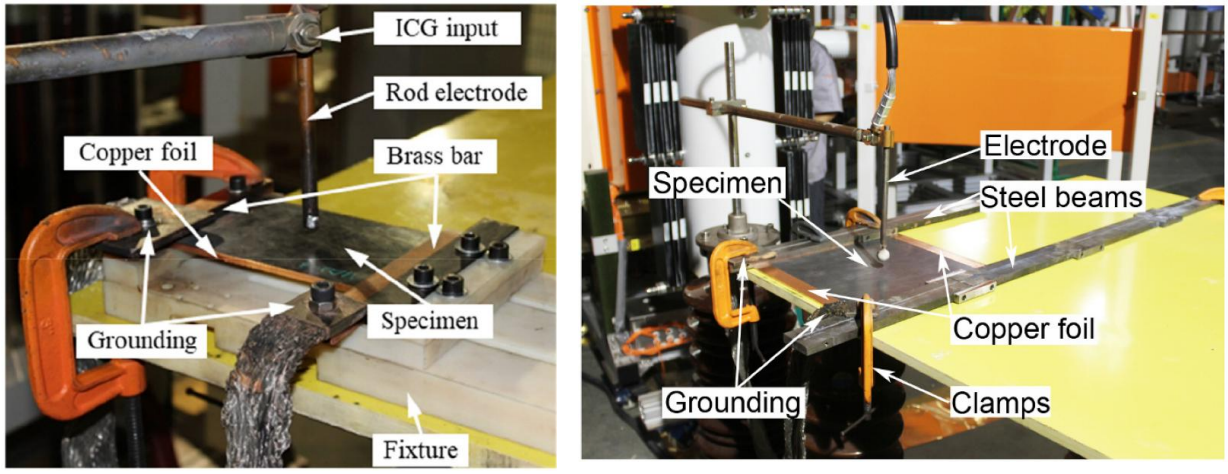

Figure 2.36. Guo Fixture ([94], [103], [104])

3. Frame Setup & Grounding Clamps

Xu et al. [126] had test specimens bolted into a grounded rig at opposite ends of the sample. The discharge electrode is positioned above the sample. The bolted connection runs along the short edges, ensuring firm and tight contact between the specimen and the grounding clamps. This serves as the primary route for grounding the sample, thus creating a path for the injection of current into the specimen.

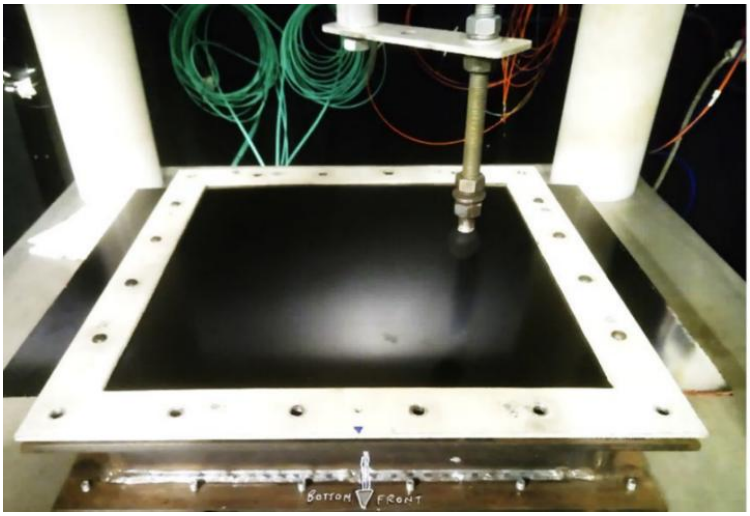

Figure 2.37. Lee Fixture ([126])

2.3.5.2 Proposed Grounding Schemes

Based on the literature and technical input, the following two grounding schemes were developed:

1. Proposal 1

   This approach essentially follows the methods outlined in the literature. The edges of the specimen will be painted silver, and a layer of compliant foil, such as those made from copper or aluminum, will be placed on the top and bottom edges. The fixture will provide the necessary clamping force to ensure a strong connection. Additional copper straps will be used to bond the specimen to the ground.

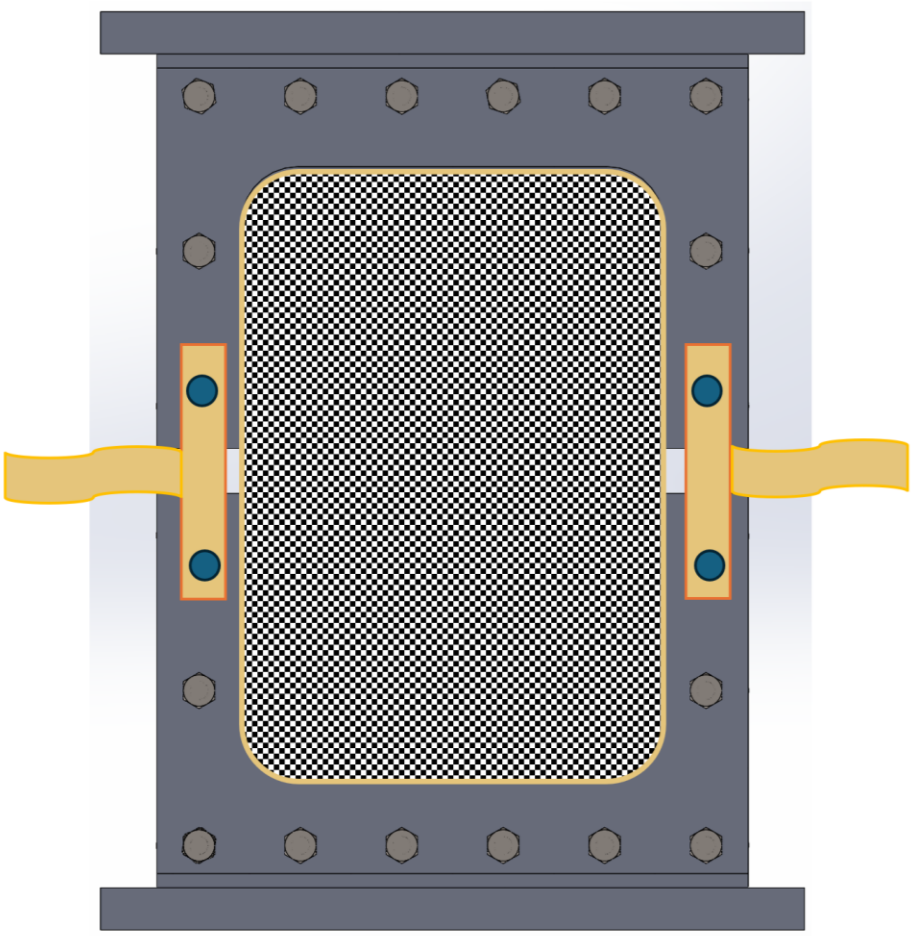

Figure 2.38. Proposal 1 Schematic

2. Proposal 2

   An alternative would be to use two U–shaped copper fixtures. This would require adding bolts to the sample to help secure the copper frame and create a path for the current to the ground. The two halves would connect with a copper braid or thick copper foil to form a complete circuit path.

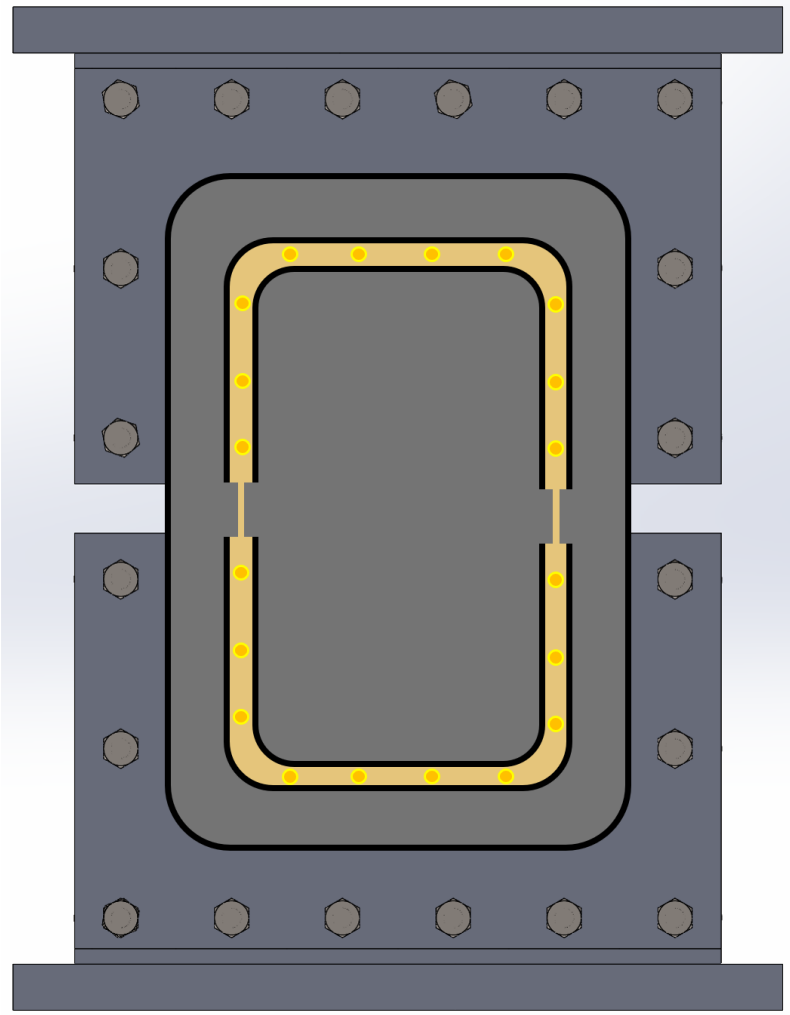

Figure 2.39. Proposal 2 Schematic

At this stage, both proposals were considered. However, it was decided to conduct initial tests to understand the lightning discharge and evaluate the strategy outlined in Proposal 1. Based on the test results and performance, we will either proceed with Proposal 1's grounding scheme or test Proposal 2.

2.3.6 Final Design

The final fixture design has been illustrated in Figure 2.40 and Figure 2.41. This design is the culmination of the previously discussed designs. Similar to Iteration 2, this fixture consists of six components: a top plate, a bottom plate, two front anti-buckling plates, and two rear anti-buckling plates. The rear anti-buckling plates are bolted directly to the top and bottom plates, removing the need for a recessed cavity in the earlier design. The front anti-buckling plates continue to feature window-like architecture, incorporating curved edges to minimize stress concentration. External bolts and wing nuts are used to secure the specimen between the two antibuckling plates, accommodating specimens of varying thicknesses. The preference for wing nuts allows for tool-less tightening, making assembly and disassembly easier. Taking inspiration from the ASTM 3410 compression test fixture [136], guide rails were incorporated to create a linear path for the movement of the top and bottom halves, thereby preventing any undesirable loads on the specimen. The CAD model depicts a copper frame as a representative example of grounding, as discussed in the previous section. Although not shown here, the fixture will have a 2-inch-thick plate of Garolite to insulate it and ensure that there is no charge transfer from the fixture to the hydraulic press.

This fixture showcases a robust design, utilizing thick top and bottom loading blocks to ensure minimal deformation under high compressive loads. It also promotes proper specimen alignment while maintaining pure compression loading throughout the test duration. This design ensures repeatability and reproducibility of the test, thereby providing consistent results. Compared to earlier designs, the final iteration excels in structural stiffness, accessibility, modularity, and aesthetics. However, it is a complex system to assemble for the first time, incorporating over 30 nuts and bolts of varying sizes, which adds extra time to the assembly process. The thick plates

will also increase machining time; however, these challenges do not outweigh the benefits of using this fixture. Further tests will be conducted to ensure the validity of the system.

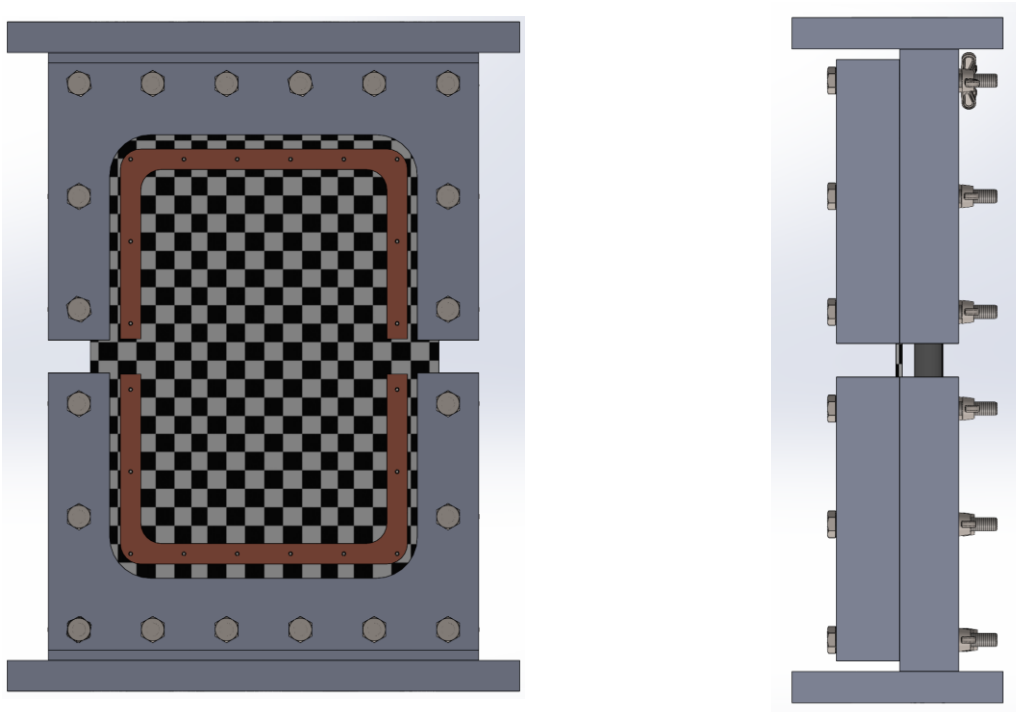

(a) Front View *(b) Side View*

Figure 2.40. Final Fixture Design

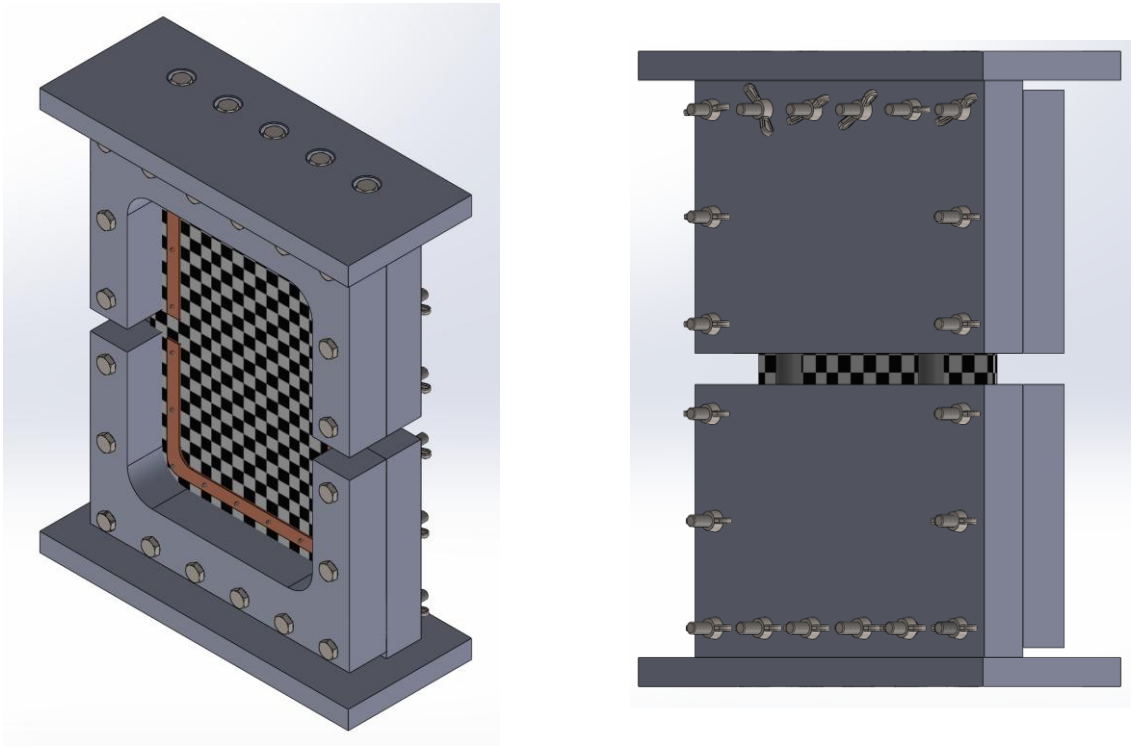

(c) Isometric View *(d) Rear View from the Right Side*

Figure 2.41. Final Fixture Design

2.4 **Circuit Design**

The schematic of the high-voltage (HV) discharge circuit (Figure 2.42) illustrates the setup that will be used to simulate lightning strikes. A HV power supply had to be obtained from the local power company to charge the capacitor bank, which is connected by a switch referred to here as SW 2. SW 2 is an HV relay, specifically a double pole double throw (DPDT) relay. This circuit utilizes a Gigavac G 23 Relay, composed of two single-pole double-throw relays. Between the capacitor bank and the HV supply is a diode known as the shaping diode, which modifies the shape of the input waveform and prevents current from returning to the HV supply during the discharge phase.

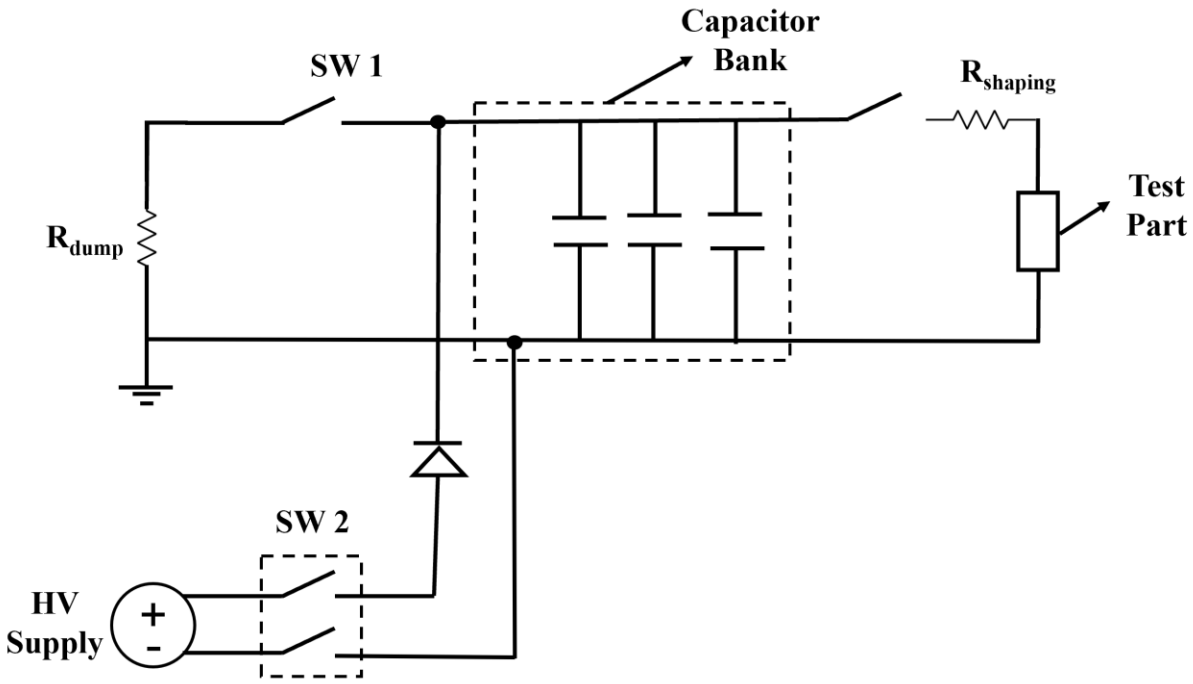

Figure 2.42.Circuit Diagram (Original Design by Dejan Nikic)

The capacitor bank consists of 12 capacitors that store electrical energy and serve as the primary energy source for impulse discharge. The shaping resistor, a 100-milli-ohm HV-rated resistor, controls the pulse shape and delivers the final high current pulse from the capacitor bank to the test part. SW1 is a single-pole single-throw (SPST) HV relay used to close the circuit and discharge the capacitors. The dump resistor, a 200-ohm HV-rated resistor, is connected to the capacitor bank and discharges residual voltage gradually to prevent electrical shock. There are three operating states: Dump, Charge, and Fire. The Dump State is the default operation mode, used to discharge the residual voltage from the capacitors. The Charge stage connects the HV power supply to the capacitor bank for charging. Finally, the Fire stage disconnects the circuit from the power supply and the dump resistor to initiate the impulse to the test part. The configuration of the switches is shown in Table 2-12.

Table 2-12: Switch Configuration

State	SW 1	SW 2
Dump	ON	OFF
Charge	OFF	ON
Fire	OFF	OFF

2.5 Cart Design

The design of the cart focuses on housing the capacitors within a mobile frame. This mobility is necessary for moving the cart as needed, since the final location of the system was not determined at the project's design stage. Additionally, it must feature a modular design and be capable of mounting surfaces to accommodate components necessary for constructing the circuit. Another requirement is to ensure that the ignitron remains in a vertical position to prevent corrosion of the anode, which could occur if the mercury inside the ignitron is not kept level.

The high-voltage capacitors are represented as cyan boxes within a protective enclosure. They are arranged in a symmetrical grid layout, which helps distribute weight and enhance the cart's balance while optimizing the design for space and footprint. The capacitors are configured in a 6 x 2 arrangement with a gap in the middle to accommodate the ignitron's placement. Copper busbars run horizontally along the length of the capacitor cart, connecting the capacitors by providing a low-resistance path for current flow. The stainless-steel frame offers mechanical support and shields the capacitor array. It features top and mid-structural rails for added stability. Additionally, the holes in the sides of these slotted channel bars indicate that they can be used for modular assembly, offering flexibility in mounting points for the cart as well as additional components on the surface. The wheels attached to the bottom of the frame allow the unit to be mobile, while a locking mechanism secures the entire cart in place. The ignitron, depicted in purple, is oriented vertically and attached to a plate secured to steel bars running along the length of the cart. The

plate is illustrated here as a grey surface at the center. The wires will connect it to the shaping resistor, which is mounted on the long arms extending from the cart's side. At the end of the arm, known as the discharge arm, a vertically oriented rod holds a horizontally aligned discharge probe. This probe delivers the final lightning shot to the test part.

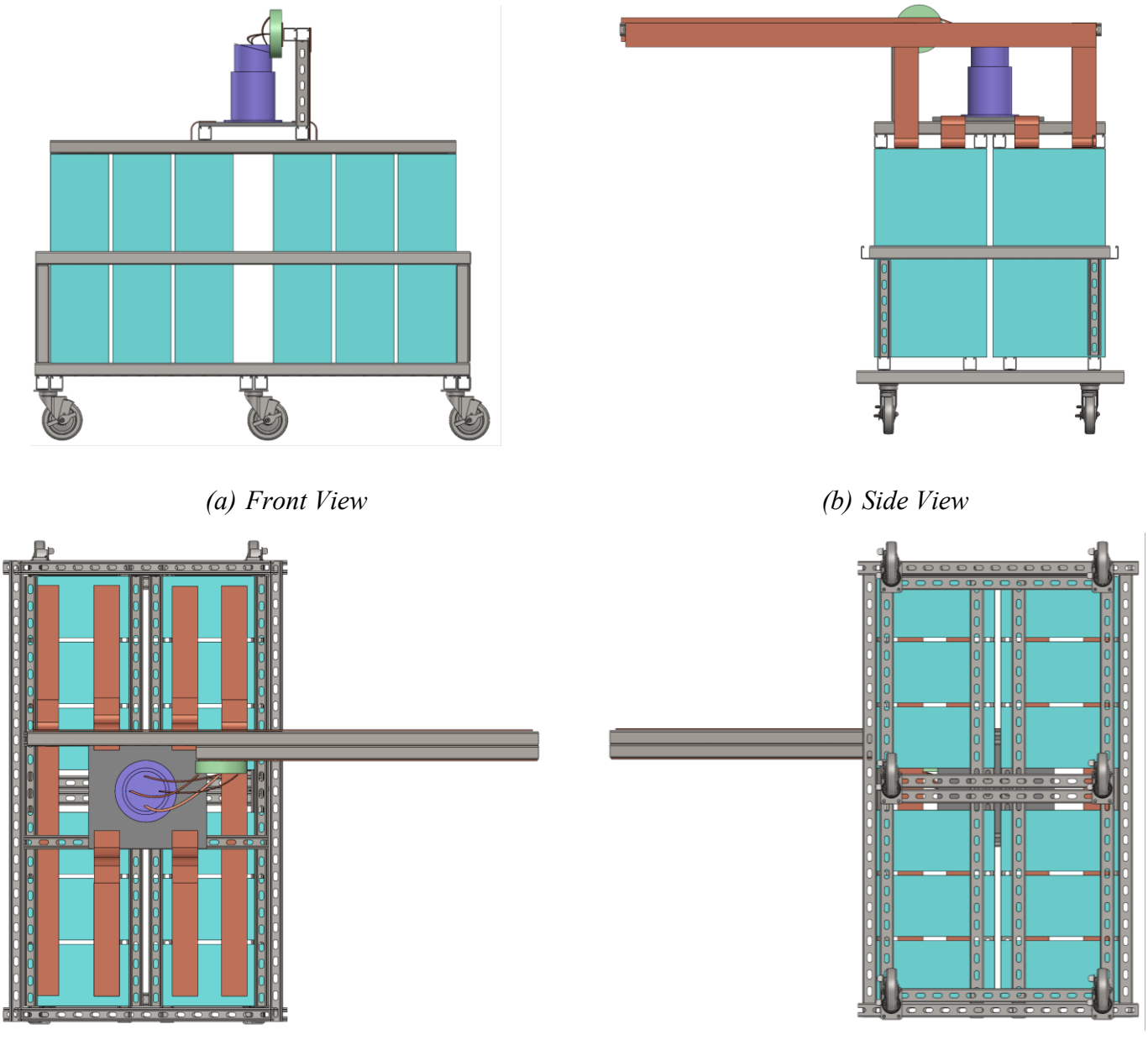

(a) Front View *(b) Side View*

(c) Top View *(d) Bottom View*

Figure 2.43. Capacitor Cart CAD (Courtesy Kameron Harmon)

Chapter 3: System Manufacturing and Testing

3.1 Manufacturing and Assembly

3.1.1 Sample Manufacturing

The samples with the specified dimensions outlined in Section 2.2 were manufactured to evaluate their damage characteristics. The hand layup process was utilized because it requires a flexible and straightforward setup for small production runs and is ideal for fabricating flat shapes, such as plates. Although this process is labor-intensive, it is sufficient to produce standardized specimens for use in this study. Of all the prepreg material available in-house, unidirectional Hexcel IM8GS–12 / M65-1 was selected because it was the one closest to the appropriate ply thickness. It has a nominal fiber areal weight of 190 GSM and a resin content of 35% by weight. The material is stored in a controlled freezer at a temperature of 10°F, as advised by the manufacturer. The material was cut into the appropriate number of plies in the correct orientation and dimensions using a Zünd G3 fiber cutter [137] available at the Advanced Composites Centre, University of Washington, as shown in Figure 3.2. A flat aluminum tool was used to lay up the piles, which were sanded down before each layup and then cleaned with acetone to achieve a better surface finish. The release film was spread evenly on the tool, avoiding the formation of air bubbles, and secured with flash tape. The plies were laid up layer by layer according to the desired schedule: [45 °/0 °/- 45 °/90 °/45 °/ 0 °/- 45 °/90 ° | |90 °/- 45 °/0 °/45 °/90 °/- 45 °/0 °/45 °]. The first specimen was manufactured, vacuum-bagged, and cured in the autoclave available at the UW ME composite shop, following the manufacturer's cure cycle [138]. Later, the autoclave was out of order due to pressurization issues, so the heated platen press was used as an alternative. The curing recipe was modified to comply with the platen press and is shown in Figure 3.1. Following the cure, the samples were

stored carefully. Once sufficient samples were manufactured and cured according to the manufacturer's data sheet, a post-cure cycle was initiated, as shown in Table 3-1 was followed to complete the manufacturing process.

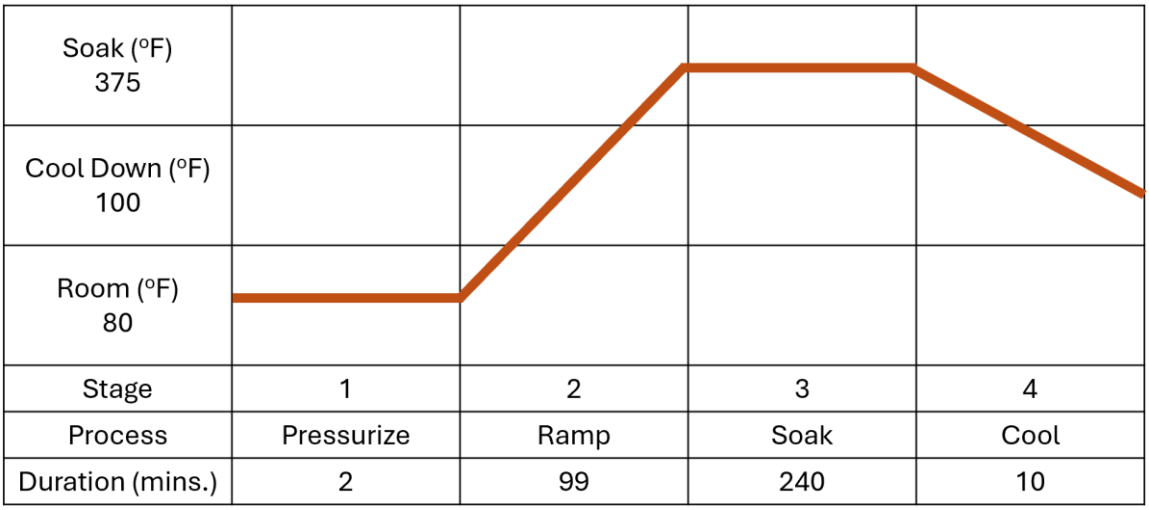

Figure 3.1. Platen Press Curing Cycle

Table 3-1: Post Cure Cycle

Stage	**Process**	**Target Temp. (°F)**	**Rate (°F/min)**
1	Ramp 1	Ambient to 375	5 - 10
2	Ramp 2	375 to 470	1 - 2
3	Soak	470	6 Hours
4	Cool	470 to ambient	-

Figure 3.2. Zünd G3 fiber cutter in action

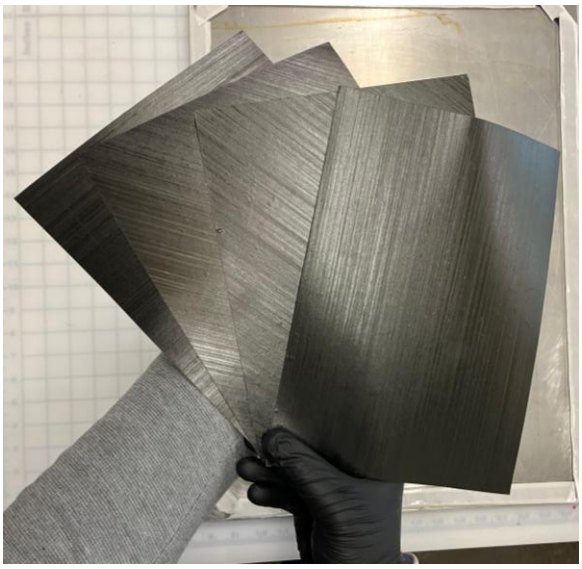

Figure 3.3. Plies after being cut

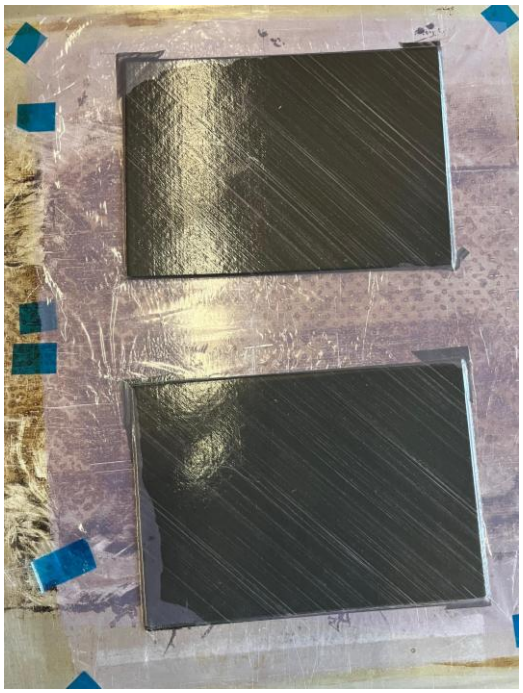

Figure 3.4. Laid up specimens before curing them in the platen press

Figure 3.5. Heated platen press available at the UW ME Composite Shop

The samples were oversized by 2 cm on each side to account for manufacturing defects along the outer edges, enhancing the consistency of the final product. Subsequently, they were cut to the desired final size using a wet saw. Over 30 specimens were prepared, and some would undergo further modifications in the future.

Figure 3.6. Wet Saw

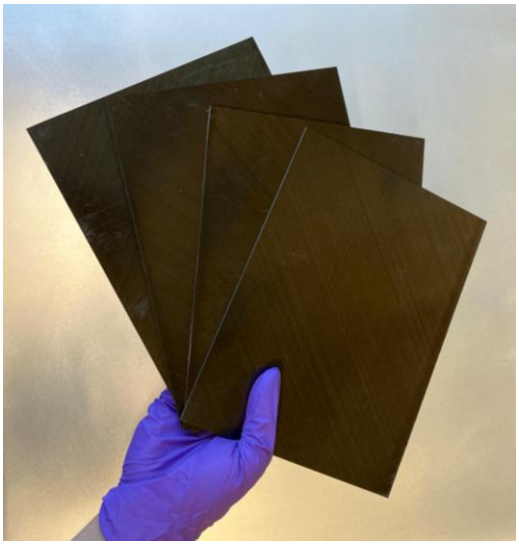

Figure 3.7. Final Specimen

3.1.2 Fixture Manufacturing

The fixture is designed to securely hold the specimen during both compression and lightning discharge testing procedures. It consists of six essential components: two rear anti-buckling plates, two support plates, and two front anti-buckling plates. These critical components are bolted together to create a robust and stable configuration that reinforces the integrity of the entire assembly. Each element was fabricated to strict dimensional tolerances, adhering to the design

specifications, which are vital for the fixture's proper functioning. Manufactured from high-strength steel, the fixture ensures exceptional durability and wear resistance under extreme conditions. The rear anti-buckling plates, along with the top and bottom plates, were cut to the specified dimensions using various milling techniques.

Figure 3.8. Fabricated Fixture

A critical aspect of the machining process involves drilling holes for bolts, which must be executed with precision according to engineering drawings. This ensures that there is no interference between the bolts connecting the rear anti-buckling plate to the top and bottom plates, and it guarantees a secure connection between the rear anti-buckling plate and the front anti-buckling plate, which is responsible for securing the specimen in place during testing. To ensure a robust assembly, the rear anti-buckling plate is secured to the top and bottom plates using ¼” – 28 hex

bolts, each measuring 1.75 inches in length. These bolts are carefully installed through counterbore holes, ensuring they are recessed within the surface, thus providing a flush and clean finish that maintains the surface flatness required for optimal performance. The front and rear anti-buckling plates are secured with 3-inch-long ¼" – 28 hex bolts. Furthermore, the rear plate is equipped with two strategically positioned holes that allow a 4-inch steel rod to pass through, connecting the upper and lower halves of the fixture. This design effectively creates a useful pathway for the fixture to move along when a load is applied, while also facilitating ease of assembly and disassembly during the experimental process.

Figure 3.9. Fabricated Fixture: Top and Bottom Halves

Additionally, the front anti-buckling plates were initially milled using a vertical CNC machine to achieve the necessary internal geometry required for assembly. The corners of these plates were further machined with a corner-radius mill to precisely attain the specified dimensions, enhancing the fixture's overall capability. The bolt pattern was carefully established through precision drilling

and tapping holes to securely clamp the specimen between the front and rear anti-buckling plates. Moreover, the rear anti-buckling plate is designed to be slightly recessed by 2 mm to accommodate the thickness of the current specimen being tested, which in turn enhances the clamping force exerted by the friction plate positioned between the specimen and the anti-buckling plates in addition to act as a surface to transfer current from the specimen to the fixture and onward to the grounding straps attached. The upper and lower sections of the fixture also feature a substantial 2-inch-thick block of Garolite, which effectively insulates the specimen and prevents any charge transfer to the hydraulic press, thereby maintaining safety and functionality during the tests.

Figure 3.10. Fixture with sample

Figure 3.11. Placement of the fixture on the press

3.1.3 Cart Assembly

The initial design of the cart features an integration of high-energy capacitors along with their corresponding circuit components, all neatly housed within a custom-built, modular, and mobile framework. This design places a strong emphasis not only on mechanical stability but also on adequate grounding and modularity, facilitating ease of access for maintenance and upgrades, while ensuring compliance with stringent safety standards governing high-voltage operations.

In the first phase of the assembly process, the base support frame was manufactured using durable steel tubing, which was subsequently assembled into a robust structure. To enhance mobility and functionality, caster wheels were attached to the bottom of this frame. Following this, a forklift was used to lift each capacitor into position carefully; these capacitors were then manually placed in their designated locations. To further ensure stability, additional crossbars were integrated into the framework, providing necessary support and acting as a secure mounting surface for the electrical components. The precise arrangement of the capacitors was deliberate to achieve a symmetric pattern. This symmetrical placement significantly aids in balancing the overall weight distribution, which is crucial for efficient operation.

Copper busbars were then cut to the necessary lengths, and holes were strategically positioned at pre-designated locations to enable electrical connections between the hot and ground sides of each capacitor. A center plate was employed to form a secure and reliable connection to the ignitor, thereby facilitating the creation of an efficient electrical pathway using the copper busbars. This arrangement provides a meticulously controlled conduction path that prevents any unintended arcing, which could pose safety risks.

The ignitron is connected seamlessly to shaping resistors through the use of braided copper wires. The shaping resistors are firmly mounted on the extended arm of the configuration. Progressing from this point, the design includes a discharge arm that can translate smoothly across the length of the vertical bar. This feature allows the setup to accommodate a variety of specimens for experimentation, ensuring versatility in application. The energy transfer to the probe occurs through this discharge arm, which plays a critical role in delivering the final shot to the specimen in a controlled and effective manner.

Figure 3.12. Final Assembled Cart

3.1.4 Overall System

This section provides a detailed explanation of the system's operation. The igniter triggers the cascade effect and connects the power supply to the ignitron using two sets of wires. The negative or ground side of the circuit is the outer edge of the capacitor array on each side; these will connect

to the building's ground, which will be a support column nearest to the capacitor cart. The copper busbars of the ground side are placed lower and closer to the capacitors, while the hot side, or positive side, is mounted at a higher height. This further differentiates the positive and negative sides of the capacitor array. The hot side copper bars are connected to a platform that secures the ignitron. All surfaces were mechanically abraded before being fastened together to ensure the best possible electrical connection. The two relays (SW1, SW2) are grounded together through the dump resistor, which has its ground side at the bottom and its hot side at the top. Relay (SW2) is usually closed. Once connected to the HV supply, the relay opens, allowing the capacitors to charge up and develop a potential difference between the gaps. In the event of a power loss, the system's default safety setting transfers everything to the dump resistor. Two safety wires connecting the capacitors' ground and hot sides will be disconnected when charging. The capacitors cannot be charged until those wires are removed, serving as a safety mechanism. The relay is connected to the power supply, which is plugged into a 120V wall socket. The capacitors are 14 μF and are rated for 25 kV applications; however, for this project, they will only be charged up to 10 kV.

The power supply module is placed on the lower deck of the control station. When a lightning shot needs to be fired, the power will travel through the capacitors to the ignitron, which connects to the shaping resistor using braided copper wires. The resistor then connects through another thick, braided wire to the discharge electrode. The discharge electrode can translate vertically, accommodating various parts being tested. It has a red, spherical shape and is connected to the test part with a thin copper wire. The lower part of the ignitron is the hot side, located directly beneath the mercury chamber. When a voltage is applied from the ignitor through two leads, it generates a

potential difference that results in a breakdown, allowing additional capacitors to discharge across the gap. The top section of the ignitron connects to the shaping resistors using braided copper wires. Shaping resistors are mounted on the top busbars, which are secured with bolts and connected by a copper strip to ensure an electrical connection. A braided cable will be attached to a fiberglass rod, providing an additional layer of grounding and protection.

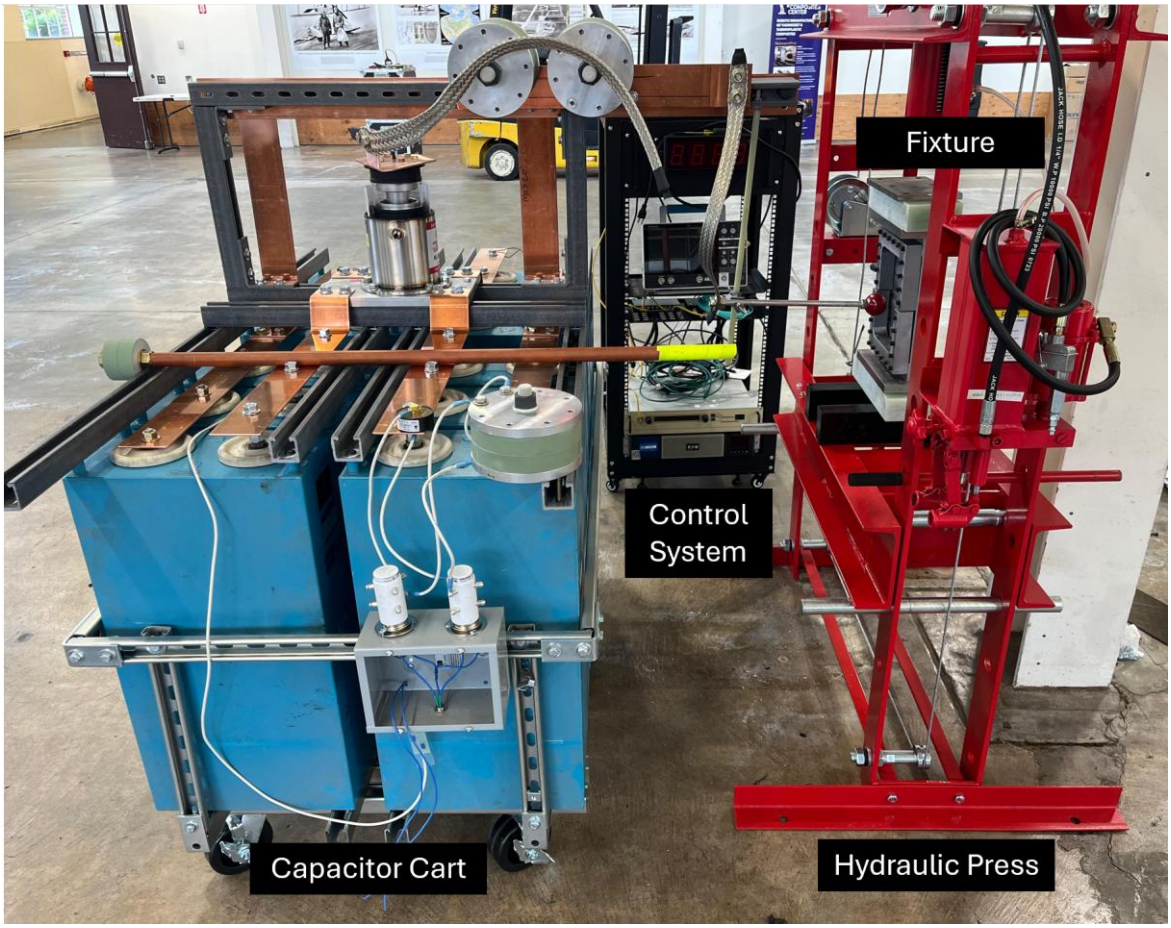

Figure 3.13. Overall System

The control system includes a Programmable Logic Controller (PLC) connected to a relay for the 120 V power supply and a UPS backup located underneath it. The system is plugged into a wall socket, allowing power to flow through the relay to the UPS. The UPS then provides power back

to the control system, creating backup power for all essential electronics that must operate during system use. When the control system relay is open, power is supplied through the UPS to the PLC, system network, and voltmeter. All components are connected through a switch, which links to a fiber optic cable attached to a computer used to control the system. This computer will be situated at a significant distance from the apparatus to ensure user safety. A custom cable is hooked up to the relay, providing control over it; this wire is also connected to the voltmeter to display the readings. Another optical wire will connect the setup to the blue box, which essentially acts as the command switch for the actual lightning shot.

(a) Hydraulic Press with Fixture *(b) Control System*

Figure 3.14. Overall System

3.2 **Preliminary Test Plans**

3.2.1 Safety Audit and Configuration Check

Before the system is used for any testing, it must undergo an extensive safety audit and the preparation of Standard Operating Procedures (SOPs). Key checks include ensuring that all ground straps are securely connected to a verified ground point, particularly the building's central pillars; confirming that the air gap between the busbars is adequate; and ensuring that the discharge to the dump resistor is both safe and proper. Additionally, all mechanical fasteners should be securely bolted, the wheels must be locked to prevent unnecessary movement, and the structural integrity of the frame must be verified. Furthermore, the system will be secured in a cage to ensure that only authorized individuals can access it, and a manual key will be used to connect the high-voltage power supply to the capacitors. The HV power supply will be connected with a special cable that will be locked up and used only when needed, adding another layer of safety.

Once the system is assembled and passes the safety audit, a series of initial low-voltage tests will be conducted to ensure the electrical integrity and functionality of the system. These tests are crucial to confirm that the preliminary checks have been thoroughly established and that the current flow is occurring as expected. This will be followed by a fail-safe and logical circuit check to evaluate whether the relays and associated systems are operating as intended. Only after these validations are completed will the system be deemed electrically sound, allowing it to be utilized for full-scale testing.

This setup will focus on a scaled-down version of waveform A with an amplitude between 30kA and 50kA, specifically concentrating on Zone 2A as defined in SAE ARP 5412 and 5414 in Section 1.3.

3.2.2 Validity of Fixture: Dry Tests

To validate the fixture's functionality, a series of dry tests were conducted, using specimens tested under load to measure failure loads and evaluate damage characteristics. This also provided an opportunity to identify any mechanical issues that could be addressed before performing the actual test.

To begin, there was concern that the fixture might topple under load, potentially falling forward or backward, which would have been unacceptable. To ensure stability, it was decided to mount the base plate to the hydraulic press bars. This was not an issue during the dry runs being tested, but a potential solution remains available in case the project is scaled up in the future. Additionally, the 2-inch block of Garolite was required to insulate the sample and provide an alternative loading path. However, there was concern that the Garolite G10 might become indented due to repeated tests. Thus, a thick plate of steel was added on top to prevent that.

This also presents an opportunity to determine the process of securing the specimen and documenting it. The top half of the fixture will be removed first, followed by the careful removal of the front anti-buckling plate, which creates a gap for inserting the sample and ensures proper alignment. Following this, it will be assured that a friction fit is maintained. After that, the rear anti-buckling plate is placed on top, and the guide rail helps position it correctly. Finally, the front anti-buckling plate of the top half is inserted and bolted, thus securing the sample.

The setup for the preliminary dry tests has been shown in Figure 3.15.

Figure 3.15. Dry Test Setup

To also quantify the fixture design against the design criteria, one of the plates was used to create compression test specimens following ASTM D6641 [125]. The tab length and gauge length were established based on the material property estimates provided by the manufacturer. The test was carried out at the UW ME Mechanical Test Shop. The configuration is shown in Figure 3.16 and the results are analyzed in the next section. The data from this test will also help calibrate the machine, particularly in determining the required force values to achieve the corresponding stress values.

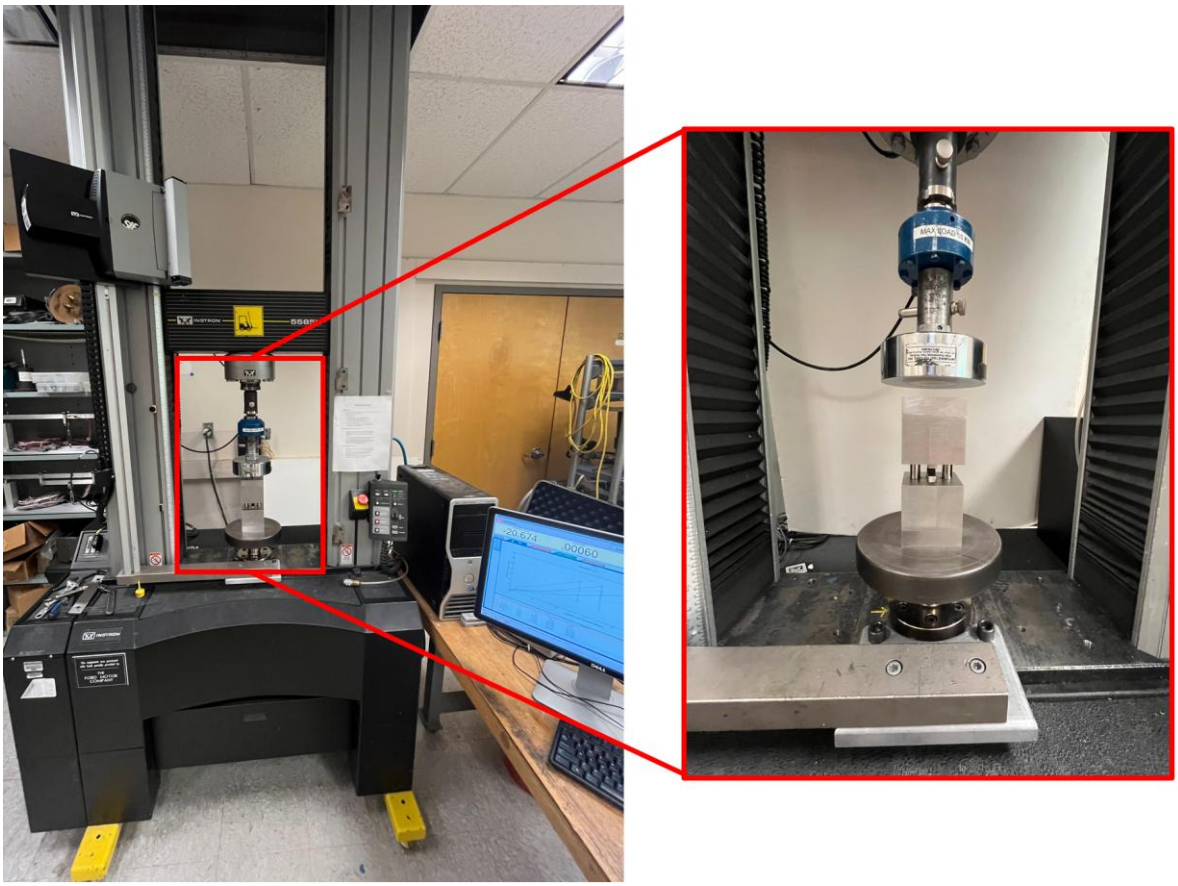

Figure 3.16. ASTM D6641 Setup

3.2.3 Validity of Fixture: Grounding

The grounding of the fixture was also a significant concern, as discussed in Section 2.3.5. In the initial stages of the procedure, the sample will be securely positioned within the fixture, establishing a direct connection to the lip of the apparatus. The side of the specimen attached to the lip will undergo a coating process with silver ink, specifically designed to enhance the electrical connection and conductivity of the setup. This method was further supported by the existing grounding straps, which were firmly affixed on both sides of the front fixture, thereby facilitating

a connection to the grounding surface, particularly the central column of the building where this operation took place.

This grounding method has been executed as an initial grounding pass; however, there is another viable alternative: adhering the width of the specimen to a compliant foil, such as copper or aluminum. This foil would then be securely affixed to the lip of the fixture. This specific approach was employed in scenarios where samples are maintained in an assembly with friction and are not positioned on the lip itself. Depending on the assessed effectiveness of this grounding scheme, a well-informed decision will be made regarding whether to proceed with it or to adopt the alternative strategy that involves using a copper frame. It should be noted, however, that a significant drawback associated with this copper frame strategy is the need for extensive machining on the sample itself. This machining process would require drilling multiple holes and incorporating small nuts and bolts to adequately secure the sample in place, thereby introducing additional complications and potential challenges to the overall process.

3.2.4 Validity of System: Tests with Aluminum Plate

Initial tests using lightning shots will occur on an aluminum plate. Because aluminum is a metal, it effectively conducts electricity without experiencing significant damage. The primary objective of these tests is to define the relationship between voltage and current. Specifically, the system must be calibrated correctly to achieve the necessary voltage levels to generate the desired current values. This project aims to simulate a modified waveform A with reduced amplitude, ranging from 30 kA to 50 kA, and these tests will help determine this relation.

3.2.5 Tests on CFRP Sample

In conclusion, after diligently completing all necessary safety checks, thoroughly approving the required Standard Operating Procedures (SOPs), and meticulously calibrating the system, it will be time to conduct a comprehensive test on the CFRP sample. There are numerous variables to consider during this process; however, to start, we will keep our approach straightforward. The primary objective will be to analyze and compare the damage sustained by an unloaded sample against that of a loaded one of a standard CFRP specimen with no change in configuration.

To further our analysis, the samples will subsequently undergo rigorous inspections utilizing advanced optical techniques, such as ultrasound imaging. This detailed evaluation will then be followed by a thorough residual strength test designed to assess and determine the structural integrity of the specimen after exposure to a lightning strike, thereby providing profound insights into its performance under extreme conditions. The infographic below summarizes the testing plan.

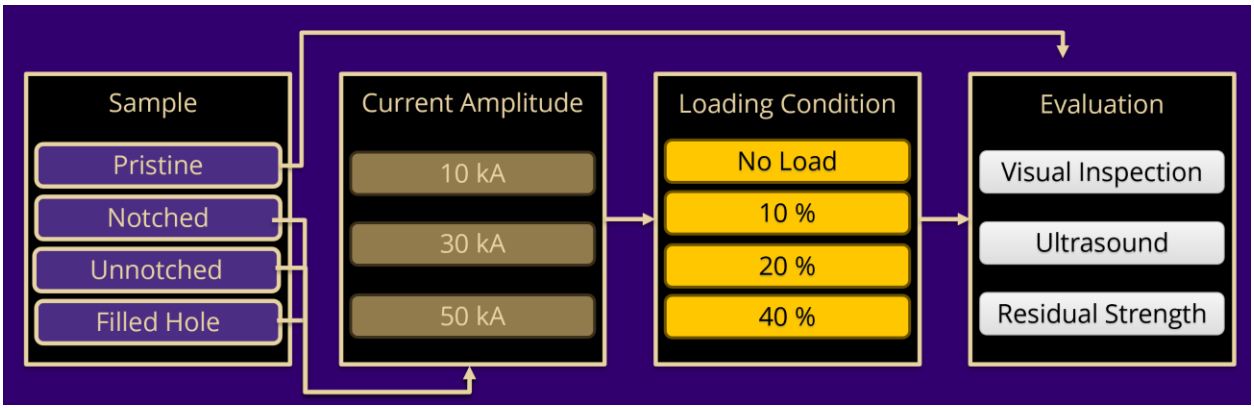

Figure 3.17. CFRP Sample Testing Infographic

3.3 Preliminary Tests Conclusions

3.3.1 Validity of Fixture: Dry Test

This section will provide a detailed report on the results of the Fixture Validation process. The strength of the specimen has been evaluated using the ASTM D6641 method. The specimens' post-test results are shown in Figure 3.18. The findings regarding the specimen's strength are summarized in Table 3-2 and plotted in Figure 3.19. The strength of the sample was recorded as 559.88 MPa for further analysis.

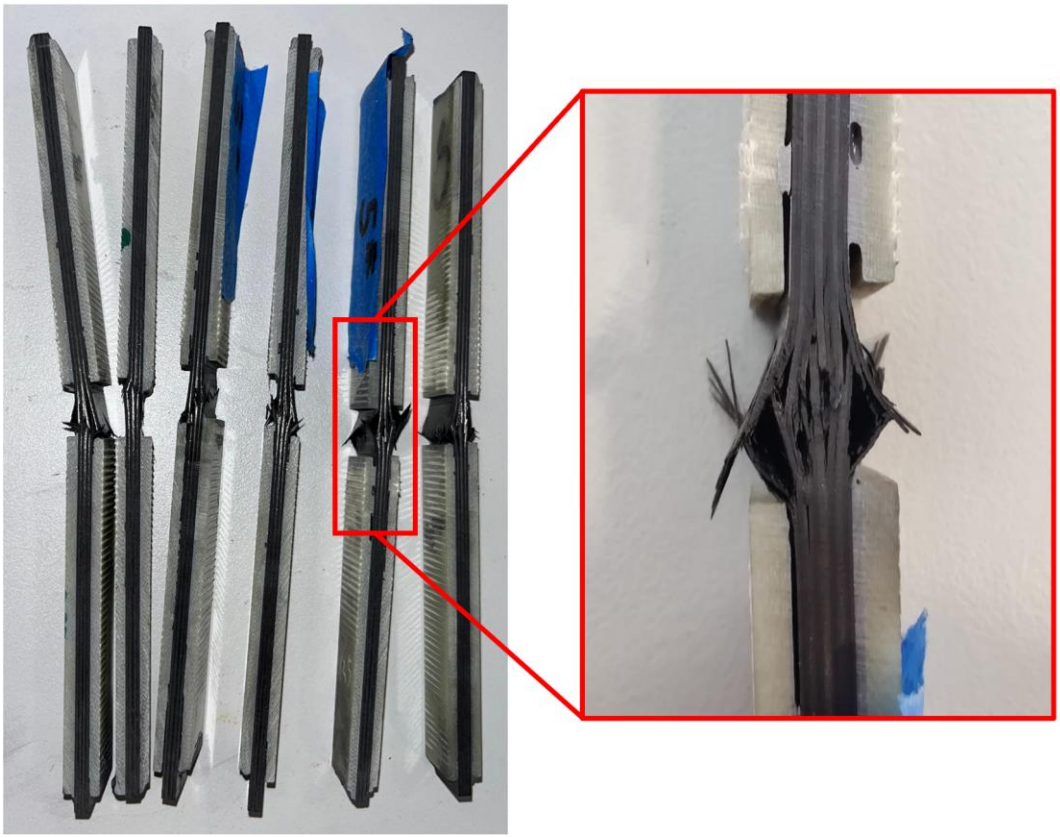

Figure 3.18. Specimens Post Test

Table 3-2: Compressive Strength

Sample Label	Compressive Strength at Maximum Load (MPa)
1	537.92
2	576.07
3	554.67
4	492.21
5	602.10
6	596.33

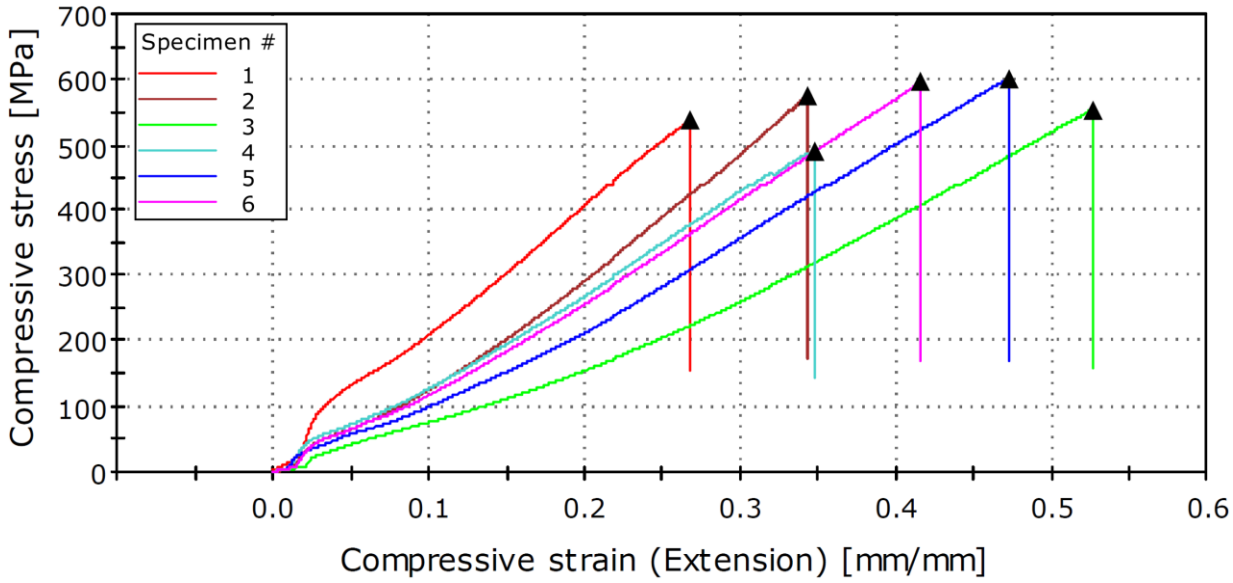

Figure 3.19. Stress–Strain Curve

Four specimens underwent dry testing using the fixture, with their damage primarily caused by local buckling, which further leads to delamination. The specimens and their damage characteristics are illustrated in the following images.

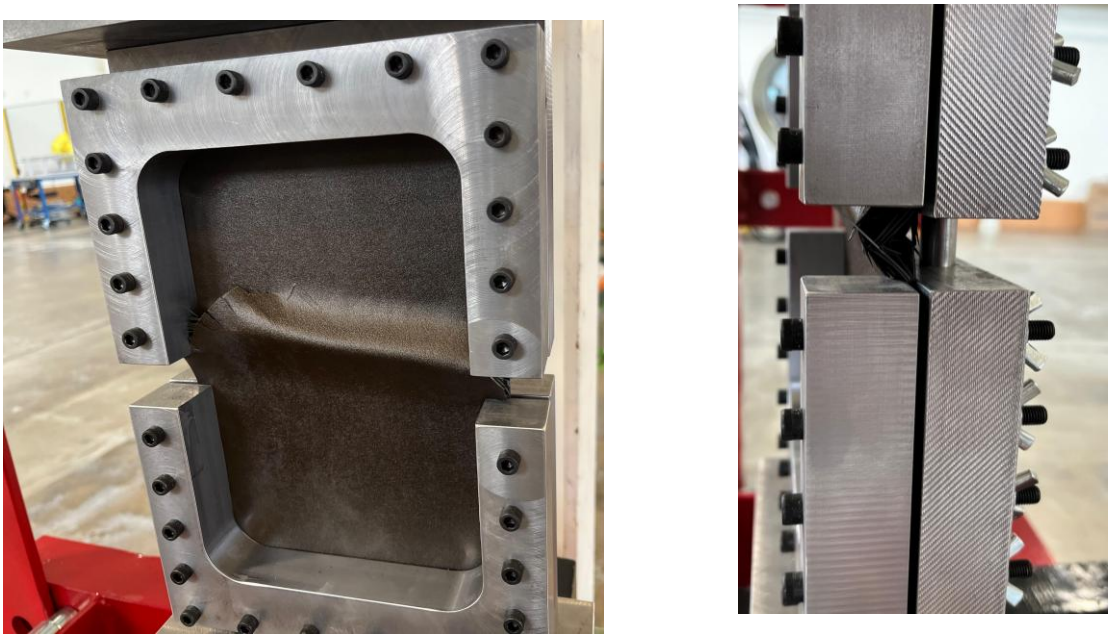

(a) Front View (b) Side View

Figure 3.20. Damage Characteristics of Sample 1

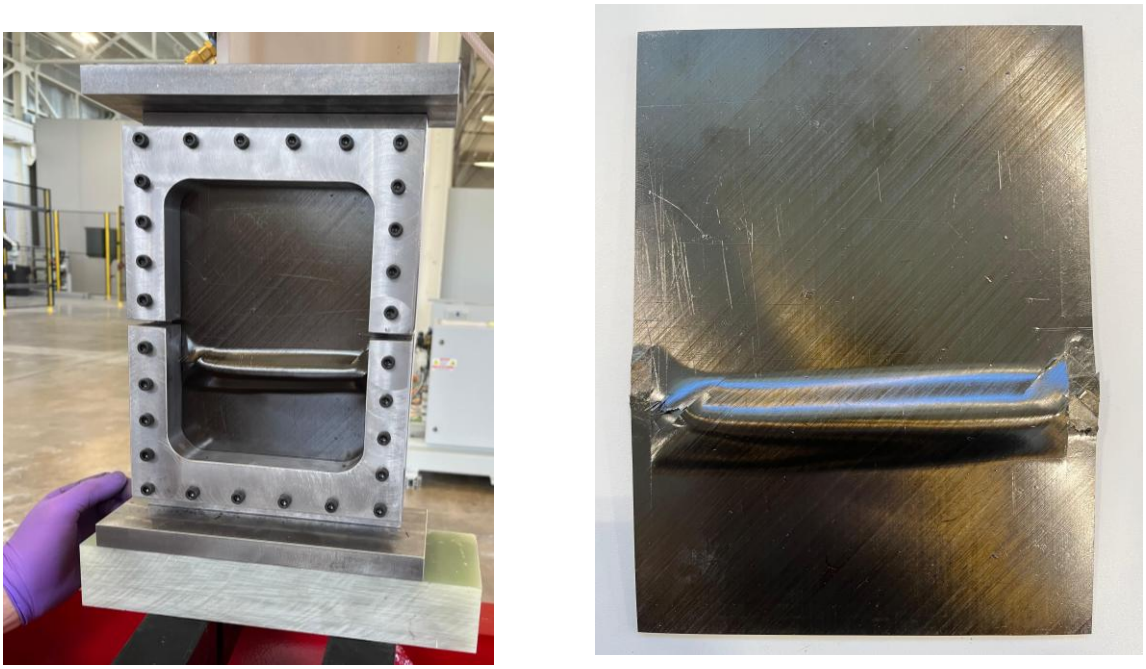

(a) Front View within the fixture (b) Removed from Fixture

Figure 3.21. Damage Characteristics of Sample 2

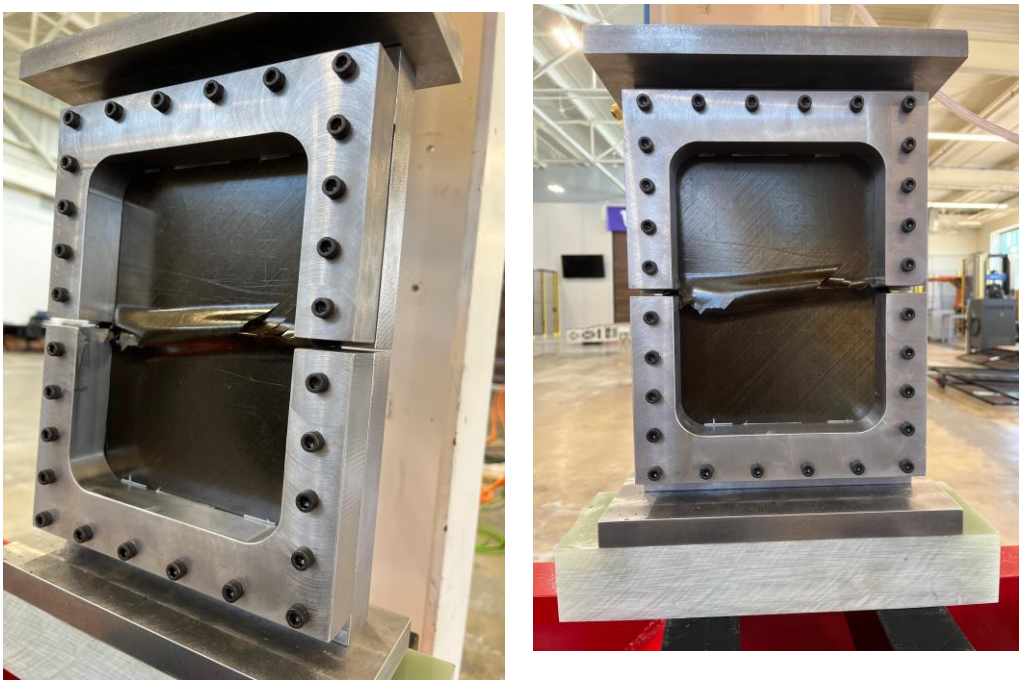

Figure 3.22. Damage Characteristics of Sample 3

Figure 3.23. Damage Characteristics of Sample 4

The dial gauge of the hydraulic press was monitored to determine the load at failure. The data was then processed to determine the stress experienced by the plate at failure. This data is summarized in Table 3-3.

Table 3-3: Stress at Failure

Sample Label	Failure Load (N)	Stress (MPa)	%age of Compressive Strength
1	110000	213.41	38.12 %
2	125000	280.17	50.04 %
3	120000	249.35	44.54 %
4	120000	262.09	46.81 %

Based on the various dry tests conducted, it can be stated that the current fixture design significantly surpasses the established design criteria. In fact, it achieves an impressive yield strength failure percentage that is nearly double that of the original design. This substantial improvement is not only noteworthy but will also play a critical role in guiding further testing and comprehensive analysis in the future. An important point to note is that the current tests are limited to the selected materials and lay-ups. Additional testing with different materials and lay-ups will be crucial for further characterizing the system's performance.

Chapter 4: Conclusion

4.1 Summary and Current Status

A one-of-a-kind lightning strike simulator has been developed to enable an in-depth examination of various specimens, with a particular focus on carbon fiber-reinforced polymers under compressive loads. An extensive analysis was performed to determine the most effective load application system, accurately size the specimen, and design an optimal fixture tailored to the study's specific requirements. As of this writing, the mechanical components of this system have been successfully constructed and rigorously tested at the Advanced Composites Center at the University of Washington in Seattle. Meanwhile, the electrical and electronic components are currently in the final stages of assembly and will soon be ready for a thorough safety inspection and preliminary testing scheduled for the upcoming weeks. Preliminary dry tests have shown that the fixture, in combination with the specimen, exceeds 20% of the yield strength, confirming that it meets the established design objectives.

This comprehensive and robust testing system is designed for easy access by Boeing at any time, providing crucial material performance data. This data is vital for enhancing safety guidelines, optimizing operational efficiency, and expanding applications within the aerospace industry. In addition to serving Boeing, the Strike Generator is also highly advantageous for small and medium-sized aerospace enterprises, extending its benefits to the entire Pacific Northwest supply chain. By optimizing LSP design, it effectively reduces the risk of severe damage from lightning strikes, ensuring greater safety for aircraft operations while reducing CO_2 emissions and improving fuel efficiency.

4.2 **Future Work**

This project will serve as the culmination of the development and validation cycle, particularly through the completion of preliminary mechanical tests. However, it is essential to recognize that this is merely the beginning of an extensive and detailed testing regimen ahead. Previous literature has indicated a variety of sample configurations that can undergo rigorous testing, including but not limited to notched and filled hole samples, specimens coated with dielectric materials, and specimens incorporating lightning strike protection systems. Conducting a comprehensive analysis of these diverse samples will significantly enhance our understanding of real-world aerospace applications and the potential threats posed by lightning strikes. Furthermore, the data collected throughout this project will be meticulously compiled and presented to Boeing, serving as a foundational starting point for optimizing and enhancing lightning strike protection system designs in the future.

4.2.1 Future Goals

1. Short Term
    - Completion of construction and assembly.
    - Conduct a thorough safety audit and develop and approve SOPs under technical supervision.
    - Perform preliminary tests to validate performance.
    - Create a detailed testing plan.
    - Prepare samples using various configurations.
    - Preliminary testing with CFRP Samples.

2. Medium Term
    - Safety Audit and approval by the Department of Environmental Health and Safety, University of Washington.
    - Conduct dry tests using specimens with different layups and materials.
    - Begin following the testing regimen as laid out, with proper documentation of damage characteristics with destructive and non-destructive testing using specimens of various materials characteristics and configurations.
    - Use of the fixture in a UTM for more accurate control of loading conditions.

3. Long Term
    - Preparation of a detailed report summarizing the results to aerospace organizations and regulatory authorities, recommending guidelines.
    - Introducing the ability to scale up and scale down the specimens being tested in terms of sample cross-sectional dimensions and thickness by introducing modifications to the fixture design.
    - Development of a Multiphysics electro-thermal-mechanical numerical model incorporating the effect of mechanical stress to optimize LSP design and safety. This can be done leveraging advanced composite models developed by the MAMS group, including continuum mesoscale and multiscale formulations ([139],[140],[141],[142]) and advanced discrete, mesoscale formulations ([143],[144],[145]).

BIBLIOGRAPHY

[1] D. K. Rajak, D. D. Pagar, R. Kumar, and C. I. Pruncu, "Recent progress of reinforcement materials: a comprehensive overview of composite materials," *Journal of Materials Research and Technology*, vol. 8, no. 6, pp. 6354–6374, Nov. 2019, doi: 10.1016/j.jmrt.2019.09.068.

[2] M. Maria, "Advanced composite materials of the future in aerospace industry," *INCAS BULLETIN*, vol. 5, no. 3, pp. 139–150, Sep. 2013, doi: 10.13111/2066-8201.2013.5.3.14.

[3] Fact.MR, "Aerospace Composites Market Report," 2025, 2023. [Online]. Available: https://www.factmr.com/report/aerospace-composites-market

[4] F. Khan *et al.*, "Advances of composite materials in automobile applications – A review," *Journal of Engineering Research*, p. S2307187724000440, Feb. 2024, doi: 10.1016/j.jer.2024.02.017.

[5] T. Edwards, "Composite Materials Revolutionize Aerospace Engineering," *Ingenia Magazine*, no. 36, Sep. 2008. [Online]. Available: https://www.ingenia.org.uk/articles/composite-materials-revolutionise-aerospace-engineering/

[6] B. Parveez, M. I. Kittur, I. A. Badruddin, S. Kamangar, M. Hussien, and M. A. Umarfarooq, "Scientific Advancements in Composite Materials for Aircraft Applications: A Review," *Polymers*, vol. 14, no. 22, p. 5007, Nov. 2022, doi: 10.3390/polym14225007.

[7] W. G. Roeseler, B. Sarh, and M. U. Kismarton, "COMPOSITE STRUCTURES: THE FIRST 100 YEARS," in *ICCM-16 Proceedings*, Kyoto, 2007.

[8] “Composites: Airbus continues to shape the future | Airbus.” [Online]. Available: https://www.airbus.com/en/newsroom/news/2017-08-composites-airbus-continues-to-shape-the-future

[9] A. Kausar, I. Rafique, and B. Muhammad, “Aerospace Application of Polymer Nanocomposite with Carbon Nanotube, Graphite, Graphene Oxide, and Nanoclay,” *Polymer-Plastics Technology and Engineering*, vol. 56, no. 13, pp. 1438–1456, Sep. 2017, doi: 10.1080/03602559.2016.1276594.

[10] “Boeing 787 Dreamliner Represents Composites Revolution.” [Online]. Available: https://www.designnews.com/assembly/boeing-787-dreamliner-represents-composites-revolution

[11] T. Boon and P. Pande, “The Story Of The Boeing 777X’s Wingtips,” Simple Flying. Accessed: Apr. 15, 2025. [Online]. Available: https://simpleflying.com/boeing-777x-wingtips/

[12] “New Russian jet heralds carbon manufacturing shake-up | Reuters.” Accessed: Apr. 15, 2025. [Online]. Available: https://www.reuters.com/article/us-aerospace-composites-analysis/new-russian-jet-heralds-carbon-manufacturing-shake-up-idUSKBN18P1X0/

[13] B. Alemour, O. Badran, and M. R. Hassan, “A Review of Using Conductive Composite Materials in Solving Lightening Strike and Ice Accumulation Problems in Aviation,” *J.Aerosp. Technol. Manag.*, 2019, doi: 10.5028/jatm.v11.1022.

[14] P. Singh *et al.*, “Composite material: A review over current development and automotive application,” *Materials Today: Proceedings*, p. S2214785323050812, Nov. 2023, doi: 10.1016/j.matpr.2023.11.012.

[15] S. K. Sardiwal, A. Sami, B. V. S. Anoop, G. Susmita, and L. Vooturi, “Advanced Composite Materials in Typical Aerospace Applications,” 2014.

[16] M. R. M. Asyraf *et al.*, “Advanced Composite in Aerospace Applications: Opportunities, Challenges, and Future Perspective,” in *Advanced Composites in Aerospace Engineering Applications*, N. Mazlan, S. M. Sapuan, and R. A. Ilyas, Eds., Cham: Springer International Publishing, 2022, pp. 471–498. doi: 10.1007/978-3-030-88192-4_24.

[17] M. A. Uman and V. A. Rakov, “The interaction of lightning with airborne vehicles,” *Progress in Aerospace Sciences*, vol. 39, no. 1, pp. 61–81, Jan. 2003, doi: 10.1016/S0376-0421(02)00051-9.

[18] “CERTIFICATION OF TRANSPORT AIRPLANE STRUCTURE,” U.S. Department of Transportation; Federal Aviation Administration, Advisory Circular AC 25-21, Sep. 1999.

[19] “Aircraft and lightning strikes: here is what the statistics say,” mainblades.com. [Online]. Available: https://www.mainblades.com/blog-posts/aircraft-and-lightning-strikes-here-is-what-the-statistics-say

[20] H. Ranter, “Accident Lockheed L-188A Electra OB-R-941, Friday 24 December 1971.” Accessed: Apr. 17, 2025. [Online]. Available: https://asn.flightsafety.org/wikibase/330639

[21] “Accident Details Flight 508.” Accessed: Apr. 17, 2025. [Online]. Available: https://web.archive.org/web/20181117142800/http://www.planecrashinfo.com/1971/1971-69.htm

[22] H. Ranter, “Accident Lockheed L-1649A Starliner N7313C, Friday 26 June 1959.” Accessed: Apr. 18, 2025. [Online]. Available: https://asn.flightsafety.org/asndb/333982

[23] A. News, “Next Month is 65 Years Since TWA Flight 891 Crashed,” AviationSource News. Accessed: Apr. 18, 2025. [Online]. Available: https://aviationsourcenews.com/next-month-is-65-years-since-twa-flight-891-crashed/

[24] “Boeing 707-121 | Federal Aviation Administration.” Accessed: Apr. 18, 2025. [Online]. Available: https://www.faa.gov/lessons_learned/transport_airplane/accidents/N709PA

[25] “08.12.1963: Pan Am Flight 214.” Accessed: Apr. 18, 2025. [Online]. Available: https://timenote.info/en/events/Pan-Am-Flight-214

[26] D. M. S. from the C. Whig, “50 years later, witnesses, families recall Flight 214 crash,” Newark Post. Accessed: Apr. 27, 2025. [Online]. Available: https://www.newarkpostonline.com/regional/50-years-later-witnesses-families-recall-flight-214-crash/article_c539e445-0cd1-5368-af70-f2bff93a1d93.html

[27] H. Kawakami, *Lightning strike induced damage mechanisms of carbon fiber composites*. University of Washington, 2011.

[28] G. Sweers, B. Birch, and J. Gokcen, “Lightning Strikes: Protection, Inspection and Repair,” *Aero Magazine*, no. 12, pp. 19–28, 2012.

[29] NASA Earth Observatory, “Where Lightning Strikes.” Accessed: Apr. 18, 2025. [Online]. Available: https://earthobservatory.nasa.gov/images/2002/where-lightning-strikes

[30] C. Parten, “NIAR KART R51135 Direct Effects Project,” no. 18.

[31] W. Golding, “Lightning Strikes on Commercial Aircraft: How the Airlines Are Coping,” *JAAER*, 2005, doi: 10.15394/jaaer.2005.1511.

[32] J. A. Plumer, N. O. Rasch, and M. S. Glynn, “Recent data from the airlines lightning strike reporting project,” *Journal of Aircraft*, vol. 22, no. 5, pp. 429–433, May 1985, doi: 10.2514/3.45142.

[33] F. A. Fisher and J. A. Plumer, “Lightning Protection of Aircraft Handbook”.

[34] J. O’Loughlin and S. R. Skinner, “General Aviation Lightning Strike Report and Protection Level Study,” National Institute for Aviation Research Wichita State University, Wichita, KS, DOT/FAA/AR-04/13, Aug. 2004.

[35] A. Larsson, A. Delannoy, and P. Lalande, “Voltage drop along a lightning channel during strikes to aircraft,” *Atmospheric Research*, vol. 76, no. 1–4, pp. 377–385, Jul. 2005, doi: 10.1016/j.atmosres.2004.11.033.

[36] P. Laroche, P. Blanchet, A. Delannoy, and F. Issac, “Experimental Studies of Lightning Strikes to Aircraft,” *AerospaceLab*, 2012.

[37] P. Lalande, A. Bondiou-Clergerie, and P. Laroche, “Analysis of Available In-Flight Measurements of Lightning Strikes to Aircraft,” presented at the International Conference on Lightning and Static Electricity, Jun. 1999, pp. 1999-01–2397. doi: 10.4271/1999-01-2397.

[38] J. Heeter, “A Comparison of the Pulse and Swept-Frequency Transfer Function Lightning Test Responses on an Airplane with Composite Structure,” presented at the International Conference on Lightning and Static Electricity, Sep. 2001, pp. 2001-01–2928. doi: 10.4271/2001-01-2928.

[39] F. A. Fisher and J. A. Plumer, “Lightning Protection of Aircraft,” National Aeronautics and Space Administration ; Scientific and Technical Information Office, General Electric Company, Pittsfield, Massachusetts, NASA Reference Publication Prepared for Aerospace Safety Research and Data Institute NASA Lewis Research Center 1008, 1977.

[40] “ARP5414B: Aircraft Lightning Zoning - SAE International.” Accessed: Apr. 23, 2025. [Online]. Available: https://www.sae.org/standards/content/arp5414b/

[41] R. Prabhakaran, “Lightning Strikes on Metal and Composite Aircraft And Their Mitigation,” *joast*, pp. 208–222, Aug. 2023, doi: 10.61653/joast.v63i3.2011.545.

[42] L. Chemartin *et al.*, “Direct Effects of Lightning on Aircraft Structure: Analysis of the Thermal, Electrical and Mechanical Constraints,” no. 5, 2012.

[43] R. E. Baldwin, C. J. Hardwick, and G. W. Reid, “Lightning Hazard to Modern Aircraft Structures and Systems,” presented at the The Aerospace Technology Conference and Exhibition, Birmingham, Oct. 1987.

[44] C. C. Goodloe, “Lightning Protection Guidlines for Aerospace Vehicles,” National Aeronautics and Space Administration, Marshall Space Flight Center, Alabama, NASA/TM-19990209734.

[45] J. Phillpott, “Recommended Practice for Lightning Simulation and Testing Technique for Aircraft,” Culham Lab, United Kingdom Atomic Energy Authority, CLM-R163, May 1977.

[46] “ARP5416B: Aircraft Lightning Test Methods - SAE International.” Accessed: Apr. 27, 2025. [Online]. Available: https://www.sae.org/standards/content/arp5416b/

[47] P. T. Hacker, “Lightning Damage to a General Aviation Aircraft - Description and Analysis,” National Aeronautics and Space Administration, Lewis Research Centre, Cleveland, Ohio, Technical Note NASA TN-D 7775.

[48] J. D. Robb, E. L. Hill, M. M. Newman, and J. R. Stahmann, “Lightning Hazards to Aircraft Fuel Tanks,” NACA-TN-4326, Sep. 1958. Accessed: Apr. 29, 2025. [Online]. Available: https://ntrs.nasa.gov/citations/19930085198

[49] S. L. J. Millen and J. Lee, “Microscale modelling of lightning damage in fibre-reinforced composites,” *Journal of Composite Materials*, vol. 57, no. 10, pp. 1769–1789, May 2023, doi: 10.1177/00219983231163271.

[50] "AC 20-53C - Protection of Aircraft Fuel Systems Against Vapor Ignition Caused by Lightning." Accessed: Apr. 29, 2025. [Online]. Available: https://www.faa.gov/regulations_policies/advisory_circulars/index.cfm/go/document.information/documentid/1034432

[51] "AC 25.981-1C - Fuel Tank Ignition Source Prevention Guidelines (Cancelled)." Accessed: Apr. 29, 2025. [Online]. Available: https://www.faa.gov/regulations_policies/advisory_circulars/index.cfm/go/document.information/documentID/73716

[52] C. E. Rash, "When Lightning Strikes," *Flight Safety Foundation | Aerosafety World*, Jun. 2010.

[53] P. T. Hacker and J. A. Plumer, "Measurements and Analysis of Lightning-Induced Voltages in Aircraft Electrical Circuits," presented at the SAE/USAF Lightning and Static Electricity Conference, Feb. 1970, p. 700924. doi: 10.4271/700924.

[54] J.-P. Parmantier, F. Issac, and V. Gobin, "Indirect Effects of Lightning on Aircraft and Rotorcraft," *Aerospace Lab*, no. 5, Dec. 2012.

[55] "AC 20-136B - Aircraft Electrical and Electronic System Lightning Protection." Accessed: Apr. 29, 2025. [Online]. Available: https://www.faa.gov/regulations_policies/advisory_circulars/index.cfm/go/document.information/documentid/1019488

[56] "lightning-strikes," *Safety First: The Airbus safety Magazine*, Nov. 2023.

[57] Z. Zhao and S. Wang, "Lightning the Electromagnetic Pulse Coupling of Airborne Secondary Radar Electronic Equipment Using Intelligent Computing," *Mobile Information Systems*, vol. 2022, no. 1, p. 1810862, 2022, doi: 10.1155/2022/1810862.

[58] D. Morgan, C. J. Hardwick, S. J. Haigh, and A. J. Meakins, “The Interaction of Lightning with Aircraft and the Challenges of Lightning Testing”.

[59] L. H. Santos, W. P. T. Sousa, S. S. F. De dafé, and P. A. M. Junior, “Microstructural characterization and mechanical behavior analysis of 7075-T6 aluminum subjected to simulated lightning strikes,” *Chinese Journal of Aeronautics*, vol. 34, no. 12, pp. 39–50, Dec. 2021, doi: 10.1016/j.cja.2020.08.045.

[60] A. Soysal, I. Ozkol, and E. Uzal, “An Analytical-Based Lightning-Induced Damage Model for an Aircraft Wing Exposed to Pressure Loading of Lightning,” *Mathematical Problems in Engineering*, vol. 2024, no. 1, p. 8313135, 2024, doi: 10.1155/2024/8313135.

[61] V. Kumar *et al.*, “Enhanced through-thickness electrical conductivity and lightning strike damage response of interleaved vertically aligned short carbon fiber composites,” *Composites Part B: Engineering*, vol. 253, p. 110535, Mar. 2023, doi: 10.1016/j.compositesb.2023.110535.

[62] Y. Zhu *et al.*, “Finite Element Analysis of Lightning Damage Factors Based on Carbon Fiber Reinforced Polymer,” *Materials (Basel)*, vol. 14, no. 18, p. 5210, Sep. 2021, doi: 10.3390/ma14185210.

[63] S. Millen, V. Kumar, and A. Murphy, “The Influence of Carbon Fiber Composite Specimen Design Parameters on Artificial Lightning Strike Current Dissipation and Material Thermal Damage,” *SAE Int. J. Aerosp.*, vol. 16, no. 2, pp. 01-16-02–0017, Apr. 2023, doi: 10.4271/01-16-02-0017.

[64] B. Wang *et al.*, “Understanding lightning strike induced damage mechanism of carbon fiber reinforced polymer composites: An experimental study,” *Materials & Design*, vol. 192, p. 108724, Jul. 2020, doi: 10.1016/j.matdes.2020.108724.

[65] Y. Guo and Y. Jia, “THERMAL DAMAGE CHARACTERISTICS OF CFRP LAMINATES SUBJECTED TO LIGHTNING STRIKE,” 2017.

[66] Y. Zhu *et al.*, “Finite Element Analysis of Lightning Damage Factors Based on Carbon Fiber Reinforced Polymer,” *Materials (Basel)*, vol. 14, no. 18, p. 5210, Sep. 2021, doi: 10.3390/ma14185210.

[67] W. Lin, Y. Wang, K. Yousefpour, C. Park, and V. Kumar, “Evaluating the Lightning Strike Damage Tolerance for CFRP Composite Laminates Containing Conductive Nanofillers,” *Appl Compos Mater*, vol. 29, no. 4, pp. 1537–1554, Aug. 2022, doi: 10.1007/s10443-022-10028-1.

[68] J. Lee, T. E. Lacy, and C. U. Pittman, “Lightning mechanical damage prediction in carbon/epoxy laminates using equivalent air blast overpressure,” *Composites Part B: Engineering*, vol. 212, p. 108649, May 2021, doi: 10.1016/j.compositesb.2021.108649.

[69] P. Naghipour, E. J. Pineda, and S. M. Arnold, “Simulation of Lightning-Induced Delamination in Un-protected CFRP Laminates,” *Appl Compos Mater*, vol. 23, no. 4, pp. 523–535, Aug. 2016, doi: 10.1007/s10443-016-9472-9.

[70] V. Kumar *et al.*, “Factors affecting direct lightning strike damage to fiber reinforced composites: A review,” *Composites Part B: Engineering*, vol. 183, p. 107688, Feb. 2020, doi: 10.1016/j.compositesb.2019.107688.

[71] K. Fu, L. Ye, L. Chang, C. Yang, and Z. Zhang, “Modelling of lightning strike damage to CFRP composites with an advanced protection system. Part I: Thermal–electrical transition,” *Composite Structures*, vol. 165, pp. 83–90, Apr. 2017, doi: 10.1016/j.compstruct.2017.01.008.

[72] C. Karch, A. Arteiro, and P. P. Camanho, “Modelling mechanical lightning loads in carbon fibre-reinforced polymers,” *International Journal of Solids and Structures*, vol. 162, pp. 217–243, May 2019, doi: 10.1016/j.ijsolstr.2018.12.013.

[73] M. Gagné and D. Therriault, “Lightning strike protection of composites,” *Progress in Aerospace Sciences*, vol. 64, pp. 1–16, Jan. 2014, doi: 10.1016/j.paerosci.2013.07.002.

[74] C. Karch and C. Metzner, “Lightning protection of carbon fibre reinforced plastics — An overview,” in *2016 33rd International Conference on Lightning Protection (ICLP)*, Estoril: IEEE, Sep. 2016, pp. 1–8. doi: 10.1109/ICLP.2016.7791441.

[75] M. Ostermann, J. Schodl, P. A. Lieberzeit, P. Bilotto, and M. Valtiner, “Lightning Strike Protection: Current Challenges and Future Possibilities,” *Materials*, vol. 16, no. 4, p. 1743, Feb. 2023, doi: 10.3390/ma16041743.

[76] “ARP5412C: Aircraft Lightning Environment and Related Test Waveforms - SAE International.” Accessed: Apr. 27, 2025. [Online]. Available: https://www.sae.org/standards/content/arp5412c/

[77] “AIR5662: Method for Predicting Lateral Attenuation of Airplane Noise - SAE International.” Accessed: Apr. 27, 2025. [Online]. Available: https://www.sae.org/standards/content/air5662/

[78] “ARP5577: Aircraft Lightning Direct Effects Certification - SAE International.” Accessed: Apr. 27, 2025. [Online]. Available: https://www.sae.org/standards/content/arp5577/

[79] EUROCAE (European Organisation for Civil Aviation Equipment), “Environmental Conditions and Test Procedures for Airborne Equipment,” EUROCAE, ED-14G, Dec. 2011.

[80] EUROCAE (European Organisation for Civil Aviation Equipment), “Aircraft Lightning Environment and Related Test Waveforms,” EUROCAE, ED-84, May 1997.

[81] EUROCAE (European Organisation for Civil Aviation Equipment), “Aircraft Lightning Test Methods,” EUROCAE, ED-105, Nov. 2004.

[82] A. Larsson, “The interaction between a lightning flash and an aircraft in flight,” *Comptes Rendus. Physique*, vol. 3, no. 10, pp. 1423–1444, Oct. 2002, doi: 10.1016/S1631-0705(02)01410-X.

[83] S. Millen, A. Murphy, G. Abdelal, and G. Catalanotti, “Understanding the Impact of Standardized SAE Waveform Parameter Variation on Artificial Lightning Plasma, Specimen Loading, and Composite Material Damage,” *SAE International Journal of Aerospace*, vol. 13, no. 1, pp. 01-13-01–0002, Feb. 2020, doi: 10.4271/01-13-01-0002.

[84] R. Caldon, M. Haddad, and G. Mastrolembo, “Analysis of the control system of a high tension test laboratory on composite materials for aeronautic applications.”

[85] S. A. Baldacim, N. Cristofani, C. D. N. Santos, and J. R. Lautenschlager, “Study of Lightning Effects in Aircraft,” presented at the 2004 SAE Brasil Congress and Exhibit, Nov. 2004, pp. 2004-01–3236. doi: 10.4271/2004-01-3236.

[86] P. Feraboli and M. Miller, “Damage resistance and tolerance of carbon/epoxy composite coupons subjected to simulated lightning strike,” *Composites Part A: Applied Science and Manufacturing*, vol. 40, no. 6–7, pp. 954–967, Jul. 2009, doi: 10.1016/j.compositesa.2009.04.025.

[87] P. Feraboli and H. Kawakami, “Damage of Carbon/Epoxy Composite Plates Subjected to Mechanical Impact and Simulated Lightning,” *Journal of Aircraft*, vol. 47, no. 3, pp. 999–1012, May 2010, doi: 10.2514/1.46486.

[88] F. Soulas *et al.*, “A method to replace lightning strike tests by ball impacts in the design process of lightweight composite aircraft panels,” *International Journal of Impact Engineering*, vol. 111, pp. 165–176, Jan. 2018, doi: 10.1016/j.ijimpeng.2017.09.007.

[89] H. Kawakami and P. Feraboli, “Lightning strike damage resistance and tolerance of scarf-repaired mesh-protected carbon fiber composites,” *Composites Part A: Applied Science and Manufacturing*, vol. 42, no. 9, pp. 1247–1262, Sep. 2011, doi: 10.1016/j.compositesa.2011.05.007.

[90] “AC 43-214A - Repairs and Alterations to Composite and Bonded Aircraft Structure.” Accessed: Apr. 29, 2025. [Online]. Available: https://www.faa.gov/regulations_policies/advisory_circulars/index.cfm/go/document.information/documentid/1029806

[91] G. W. Reid, “INVESTIGATIONS INTO THE DAMAGE FOR VARIOUS TYPES OF UNPROTECTED CARBON FIBRE COMPOSITESWITH A VARIETY OF LIGHTNING ARC ATTACHMENTS,” in *International Aerospace and Ground Conference on Lightning and Static Electricity*, Kennedy Space Center, Florida: NASA, 1991.

[92] Y. Hirano, S. Katsumata, Y. Iwahori, and A. Todoroki, “Artificial lightning testing on graphite/epoxy composite laminate,” *Composites Part A: Applied Science and Manufacturing*, vol. 41, no. 10, pp. 1461–1470, Oct. 2010, doi: 10.1016/j.compositesa.2010.06.008.

[93] T. M. Harrell, O. T. Thomsen, J. M. Dulieu-Barton, and S. F. Madsen, “Damage in CFRP composites subjected to simulated lighting strikes - Assessment of thermal and mechanical responses,” *Composites Part B: Engineering*, vol. 176, p. 107298, Nov. 2019, doi: 10.1016/j.compositesb.2019.107298.

[94] Q. Dong *et al.*, “Damage analysis of carbon fiber composites exposed to combined lightning current components D and C,” *Composites Science and Technology*, vol. 179, pp. 1–9, Jul. 2019, doi: 10.1016/j.compscitech.2019.04.030.

[95] X. Tian *et al.*, “Damage mechanism analysis for carbon fiber reinforced polymer composites with a fastener under lightning strike,” *Composite Structures*, vol. 289, p. 115465, Jun. 2022, doi: 10.1016/j.compstruct.2022.115465.

[96] X. Tian, J. Sun, Y. Li, B. Wang, X. Yao, and J. Chen, “Study on the Factors Influencing the Damage Modes of Carbon Fiber-Reinforced Polymer Composites with a Fastener Under Lightning Strike Conditions,” *Appl Compos Mater*, vol. 29, no. 2, pp. 711–727, Apr. 2022, doi: 10.1007/s10443-021-09987-8.

[97] C. Kuang, Y. Zhou, H. Zhu, Q. Shi, K. Fu, and Y. Li, “Thermal and mechanical damage to carbon fibre reinforced composites with metallic fasteners under lightning strike,” *Thin-Walled Structures*, vol. 193, p. 111280, Dec. 2023, doi: 10.1016/j.tws.2023.111280.

[98] D. L. Heidlebaugh, W. B. Avery, and S. T. Uhrich, “Effect of Lightning Currents on Structural Performance of Composite Material,” presented at the International Conference on Lightning and Static Electricity, Sep. 2001, pp. 2001-01–2885. doi: 10.4271/2001-01-2885.

[99] G. Zhou, J. Golding, and W. Sun, “STUDY OF DAMAGE CHARACTERISTICS IN COMPOSITE STRUCTURES FROM SIMULATED LIGHTNING STRIKES”.

[100] F. S. Wang, Y. Y. Ji, X. S. Yu, H. Chen, and Z. F. Yue, “Ablation damage assessment of aircraft carbon fiber/epoxy composite and its protection structures suffered from lightning strike,” *Composite Structures*, vol. 145, pp. 226–241, Jun. 2016, doi: 10.1016/j.compstruct.2016.03.005.

[101] X. Zhang, J. Zhang, X. Cheng, and W. Huang, "Carbon nanotube protected composite laminate subjected to lightning strike: Interlaminar film distribution investigation," *Chinese Journal of Aeronautics*, vol. 34, no. 2, pp. 620–628, Feb. 2021, doi: 10.1016/j.cja.2020.04.033.

[102] Y. Hirano *et al.*, "Lightning damage suppression in a carbon fiber-reinforced polymer with a polyaniline-based conductive thermoset matrix," *Composites Science and Technology*, vol. 127, pp. 1–7, Apr. 2016, doi: 10.1016/j.compscitech.2016.02.022.

[103] Y. Guo, Y. Xu, Q. Wang, Q. Dong, X. Yi, and Y. Jia, "Enhanced lightning strike protection of carbon fiber composites using expanded foils with anisotropic electrical conductivity," *Composites Part A: Applied Science and Manufacturing*, vol. 117, pp. 211–218, Feb. 2019, doi: 10.1016/j.compositesa.2018.11.022.

[104] Y. Guo *et al.*, "Implementation of fiberglass in carbon fiber composites as an isolation layer that enhances lightning strike protection," *Composites Science and Technology*, vol. 174, pp. 117–124, Apr. 2019, doi: 10.1016/j.compscitech.2019.02.023.

[105] H. Zhu, K. Fu, B. Yang, and Y. Li, "Nickel-coated nylon sandwich film for combination of lightning strike protection and electromagnetic interference shielding of CFRP composite," *Composites Science and Technology*, vol. 207, p. 108675, May 2021, doi: 10.1016/j.compscitech.2021.108675.

[106] S. S. A. Kumar, Md. N. Uddin, M. M. Rahman, and R. Asmatulu, "Introducing graphene thin films into carbon fiber composite structures for lightning strike protection," *Polymer Composites*, vol. 40, no. S1, Jan. 2019, doi: 10.1002/pc.24850.

[107] P. S. M. Rajesh, F. Sirois, and D. Therriault, “Damage response of composites coated with conducting materials subjected to emulated lightning strikes,” *Materials & Design*, vol. 139, pp. 45–55, Feb. 2018, doi: 10.1016/j.matdes.2017.10.017.

[108] S. L. J. Millen and A. Murphy, “Modelling and analysis of simulated lightning strike tests: A review,” *Composite Structures*, vol. 274, p. 114347, Oct. 2021, doi: 10.1016/j.compstruct.2021.114347.

[109] T. Ogasawara, Y. Hirano, and A. Yoshimura, “Coupled thermal–electrical analysis for carbon fiber/epoxy composites exposed to simulated lightning current,” *Composites Part A: Applied Science and Manufacturing*, vol. 41, no. 8, pp. 973–981, Aug. 2010, doi: 10.1016/j.compositesa.2010.04.001.

[110] A. Duongthipthewa, Y. Tian, O. Duongthipthewa, Z. Su, and L. Zhou, “A comprehensive analysis of electric, thermal, and structural effects of lightning strikes on CFRP composites and protective strategies,” *Composites Communications*, vol. 44, p. 101739, Dec. 2023, doi: 10.1016/j.coco.2023.101739.

[111] Q. Dong, G. Wan, L. Ping, Y. Guo, X. Yi, and Y. Jia, “Coupled thermal-mechanical damage model of laminated carbon fiber/resin composite subjected to lightning strike,” *Composite Structures*, vol. 206, pp. 185–193, Dec. 2018, doi: 10.1016/j.compstruct.2018.08.043.

[112] Y. Xiao, J. Yin, S. Li, X. Yao, and F. Chang, “Characterization of Composite Laminate Lightning Strike Thermal-Mechanical Coupling Damage Based on Progressive Damage Model,” in *Proceedings of the 2018 7th International Conference on Energy, Environment and Sustainable Development (ICEESD 2018)*, Hangzhou, China: Atlantis Press, 2018. doi: 10.2991/iceesd-18.2018.333.

[113] B. Yang *et al.*, "Coupled thermal-electrical–mechanical characteristics of lightning damage in woven composite honeycomb sandwich structures," *International Journal of Solids and Structures*, vol. 305, p. 113090, Dec. 2024, doi: 10.1016/j.ijsolstr.2024.113090.

[114] S. L. J. Millen, A. Murphy, G. Catalanotti, and G. Abdelal, "Coupled Thermal-Mechanical Progressive Damage Model with Strain and Heating Rate Effects for Lightning Strike Damage Assessment," *Appl Compos Mater*, vol. 26, no. 5–6, pp. 1437–1459, Dec. 2019, doi: 10.1007/s10443-019-09789-z.

[115] J. Lee, S. L. J. Millen, and X. Xu, "Critical comparison of potential machine learning methods for lightning thermal damage assessment of composite laminates," *Advanced Composite Materials*, pp. 1–21, Oct. 2024, doi: 10.1080/09243046.2024.2416169.

[116] Y. Wang, Y. Fan, and O. I. Zhupanska, "Challenges and Future Recommendations for Lightning Strike Damage Assessments of Composites: Laboratory Testing and Predictive Modeling," *Materials*, vol. 17, no. 3, p. 744, Feb. 2024, doi: 10.3390/ma17030744.

[117] P. Leichauer, "Design and Development of Lightning Waveform Generators".

[118] W. E. Howell, "Effects of Simulated Lightning Currents on the Tensile Strength of Graphite/Epoxy," in *International Aerospace and Ground Conference on Lightning and Static Electricity (8th), Lightning Technology Roundup*, Fort Worth, Texas: NASA, Jun. 1983.

[119] G. W. Reid, "Strength Degradation of C.F.C Due to Conduction of Simulated Lightning Currents with Varying Moisture and Mechanical Loading," in *Proceedings of the 1989 International Conference on Lightning and Static Electricity*, University of Bath, UK: Controller HMSO London, Sep. 1989.

[120] G. W. Reid, “Mechanical Damage to Aircraft Structures from Lightning Strikes,” *Proceedings of the Institution of Mechanical Engineers, Part G: Journal of Aerospace Engineering*, vol. 207, pp. 1–14, 1993.

[121] CNC Kitchen, *Fully OPEN SOURCE Universal Test Machine!*, (Feb. 16, 2019). Accessed: Aug. 12, 2024. [Online Video]. Available: https://www.youtube.com/watch?v=uvn-J8CbtzM

[122] “50 Ton Hydraulic Shop Press.” Accessed: May 30, 2025. [Online]. Available: https://www.harborfreight.com/automotive/auto-body-trim/metalwork-tools/shop-presses/50-ton-hydraulic-shop-press-96188.html

[123] E. R. Johnson, *Aerospace Structures*. Kevin T. Crofton Department of Aerospace and Ocean Engineering in association with Virginia Tech Publishing, 2021. doi: 10.21061/AerospaceStructures.

[124] D30 Committee, *Test Method for Compressive Residual Strength Properties of Damaged Polymer Matrix Composite Plates*. doi: 10.1520/D7137_D7137M-23.

[125] D30 Committee, *Test Method for Compressive Properties of Polymer Matrix Composite Materials Using a Combined Loading Compression (CLC) Test Fixture*. doi: 10.1520/D6641_D6641M-23.

[126] X. Xu *et al.*, “Developing Test Methods for Compression after Lightning Strikes,” *Appl Compos Mater*, vol. 30, no. 2, pp. 539–556, Apr. 2023, doi: 10.1007/s10443-022-10100-w.

[127] S. Sanchez-Saez, E. Barbero, R. Zaera, and C. Navarro, “Compression after impact of thin composite laminates,” *Composites Science and Technology*, vol. 65, no. 13, pp. 1911–1919, Oct. 2005, doi: 10.1016/j.compscitech.2005.04.009.

[128] S. Guo, X. Li, T. Liu, G. Bu, and J. Bai, "Parametric Study on Low-Velocity Impact (LVI) Damage and Compression after Impact (CAI) Strength of Composite Laminates," *Polymers*, vol. 14, no. 23, p. 5200, Nov. 2022, doi: 10.3390/polym14235200.

[129] Q. J. Yang, "Simplified Approaches to Buckling of Composite Plates," University of Oslo.

[130] Y. Zhu *et al.*, "Finite Element Analysis of Lightning Damage Factors Based on Carbon Fiber Reinforced Polymer," *Materials*, vol. 14, no. 18, p. 5210, Sep. 2021, doi: 10.3390/ma14185210.

[131] "ASTM D7137 Test Fixture | GD7137-818 - TestResources." Accessed: May 16, 2025. [Online]. Available: https://www.testresources.net/accessories/fixtures-by-standards/astm-fixtures/gd7137-818

[132] L. Francesconi, G. Loi, and F. Aymerich, "Impact and Compression-After-Impact Performance of a Thin Z-Pinned Composite Laminate," *J. of Materi Eng and Perform*, vol. 32, no. 9, pp. 3923–3937, May 2023, doi: 10.1007/s11665-023-07855-z.

[133] X. Xu, A. Paul, X. Sun, and M. R. Wisnom, "An experimental study of scaling effects in notched quasi-isotropic carbon/epoxy laminates under compressive loads," *Composites Part A: Applied Science and Manufacturing*, vol. 137, p. 106029, Oct. 2020, doi: 10.1016/j.compositesa.2020.106029.

[134] F. S. Wang, X. S. Yu, S. Q. Jia, and P. Li, "Experimental and numerical study on residual strength of aircraft carbon/epoxy composite after lightning strike," *Aerospace Science and Technology*, vol. 75, pp. 304–314, Apr. 2018, doi: 10.1016/j.ast.2018.01.029.

[135] K. Yousefpour, W. Lin, Y. Wang, and C. Park, "Discharge and ground electrode design considerations for the lightning strike damage tolerance assessment of CFRP matrix

composite laminates," *Composites Part B: Engineering*, vol. 198, p. 108226, Oct. 2020, doi: 10.1016/j.compositesb.2020.108226.

[136] D30 Committee, *Test Method for Compressive Properties of Polymer Matrix Composite Materials with Unsupported Gage Section by Shear Loading*. doi: 10.1520/D3410_D3410M-16E01.

[137] Z. S. AG, "G3 digital cutter | Flatbed CNC Cutter | Zünd," Zünd Systemtechnik AG. Accessed: Apr. 10, 2025. [Online]. Available: https://www.zund.com/en/cutting-systems/digital-cutting-systems/g3-cutter

[138] "Prepreg Data Sheet | Hexcel." Accessed: Apr. 10, 2025. [Online]. Available: https://www.hexcel.com/resources/datasheets/prepreg?lC=BMI

[139] K. Kirane, M. Salviato, and Z. P. Bažant, "Microplane triad model for simple and accurate prediction of orthotropic elastic constants of woven fabric composites," *Journal of Composite Materials*, vol. 50, no. 9, pp. 1247–1260, Apr. 2016, doi: 10.1177/0021998315590264.

[140] M. Salviato, S. E. Ashari, and G. Cusatis, "Spectral stiffness microplane model for damage and fracture of textile composites," *Composite Structures*, vol. 137, pp. 170–184, Mar. 2016, doi: 10.1016/j.compstruct.2015.10.033.

[141] K. Kirane, M. Salviato, and Z. P. Bažant, "Microplane-Triad Model for Elastic and Fracturing Behavior of Woven Composites," *Journal of Applied Mechanics*, vol. 83, no. 4, p. 041006, Apr. 2016, doi: 10.1115/1.4032275.

[142] Y. Kumagai, S. Onodera, M. Salviato, and T. Okabe, "Multiscale analysis and experimental validation of crack initiation in quasi-isotropic laminates," *International*

Journal of Solids and Structures, vol. 193–194, pp. 172–191, Jun. 2020, doi: 10.1016/j.ijsolstr.2020.02.010.

[143] M. Salviato, S. E. . Phenisee, A. A. Deleo, D. Pelessone, and M. Flores, "TO THE MESOSCALE AND BEYOND! CAPTURING COMPLEX DAMAGE MECHANISMS IN COMPOSITES VIA SIMPLE, PHYSICS-BASED, DISCRETE MATHEMATICAL MODELS OF FIBERS AND MATRIX," in *American Society for Composites 2023*, Destech Publications, Inc., Sep. 2023. doi: 10.12783/asc38/36705.

[144] M. Salviato, S. Phenisee, A. Deleo, D. Pelessone, and M. Flores, "A Novel Discrete, Mesoscale Modeling Framework for the Simulation of the Damaging and Fracturing Behavior of Composites," in *Volume 9: Mechanics of Solids, Structures, and Fluids; Micro- and Nano-Systems Engineering and Packaging; Safety Engineering, Risk, and Reliability Analysis; Research Posters*, Columbus, Ohio, USA: American Society of Mechanical Engineers, Oct. 2022, p. V009T12A015. doi: 10.1115/IMECE2022-95617.

[145] S. E. Phenisee, A. A. Deleo, D. Pelessone, M. Flores, and M. Salviato, "DISCRETE, MESO-SCALE MODELING OF FIBER- REINFORCED COMPOSITES (DM4C): APPLICATION TO ADDITIVE MANUFACTURING OF CONTINUOUS FIBER COMPOSITES," in *American Society for Composites 2022*, Destech Publications, Inc., Sep. 2022. doi: 10.12783/asc37/36474.